MIXED CLUSTERS FROM THE COEXPANSION OF C_2F_6 AND N_2 IN A PULSED, SUPERSONIC EXPANSION CLUSTER ION SOURCE AND BEAM DEFLECTION TIME-OF-FLIGHT MASS SPECTROMETER: A FIRST APPLICATION

By

STEVEN DANE THOMPSON

A DISSERTATION PRESENTED TO THE GRADUATE SCHOOL
OF THE UNIVERSITY OF FLORIDA IN PARTIAL FULFILLMENT
OF THE REQUIREMENTS FOR THE DEGREE OF
DOCTOR OF PHILOSOPHY

UNIVERSITY OF FLORIDA

1994

To Lee Ann, Justin, and Tara

Born in leaks, the original sin of vacuum technology, molecular beams are collimated wisps of molecules traversing the chambered void that is their theatre like companies of players framed by some proscenium arch. On stage for only milliseconds between their entrances and exits, they have captivated an ever-growing audience by the variety and range of their repertoire.

John B. Fenn

ACKNOWLEDGMENTS

The completion of this work would not have been possible if it were not for the help and support of many individuals; their assistance is therefore cheerfully acknowledged.

First, I would like to thank Dr. M. L. Muga for his invaluable help and guidance throughout the course of these investigations and subsequent preparation of this dissertation. I am grateful to Dr. F. E. Dunnam, Dr. R. J. Hanrahan, Dr. M. T. Vala and Dr. W. Weltner, Jr. for their constructive suggestions offered as members of the supervisory committee.

Additionally, I am indebted to David Burnsed for his tireless efforts in the development of the data acquisition code for the mass spectrometer, and for his assistance in troubleshooting, repairing, and in several instances completely redesigning faulty electronic circuits. For the myriad support he has provided to insure the success of this project, I am truly grateful.

I thank Chester Eastman, Vernon Cook and Dailey Burch for their skillful fabrication of countless components necessary for the construction of the experimental apparatus. I am also thankful for the assistance Shawn Hsu and Matthew Litman provided as participants of the Florida Foundation for Future Scientists Student Science Training Program. The efforts of Larissa Brown through the Summer Research Apprenticeship Program are appreciated as well. I am also grateful for the extensive literature searches conducted by Carol Drum.

I would especially like to thank the U. S. Air Force--specifically, Capt. Steven Payne of the Air Force Institute of Technology, and Drs. Stephen Rodgers and Patrick

Carrick of the Phillips Laboratory--for the cooperation and support I received during my assignment at the University of Florida. The equipment loan from the Philips Laboratory is also gratefully acknowledged.

For their considerable effort in the initial design and construction of the cluster ion source, I thank Dr. Young Bae of the Stanford Research Institute, and Joe Newnham and Bob Frazier of the Jet Propulsion Laboratory. I am also grateful to TOFTEC, Inc. for the loan of the time-of-flight mass spectrometer and associated hardware, without which this project simply could not have been completed.

I offer my heartfelt thanks to my friends in the Nuclear and Radiation Chemistry groups--Dr. Avi Gupta, Craig Hoag, David Miko, Harish Narain, and Ma'an Raja--who have been of great assistance on countless occasions during the course of this work. It has truly been a pleasure to work with each of them.

I thank my mother and father for their abiding confidence and reassurance .

Finally, I gladly acknowledge the support and encouragement of my wife and children; their fresh and dynamic approach to life has provided the inspiration and motivation needed to complete this challenging project.

PREFACE

In the spring of 1990, a new untested hydrogen cluster ion source constructed to support a rocket propulsion project whose funding had recently been canceled was delivered to the Phillips Laboratory. Just a few months earlier, three chemists at Brookhaven National Laboratory (BNL), Robert Beuhler, Gerhart Friedlander and Lewis Friedman had announced achievement of deuteron-deuteron (D-D) fusion by impacting 200 to 325 keV D_2O cluster ions on TiD targets.[1] This new "cluster-impact fusion" technique drew immediate attention. Unlike the cold fusion claims made earlier by Pons and Fleishmann,[2] the BNL results had come from a respected research group which was very familiar with nuclear chemistry techniques. Even though the possibility that light, high-velocity beam artifacts may have been responsible for the observed fusion events was pointed out almost from the start,[3] the BNL results certainly merited further investigation.

And so the stage was set. A cooperative effort between the Phillips Laboratory and the University of Florida was initiated with the goal of attempting to reproduce the BNL experiments. The cluster ion source was shipped to Gainesville in the fall of 1990, and the installation and equipment modifications were begun while anxiously watching the progress of cluster-impact fusion in the scientific literature.

While theorists offered explanations for the new fusion method,[4,5] Fallavier et al.[6] published the results of a failed attempt to reproduce the BNL results using pure deuterium clusters. They also suggested that beam contamination problems with the BNL experiment might be very serious.

In an honest attempt to answer their critics, the BNL group published more positive results with other deuterium-containing target materials along with the results of

extensive tests performed to exclude artifacts as the cause of the observed D-D fusions.[7] In July 1991 the BNL group published additional evidence from time-of-flight experiments which ruled out low molecular weight ions containing oxygen (i.e. D_2O^+, D_3O^+) as responsible for the observed fusion events.[8] Yet the possibility of stray deuterons as the possible cause persisted.

By this time we were having our own problems as it became increasingly obvious that the ion source we received was in need of major redesign and repair. During the conduct of any sizable undertaking, unanticipated problems and difficulties often arise--however, this research effort proved more than typical in this regard. Almost from the very start, ominous obstacles were encountered with the ion source design. Extensive modifications of the pulse valve, ion optics assembly and numerous other subsystems were required. Additionally, a completely new electron gun had to be designed and constructed. In short, the apparatus we received from the Phillips lab was far from being a "turn key" system.

In addition to the equipment problems with the ion source, the TOFTEC time-of-flight mass spectrometer we intended to use to characterize the ion source was aging and required a complete overhaul; this entailed the replacement of badly cracked microchannel plates along with substantial modification of the detector configuration to improve detection efficiency.

While our equipment modifications were being effected, the first independent experimental confirmation of cluster-impact fusion was reported by Young Bae et al. at SRI International.[9] However, the SRI experiment, just like the one at BNL, did not include post-acceleration beam analysis.

Young Bae joined the BNL research group which now began experiments in which the post-acceleration beam was analyzed by both magnetic and electrostatic deflection. Their initial findings, as published in an errata submitted to *Physical Review Letters*, were that artifacts were primarily responsible for events previously ascribed to cluster-impact

fusion.[10] Ironically, a comment based on the proton peak broadening reported in the original BNL paper appeared in the same issue of *Physical Review Letters* in which Lo, Petrasso and Wenzel strongly suggest light-ion beam contaminants were likely responsible for the observed fusion events.[11] The BNL announcement was followed by the publication of yet another failed attempt to find evidence of a collective enhancement of D-D fusion for carbon-cluster impact on CD_2 targets beyond that predicted by a knock-on model.[12] A complete, detailed report of the BNL post-acceleration experiments has just recently been published in which the D-D fusion rates with small $(D_2O)_nD^+$ and $(H_2O)_nH^+$ ions (for up to n = 10) were carefully studied.[13] They observed no enhancement for the fusion rates of the small D_2O clusters after oxygen knock-on corrections were made. However, the fusion yields for knock-on processes produced by $(H_2O)_nH^+$ clusters (n = 4 to n = 10) showed approximately a two-fold enhancement over the yields for H_3O^+ ions at the same velocity.

Thus, cluster-impact fusion may yet prove to be a genuine route to small enhancements in D-D fusion yields. Careful experiments with large clusters still remain to be investigated.

As it turned out, the overall source design of our equipment precluded the formation of large water clusters without major redesign; also we lacked an accelerator column to reach the required kinetic energies cited as necessary to achieve cluster-impact fusion. Thus we altered our goals in accordance with what was reasonably within reach, and remained flexible to pursue promising leads.

Because of time and financial restraints, the solutions presented throughout this dissertation to the myriad problems which arose are, in some cases, not optimal; however, in the context of the current goals and available resources, they represented viable alternatives which permitted the research to progress in a timely and economical manner. In other words, though much of our research was indeed conducted in a vacuum, our business decisions were not. Simple and ingenious solutions were relentlessly sought.

In the words of Dr. Muga, "A good scientist must know his equipment!" I feel I can truly say the process of identifying, isolating, and ultimately solving the countless equipment deficiencies encountered over the last three years has afforded me a broad and rich educational experience which simply could not have been acquired in any other way. Additionally, the imperative to remain flexible and pursue goals which are realistically within reach (regardless if they were the original goals or not) has served well to introduce me to this fascinating, yet ever changing realm of human endeavor we call scientific research.

Steven D. Thompson
Gainesville, Florida
April 1994

TABLE OF CONTENTS

Page

ACKNOWLEDGMENTS iv

PREFACE vi

ABSTRACT xii

CHAPTERS

1 INTRODUCTION 1

Background 1
Cluster Ion Genesis 2
Cluster Ion Detection 5

2 EXPERIMENTAL APPARATUS 8

Introduction 8
Ion Source 11
Pulse Valve 11
E-gun 14
Ion Optics 16
Mass Spectrometer 23
General Configuration 23
Detector 23

3 BEAM DEFLECTION TIME-OF-FLIGHT MASS SPECTROMETRY 29

Introduction 29
A First Order Model 29
A Modified Bakker's Model 32
Applications 33
Approach 34
Experiment 34
Theory 40
Experimental 44
Results and Discussion 47

4 SURVEY OF INITIAL CLUSTER ION RESULTS 57

Introduction 57
Experimental 58
Results and Discussion 59

5 MIXED CLUSTER IONS FROM C_2F_6/N_2 COEXPANSION 73

Introduction 73
Experimental 74
Results and Discussion 77

APPENDICES

A MATHEMATICAL DERIVATIONS 92

B TRAJION SOURCE CODE 109

C TRAJION OUTPUT DATA 120

REFERENCES 144

BIOGRAPHICAL SKETCH 149

Abstract of Dissertation Presented to the Graduate School
of the University of Florida in Partial Fulfillment of the
Requirements for the Degree of Doctor of Philosophy

MIXED CLUSTERS FROM THE COEXPANSION OF C_2F_6 AND N_2
IN A PULSED, SUPERSONIC EXPANSION CLUSTER ION SOURCE AND BEAM
DEFLECTION TIME-OF-FLIGHT MASS SPECTROMETER:
A FIRST APPLICATION

By

Steven Dane Thompson

April 1994

Chairman: M. Luis Muga
Major Department: Chemistry

The design and characterization of a pulsed, supersonic jet cluster ion source are detailed. A commercial solenoid valve modified to provide electrical isolation between the nozzle and solenoid mechanism provided the pulsed gas flow at a nominal duty cycle of 8 Hz, 200 μs under source stagnation pressures of 1 to 4 atmospheres. Cluster ion formation was effected through the generation of seed ions via electron impact ionization of the gas as it exits the nozzle. The cluster ions were accelerated in a weak electric field ($\sim$ 1 V/cm) towards a 2 mm i.d. conical skimmer; the extracted core of the expanding gas flow was then accelerated to 550 eV and focused coaxially through a pair of Einzel lenses.

Collinear modulation of the collimated beam pulse for time-of-flight mass analysis was accomplished by beam deflection across an interchangeable slit (0.5, 1, 2, or 3 mm wide) positioned near the entrance of the mass spectrometer. The beam was swept back and forth as it traversed a varying electric field perpendicular to the beam axis. The field was generated between two parallel plates, 2.54 cm apart, by applying a positive square-

wave potential to one plate while the other plate was held constant; the beam deflection rise-time (0 → +200 V) could be varied continuously between 30 and 2200 ns. A first order computational model was developed to predict the behavior of the chopped beam. Both flight times and peak shape information were calculated for a range of experimental conditions; theory and experiment are shown to be in substantial agreement.

Characterization of the ion source was accomplished by successfully creating positive cluster ions from He, N_2 and CO_2 expansions. The beam pulse composition for the CO_2 expansion was also examined by generating a temporal cross-sectional profile from mass spectra taken by sampling (chopping) different regions of the pulse.

Finally, the formation of mixed clusters from the coexpansion of Freon 116 (C_2F_6) and N_2 is reported. Peaks at 97 and 147 amu are identified as $CF_3N_2^+$ and $C_2F_5N_2^+$ respectively. Isotope shifts observed when substituting $^{15}N_2$ (99 atom %) for $^{14}N_2$ (natural abundance) confirm the peak assignments.

CHAPTER 1
INTRODUCTION

Background

Since the first published report of the formation of cluster beams by Becker, Bier and Henkes[14] nearly 40 years ago, cluster research has grown into a multidisciplinary field attracting attention from chemists, physicists and material scientists alike. Cluster beams, and molecular beams in general, are particularly appealing because they offer a method to study molecular systems in a collisionless environment which is free from matrix effects, they also provide a controlled way to introduce perturbations and observe their effects, and by extraction from the core of a supersonic expanding gas flow, very low temperature molecular populations concentrated in one, or only a few, internal states can be achieved. In fact, at present, clusters represent perhaps the only tractable bridge between isolated molecules and the condensed phase.

Today, research opportunities abound as attempts to further our understanding of amorphous solids, surface interactions, catalysis, liquid structure, solvation effects, and many other finite-system properties through the study of small, isolated cluster systems. A recent Department of Energy materials science panel report concluded that the range of basic scientific opportunities in understanding clusters and cluster-assembled materials is both broad and deep.[15] The new chemistry of reaction processes occurring during the collision between a cluster and a solid surface is a particularly new and exciting research area which has been variously described as "chemistry with a hammer" or even "chemistry with a jack-hammer." Both theoretical and experimental results indicate novel reactive

processes can occur as severe shock waves from the impulse delivered as a fast cluster impacts a solid surface create local pressures up to 100,000 atmospheres and temperatures as high as 4000 K.[16-19] The experimental and theoretical aspects of the application of relatively large ionized cluster beams in particle-driven inertial confinement fusion have also been discussed.[20] Recent attempts to effect cluster-impact fusion through collisions of large D_2O cluster ions on deuterated targets have received much attention and were briefly discussed in the Preface.[1,7-10,13]

However, even in light of these and other intense research efforts, characterization of specific clusters themselves in terms of structure, bonding, and reactive properties is still in the early stages; much more particle-specific information is needed. Charged clusters, or cluster ions, play a particularly important role in such studies because specific clusters can be selected through standard mass filtering techniques.

Cluster Ion Genesis

Many methods for producing beams of cluster ions (both subsonic and supersonic) have been developed and are described in an exhaustive review by Mark and Castleman.[21] Electrospray methods have been successfully applied to liquid samples to generate either positively or negatively charged particles composed of a monomer unit and attached solvent molecules.[22-24] Partial pyrolysis of a liquid sample before the expansion has also been demonstrated as a thermospray technique for creating cluster ion beams of involatile materials.[25] Corona discharge ionization of gas monomers within the stagnation chamber prior to expansion has been shown to result in beams with significant cluster ion content.[26] Beuhler and Friedman[27,28] employed a corona discharge to produce positively charged cluster species (A_n^+) with up to 10^3 monomer units in their studies on argon, nitrogen, and water. These represent just a few of the methods which have been successfully used to generate cluster ions.

Electron impact (EI) ionization of an expanding supersonic gas very near the nozzle exit has also been successfully utilized to generate both positive and negative cluster ions from various source gases,[29-31] and is the technique employed in the present research effort. Like the corona discharge technique, this method produces charged monomers, or seed ions, which behave as condensation nuclei during the expansion. Growth of the cluster ions is assumed to proceed by a series of three-body associative collisions of the type:

$$A^+ \cdot A_n + A + M \rightarrow A^+ \cdot A_{n+1} + M \qquad \text{where n = 1, 2, . . .} \qquad \text{(Eq. 1-1)}$$

in which the excess heat of reaction is carried away as translational or internal energy in the third body M; this is in marked contrast to the direct ionization of neutral clusters in which the excess heat typically results in extensive fragmentation in most cases. Because these association reactions are primarily driven by ion-molecule interactions, which are in general much stronger than the van der Waals interactions that control neutral cluster growth, expansion conditions can be chosen in which cluster ions can be grown with the near exclusion of neutral clusters. The final structure of small cluster cations has been predicted to be principally determined by competition between two strong interactions--hole delocalization and ion-neutral polarization.[32,33] Shell structures around dimer or trimer ion cores have been observed in the early growth stages of various non-metallic cluster ions.[34] The "magic numbers" often observed in cluster ion distributions reflect the stability of the ions, and a growing body of evidence suggests cluster ions may have structures quite different from their neutral analogs.[32,33,35-37]

In order to insure that sufficient gas densities in the jet remain for rapid three-body collisions, the seed ions must be generated very early in the expansion (or prior to the expansion as is done in the corona discharge method); supersonic expansions typically retain adequate densities over a free expansion distance of about 10 nozzle diameters.[31]

Precipitous changes in the local pressure, temperature and density, which can easily span several orders of magnitude during a supersonic expansion (cf. Figure 1-1), have made theoretical modeling of cluster nucleation a difficult task since most kinetic parameters are temperature dependent, and cluster densities are a highly non-linear function of the monomer density.[38] Predictions and limitations of classical nucleation theory for cluster beam sources have been discussed by Stein.[39] Molecular dynamics and Monte-Carlo simulation techniques provide two additional methods to model cluster nucleation and growth. Practical scaling laws to predict cluster growth under different experimental conditions have been derived, and are presented in two excellent reviews by Hagena.[40,41]

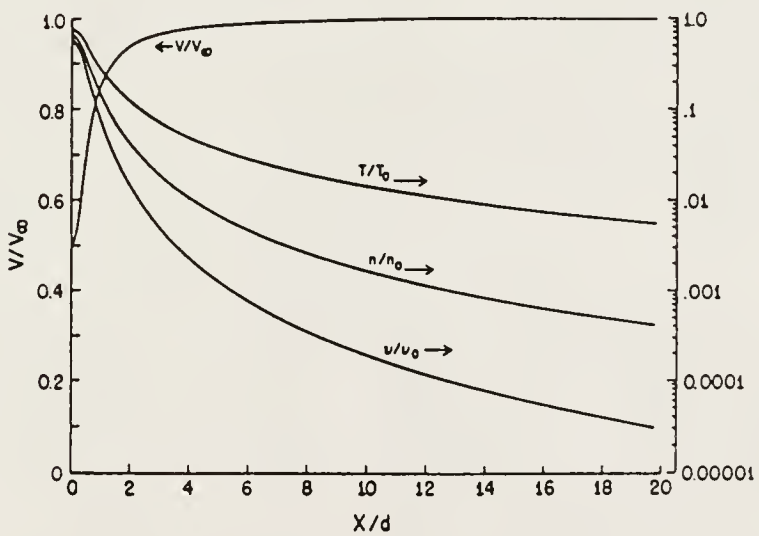

Figure 1-1 Free jet centerline properties versus distance (in nozzle diameters) from the source. A rapid and continuing decrease in temperature (T), density (n), and hard sphere collision frequency (ν) occurs with increasing distance from the source. T_0, n_0 and ν_0 are the source stagnation values. The mean velocity (V) rises quickly and asymptotically approaches the terminal velocity (V_∞). $C_p/C_v = 5/3$. (Taken from Miller.[42])

Many factors have been found to affect the degree of clustering which occurs during the adiabatic expansion of a gas in a supersonic jet, and are discussed by both Stein,[39] and Hagena,[40,41] as well as Ryali and Fenn.[43] Though the nozzle geometry has an important effect on the cluster beam intensity and average cluster size, the cluster composition in free jets is determined largely by the gas stagnation pressure, the gas stagnation temperature, and the nozzle diameter. In general, the cluster content and average cluster size increase with increased stagnation pressures and larger nozzle orifices, but decrease with higher reservoir temperatures.

Much higher source stagnation pressures can be reached without resorting to inordinately large vacuum systems by simply pulsing the beam. Pulsed beam intensities are orders of magnitude higher than continuous beam sources and have a much greater cluster content.[38] Since the first pulsed expansion work by Hagena,[44] pulsed nozzles have been popularized by Gentry and Giese,[45] as well as Liverman et al.[46] Pulsed beams, with all their obvious advantages for producing beams of clusters, do suffer from one minor problem--the beam velocity, temperature and cluster distribution are not uniform throughout the pulse. Saenger and Fenn[47,48] have provided theoretical estimates of the minimum time required for a fully open pulsed valve to generate a beam comparable to a continuous jet under the same source conditions.

Cluster Ion Detection

The method of choice for characterization of a pulsed cluster ion source is TOF mass spectrometry. It offers a simple, yet efficient means to measure ion mass with high throughput (and corresponding high sensitivity) and low noise over a large mass range. And because the pulsed valve imposes a relatively low duty cycle on the experiment, TOF methods are particularly well suited since they also require a low duty cycle in order to

permit the complete detection of a given ion bunch before a new ion bunch is injected into the mass spectrometer.

The principle of operation of TOF mass spectrometers is actually quite simple. A bunch of ions are accelerated in an electric field through a potential, V, and are then injected into a drift tube. After traversing the drift tube, the ions are detected with some type of fast electron multiplier device (i.e. microchannel plates). The kinetic energy of all of the ions, eV, is essentially the same and the velocity of each ion is inversely proportional to the square root of the mass. Thus, the light ions will arrive at the detector first while the heavier ions will arrive last. The detector response is recorded as a function of time and the mass for each resulting mass peak is assigned through the relationship:

$$m/e = \frac{2Vt^2}{L^2} \qquad \text{(Eq. 1-2)}$$

where L is the length of the drift tube and t is the flight time of a particular isomass ion packet.

The temporal pulse width of the ion bunch injected into the flight tube limits to a large degree the mass resolution obtainable. Typical pulse durations from pulsed valve sources range from ~ 50 μs to 1 ms and are quite long compared to typical ion transit times in a TOF mass spectrometer. Thus, for a continuously EI ionized pulsed cluster ion source, the beam must be modulated, or chopped, before it is introduced into the mass spectrometer. Beam deflection techniques offer an especially satisfying solution to this problem since they allow for a collinear experimental configuration and yet avoid, for instance, the many problems associated with operating a high speed rotating disk mechanical chopper in a high vacuum. Beam deflection TOF mass spectrometry is discussed at length in Chapter 3.

A superb review of TOF detection methods, cluster ion genesis and molecular beam methods in general, has recently been published.[49] This very well referenced monograph, edited by Giacinto Scoles, Davide Bassi, Udo Buck and Derek Laine, is written from an experimentalist's perspective and presents many options to the beam researcher who is setting out to design a new experiment. The essential principles and salient features of various techniques are presented in a simple and clear manner, and this compilation has been an invaluable guide in the conduct of this work.

CHAPTER 2
EXPERIMENTAL APPARATUS

Introduction

This chapter provides a general description of the equipment as currently configured. The cluster ion source (Figure 2-1) was originally designed and constructed by JPL and was on loan from the U. S. Air Force, while the TOF mass spectrometer (Figure 2-2) was supplied by TOFTEC, Inc. Since the cluster ion source underwent rather extensive redesign, and the TOF mass spectrometer was also significantly modified, no attempt has been made to indicate where modifications to their original designs were effected. Additionally, because every complex experimental apparatus is continually subject to modification and improvement to better meet the changing needs of the researcher, the design detail presented here reflects the latest experimental configuration only.

Careful attention was given throughout the redesign and modification of the apparatus to select materials which possessed characteristics best suited for their intended function within the vacuum system (i.e. low outgassing rate, high melting point, non-magnetic properties).[50,51] In addition, SIMION v4.02 was used extensively as a design tool to model potential energy surfaces and compute ion trajectories.[52] In general, SIMION predictions were found to be quite reliable and contributed greatly to the success of the final instrument design.

A detailed treatment of the beam deflection technique and associated hardware, as well as the data acquisition system is deferred to Chapter 3.

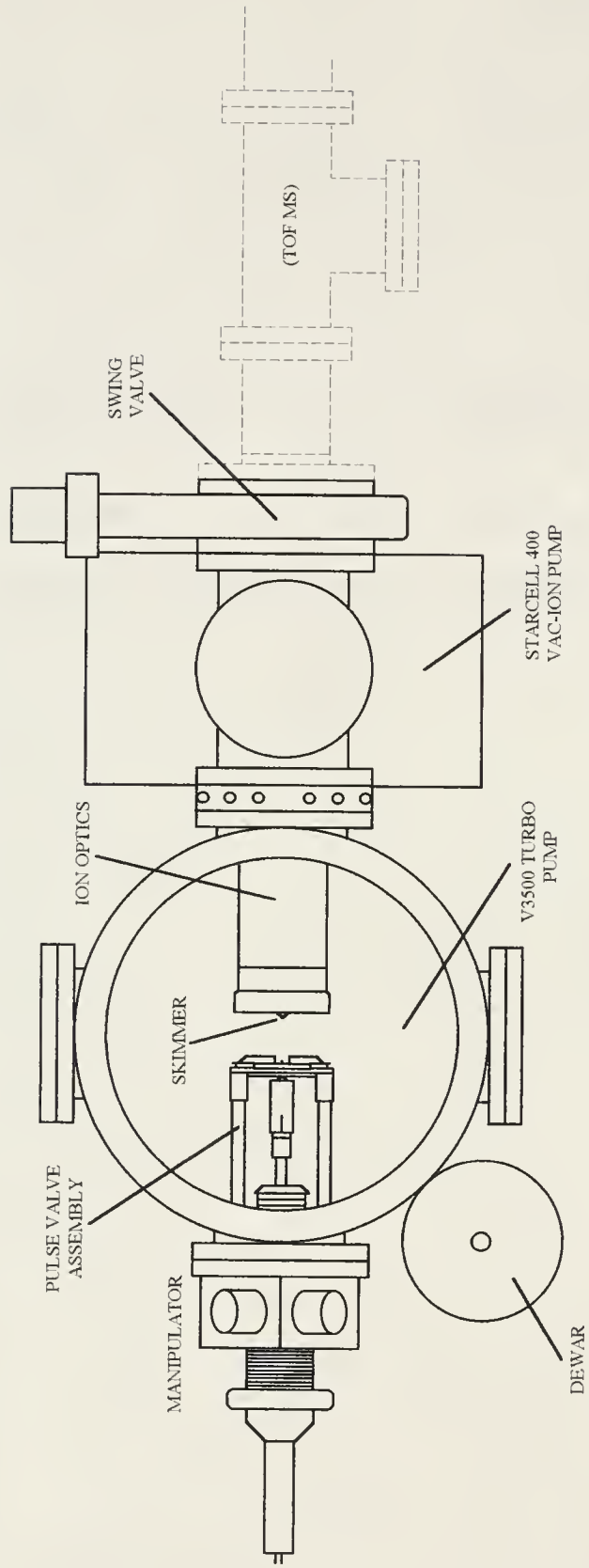

Figure 2-1 Top view of ion source. Shown with main chamber lid removed. Drawn to 1/8 scale.

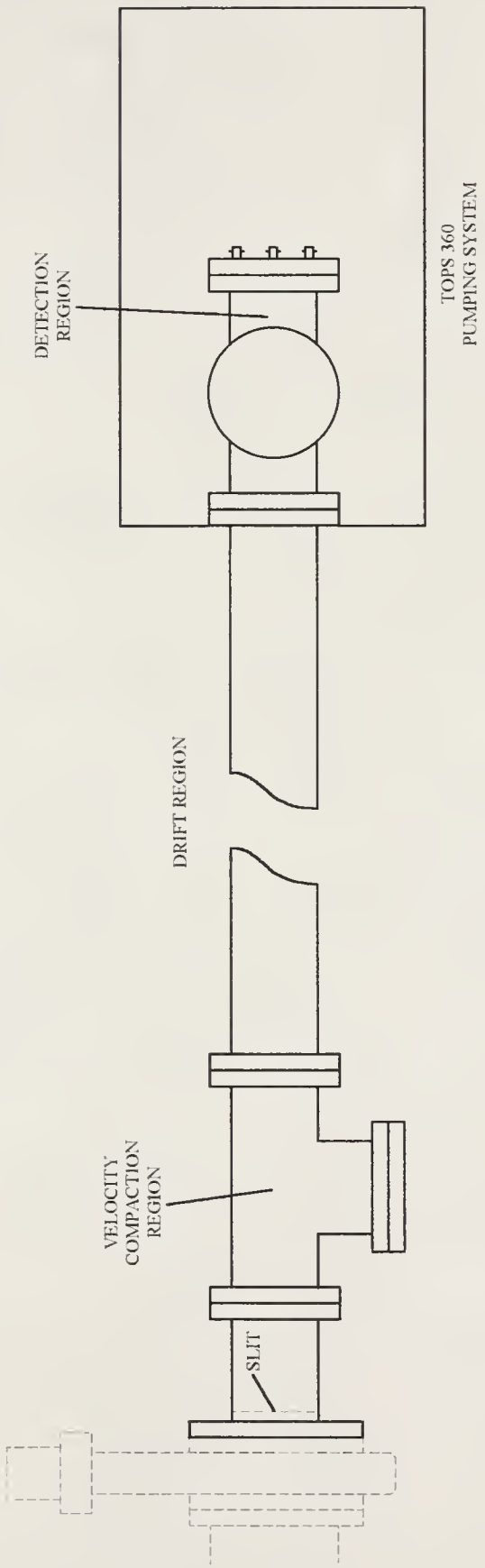

Figure 2-2 Top view of TOF mass spectrometer. Cutaway pipe section is 36 inches long from flange to flange. Drawn to 1/8 scale.

Ion Source

A top view of the ion source is shown in Figure 2-1. A 40 cm diameter chamber defines the vacuum envelope around the jet expansion region. A large Varian 3500 L/s turbomolecular pump, backed by a Varian 200 L/s turbo and a Varian 300 L/s mechanical pump, provides substantial pumping speed for the main vacuum chamber. The pressure is monitored from atmosphere down to operating pressures with a Granville-Phillips 307 gauge controller through the sequential use of a Convectron gauge and a nude ionization gauge mounted in the top of the chamber (not shown). The ion optics assembly is contained within a 6 inch diameter beam pipe; a Varian 400L/s StarCell VacIon pump provides additional pumping capacity in this region. Pressure measurements in the ion optics region are supplied by the ion pump controller. Two 6 inch pneumatic swing valves are positioned over the throat of the ion pump and at the distal end of the optics region near the start of the TOF mass spectrometer. To reduce the risk of equipment damage should high vacuum conditions be lost, the gauge and valve controllers are programmed to scram the system by automatically shutting down the e-gun and closing both swing valves if the pressure inside the vacuum chamber rises above an adjustable threshold--typically set at 5×10^{-5} torr.

Pulse Valve

A cross-sectional view of the pulse valve assembly is given in Figure 2-3. The assembly is mounted on a precision 3-way manipulator (cf. Figure 2-1). Adjustments orthogonal to the beam axis are made through micrometer drives and allow for setting the nozzle attitude. Though the nozzle is fixed with regard to movement along the beam axis, axial translation of the valve solenoid and attached valve rod can be accomplished by rotating a fine thread (24 tpi) screw; this capability is crucial for operating the pulse valve

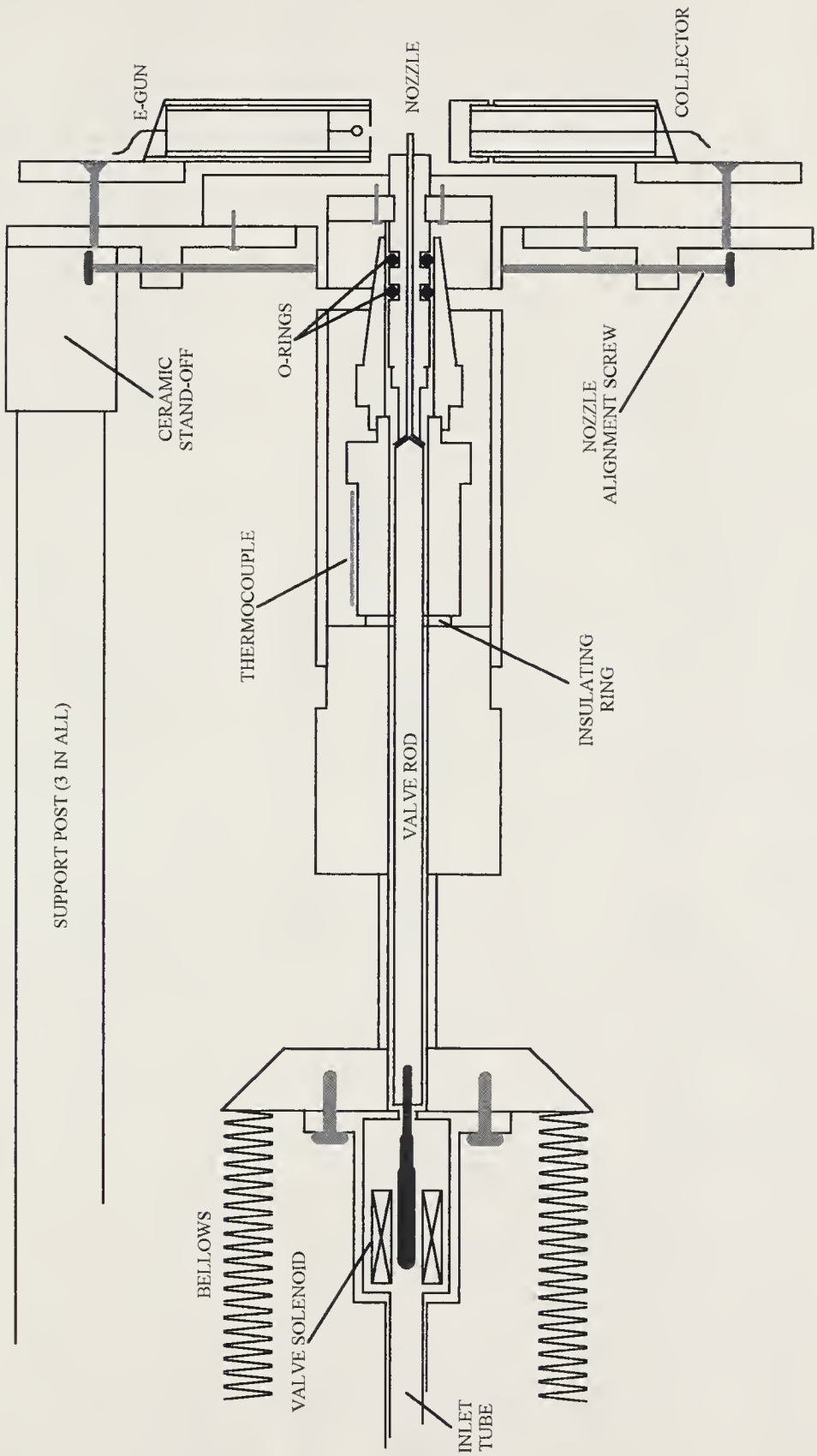

Figure 2-3 Cross-sectional view of nozzle assembly. Shown full scale.

since it permits optimization of the valve travel (nominally 0.008 - 0.020 inch) while the valve is in operation and the vacuum chamber is evacuated. This proved to be particularly important due to valve drift from thermal heating effects caused by the close proximity of the e-gun to the nozzle. Alignment of the jet nozzle with the skimmer and ion optics elements is effected through adjustment of the nozzle support plate.

The valve itself is constructed from a modified General Valve Series 9 pulse valve equipped with a lightweight (1.6 g) nylon valve rod which seats in a brass nozzle. An Iota One Pulse Driver controls the Series 9 solenoid and, for an unmodified valve, permits a nominal fast response (time to fully open) of 50 - 60 μs by overdriving the solenoid with an initial 300 V input for 165 μs; a holding voltage of about 20 V is then applied in accordance with the pulse duration selected on the Iota One Pulse Driver. Armature movement occurs only during the last 1/3 of the high voltage pulse. Thus there is about a 100 μs delay between the time when the voltage is first applied to the solenoid and when it actually begins to open. The relatively long time required to build and collapse the magnetic field within the solenoid also accounts for a minimum open time of 250 - 300 μs. A compression spring within the solenoid body restores the valve to the fully closed position in about 40 - 50 μs.[53] The valve was normally fired at a frequency of less than 10 Hz. The gas volume delivered per 200 μs pulse (measured for air at 1 atm. and 25°C) is approximately 5 μL.

The valve rod was fabricated from 5/32 inch diameter nylon stock and was tapered on one end to match the nozzle valve seat geometry; the valve and seat were lapped together prior to assembly to ensure a good seal. A groove 1/16 inch wide and 1/32 inch deep was cut down the entire length of the rod to permit unrestricted gas flow to the nozzle.

The nozzle body was constructed from brass, but contains a 4.65 cm long stainless steel capillary tube 0.030 inch in diameter which serves to define the nozzle throat. The

nozzle is easily replaceable, and a second nozzle was in fact constructed with a throat diameter of 0.018 inch but was not used.

The gas stagnation temperature was monitored via a miniature Type J thermocouple mounted outside against the valve assembly near the region where the valve seats. The stagnation pressure was measured with a Bourdon tube mechanical pressure/vacuum gauge attached to a gas manifold. Cooling of the valve assembly, though possible through the use of an external dewar and conducting straps within the vacuum chamber, was never attempted.

The ions were produced at a high potential and then accelerated to ground. The nozzle and nozzle support plate were therefore electrically insulated from the vacuum chamber through the use of ceramic stand-offs. A Kepco APH1000M DC power supply and Lambda C-280M DC supply maintain the nozzle at +550 V. The skimmer potential is supplied in parallel with the nozzle voltage through a potentiometer and was typically reduced 5 V. The results of SIMION modeling of the electric field generated between the nozzle (and support plate) and the skimmer and ion optics face are shown in Figure 2-4.

E-Gun

The electron beam is generated continuously from a 0.005 inch diameter, 97% tungsten, 3% rhenium, coiled filament wire. The wire (total length of ~5 cm) was wound seven turns about a 0.040 inch diameter rod to create the coil. A current of 2 A was passed through the filament which was held at ~ +430V. The filament legs are inserted into stainless steel posts mounted within a MACOR cylinder fitted within a 3/8 inch o.d. stainless steel casing closed at one end by a thin stainless steel plate with a 1 mm slit. The casing and slit plate are at the same potential as the nozzle (+550V) and therefore the electrons emitted from the filament (positioned approximately 1 mm away from the slit) are accelerated to ~120 eV as they exit the slit. The electrons then drift across the nozzle

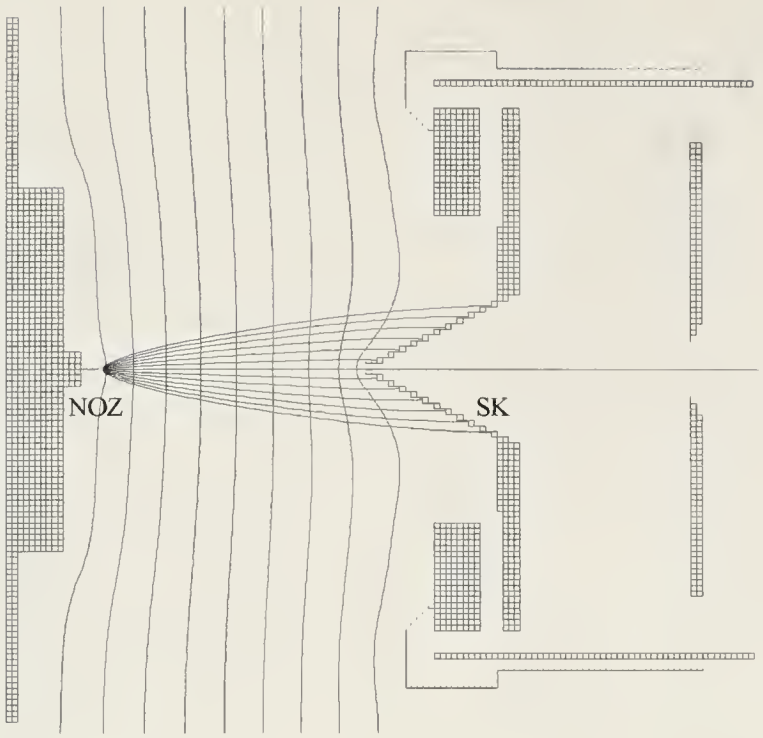

(a)

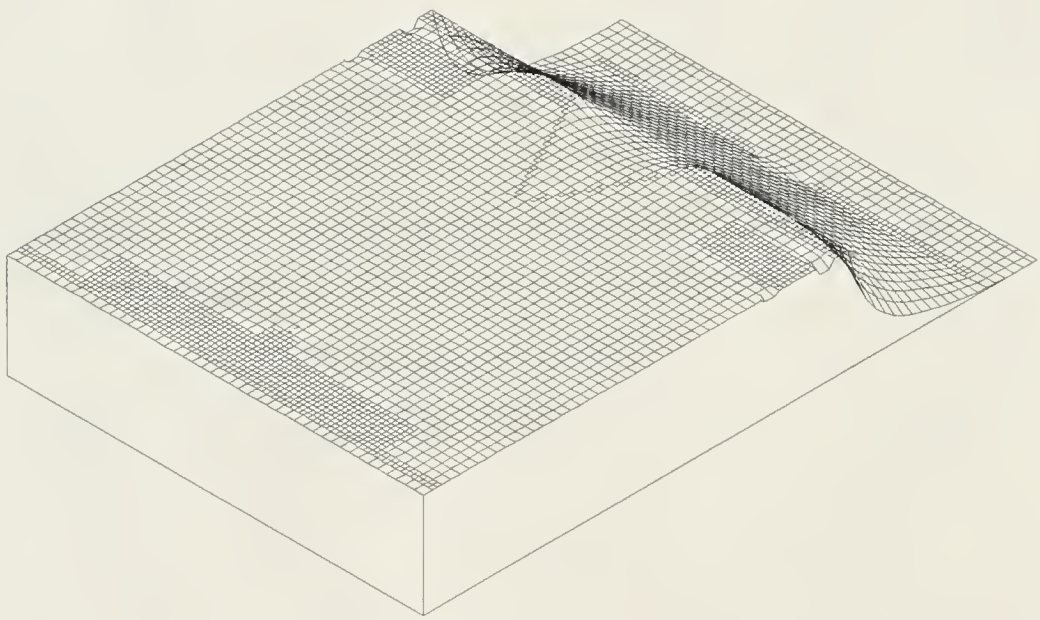

(b)

Figure 2-4 SIMION model of jet expansion region. (a) Ion trajectories from a 120° CO_2^+ jet spray ; Δ0.5 V contour lines show smooth E-field between nozzle (*NOZ*) and skimmer (*SK*); (b) 3-D view of potential surface; Nozzle potential = +550 V, skimmer = +545 V.

exit and are detected by a collector with essentially identical external geometry as the e-gun to minimize electric field perturbations near the nozzle. Electrical leads were also shielded to minimize field disturbances. Electron currents of 200 μA were measured under typical source operating conditions. Both the gun and collector can be moved radially and axially relative to the nozzle, but can only be adjusted with the system up to air.

Ion Optics

The central portion of the expanding jet flow is extracted through a standard Beam Dynamics conical nickel skimmer with a 2 mm entrance orifice located 4.7 cm downstream from the nozzle exit. The optics used to accelerate and focus of the beam are shown to scale in the SIMION simulations for two different operating configurations presented in Figures 2-5 and 2-6. The ion optics assembly end cap and face plate are held at the same potential as the skimmer (+545 V). The two Einzel lens voltages are supplied independently through two Ortec 556 HV power supplies. The potential applied to the four pairs of parallel plates can be varied individually by adjusting an array of eight precision potentiometers connected to two Kikusui PAB 250-0.25A DC power supplies. The plates are used for making small adjustments to the beam trajectory (steering). The last pair of plates is also used to modulate the pulsed cluster ion beam for introduction into the TOF mass spectrometer.

The electrical leads are supplied to each element internally (within the 4 inch o.d. stainless steel sleeve), but are insulated and shielded with Teflon spaghetti and 1/8 inch copper tubing. As previously mentioned, a 6 inch swing valve separates the ion optics from the mass spectrometer.

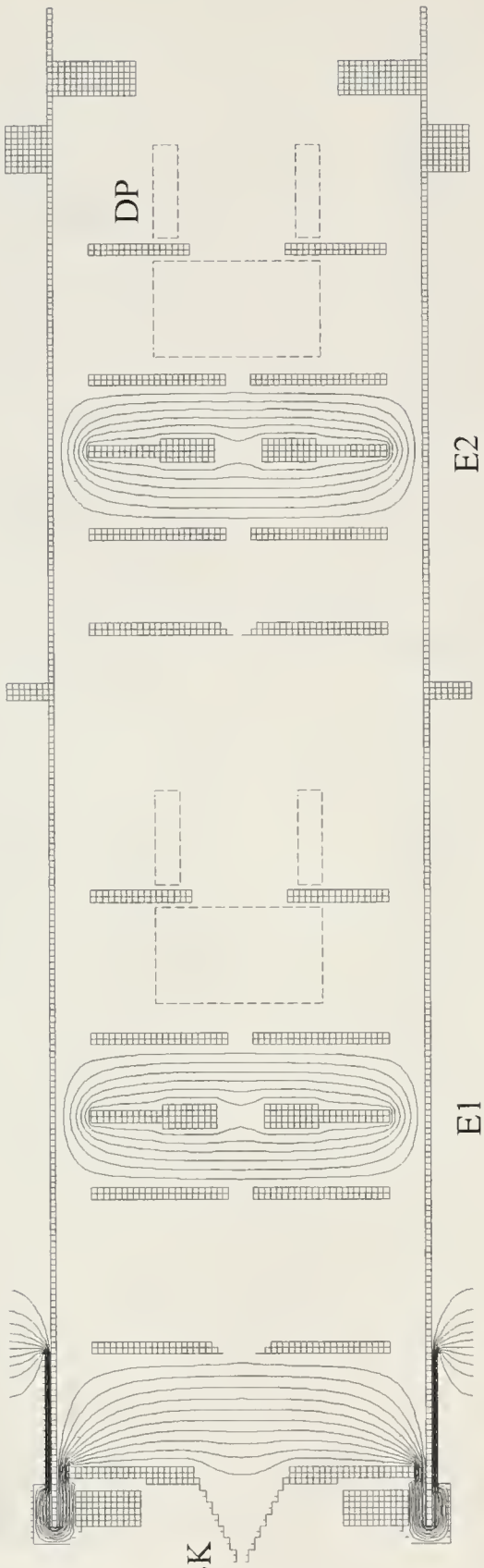

Figure 2-5(a) SIMION ion optics contour plot. Skimmer (*SK*) voltage = +545 V; Both Einzel lenses (*E1*, *E2*) = +340 V; Position of steering plates is indicated by dashes; The last pair of parallel plates function as deflection plates (*DP*); Δ50 V contour lines are also shown.

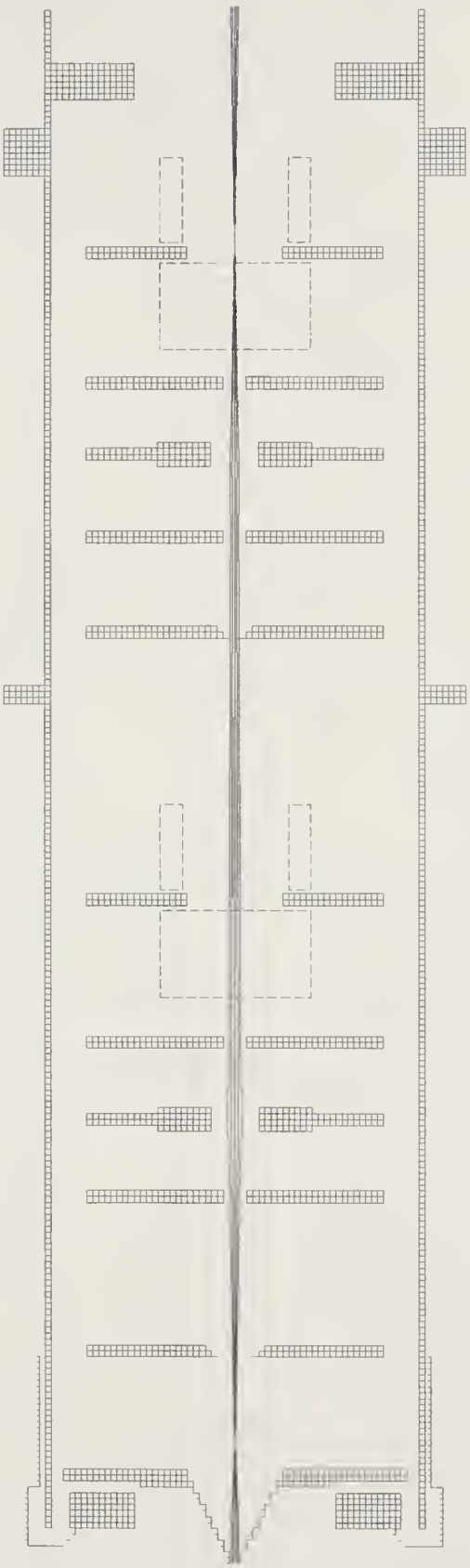

Figure 2-5(b) SIMION trajectory plot. Focusing of CO_2^+ beam is simulated; $SK = +545$ V, $E1 = E2 = +340$ V.

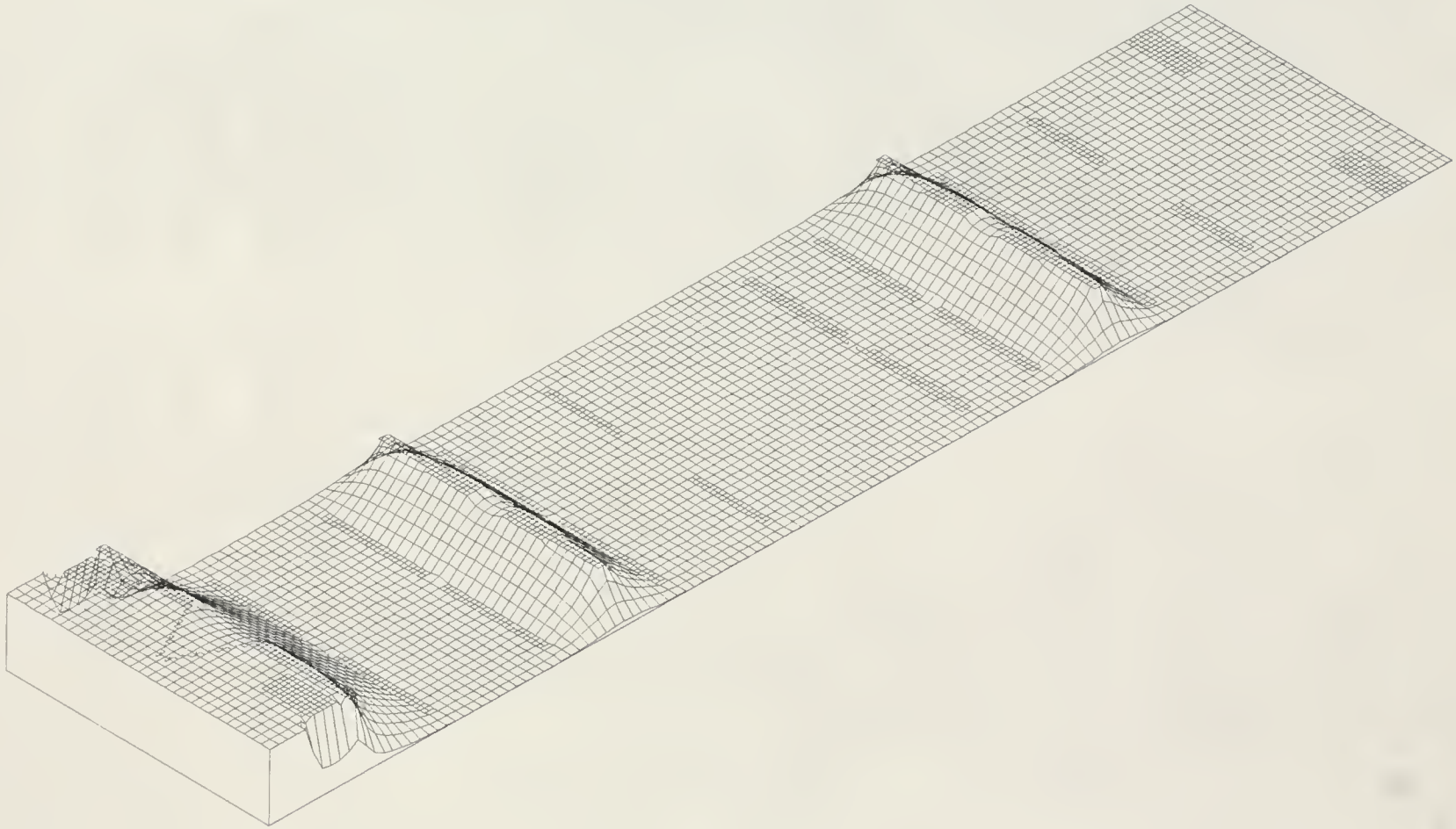

Figure 2-5(c) 3-D view of ion optics potential energy surface.

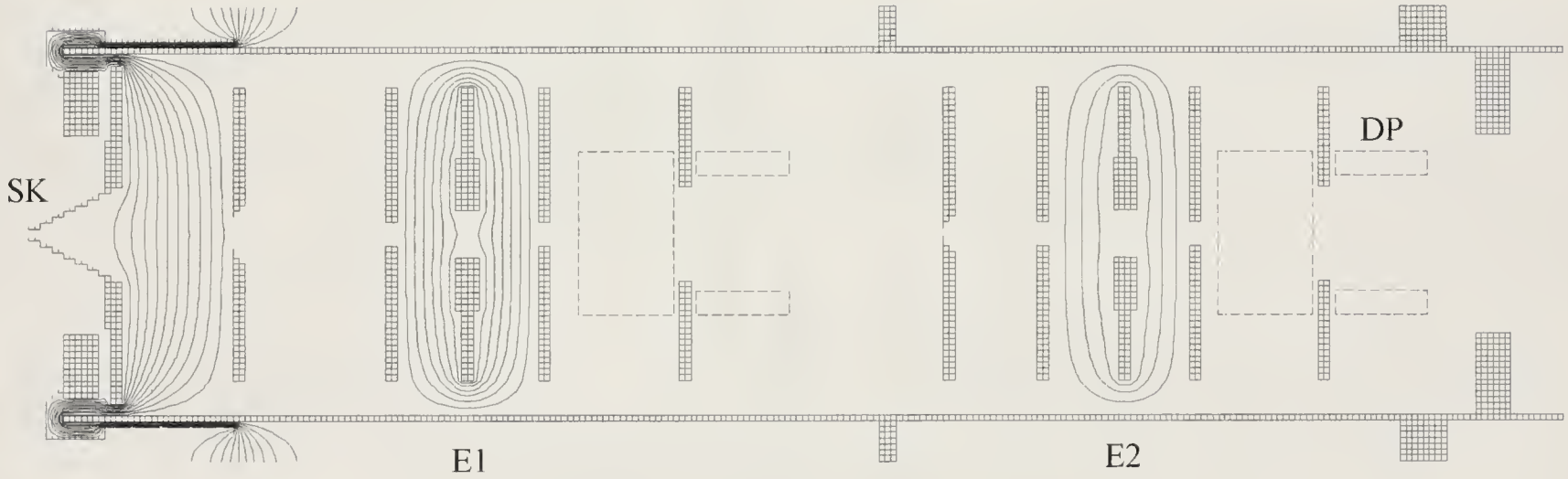

Figure 2-6(a) SIMION ion optics contour plot. Skimmer (*SK*) voltage = +545 V; *E1* = +340 V, *E2* = +200 V; Position of steering plates is indicated by dashes; The last pair of parallel plates function as deflection plates (*DP*); Δ50 V contour lines are also shown.

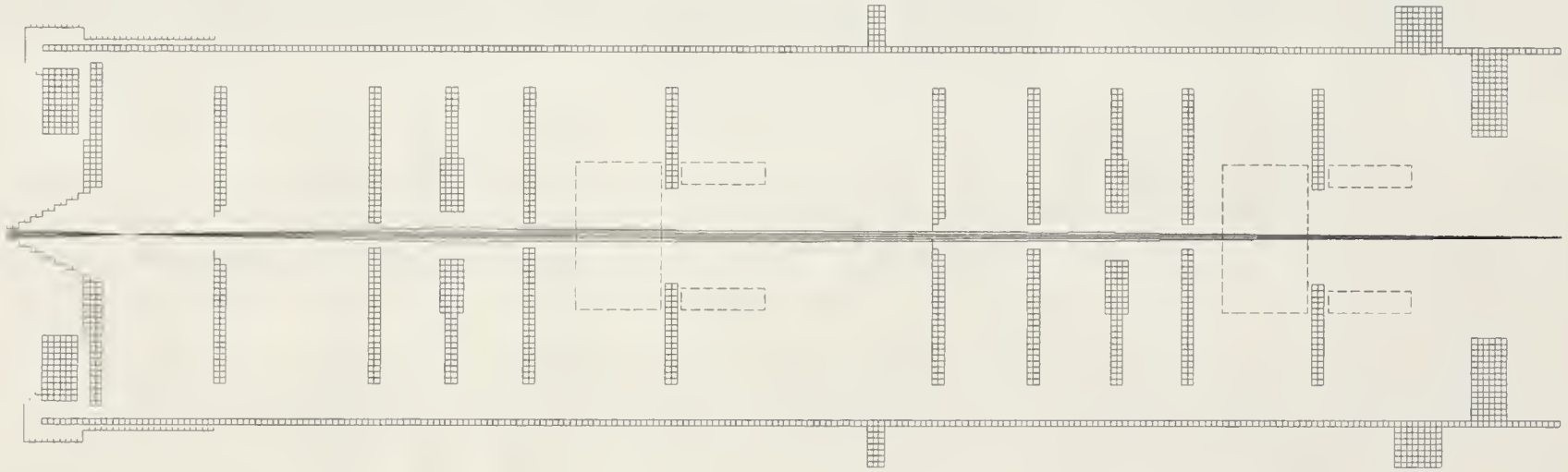

Figure 2-6(b) SIMION trajectory plot. Focusing of CO_2^+ beam is simulated; *SK* = +545 V, *E1* = +340 V, *E2* = +200 V.

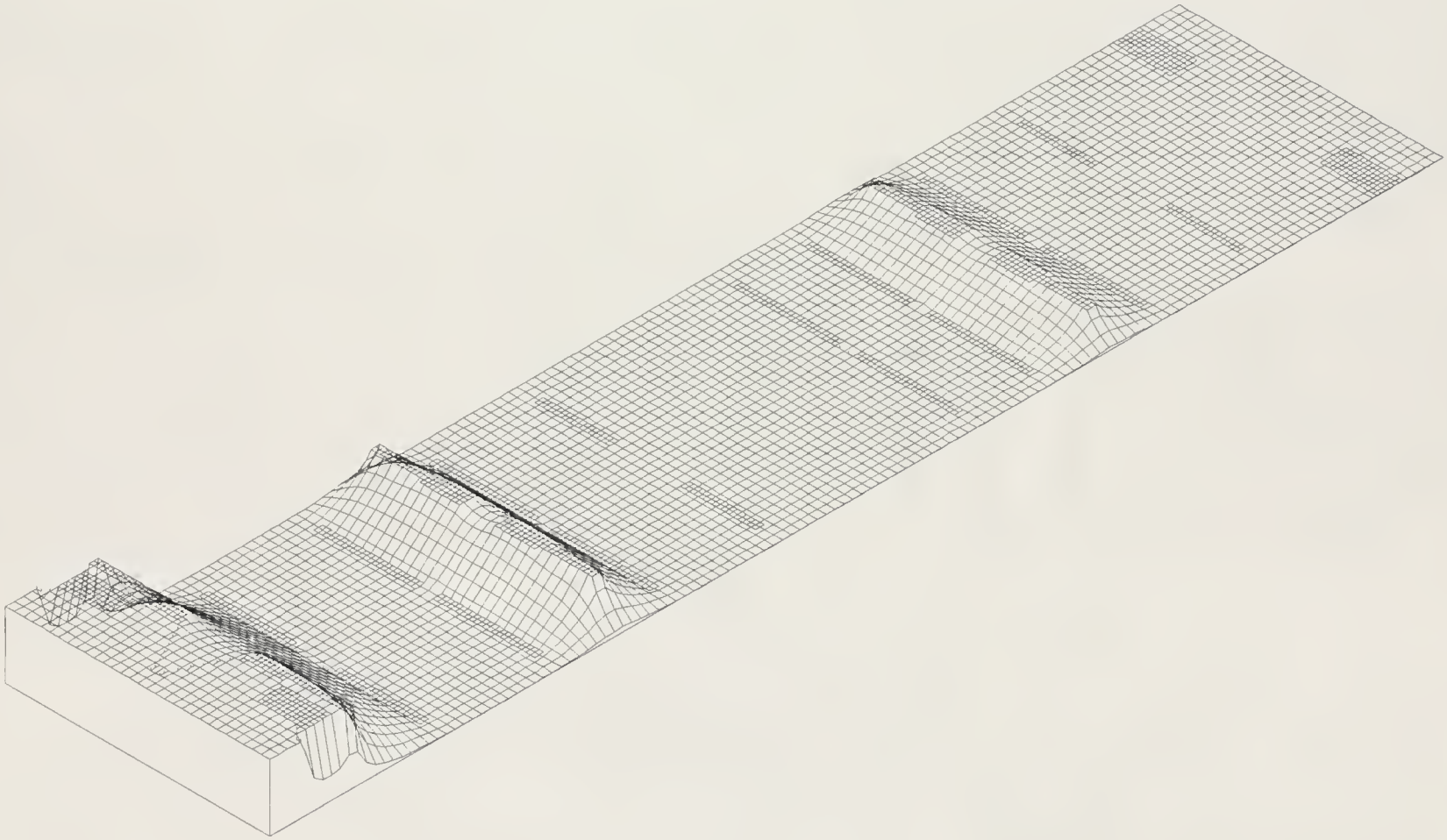

Figure 2-6(c) 3-D view of ion optics potential energy surface.

Mass Spectrometer

A top view of the mass spectrometer was shown in Figure 2-2. Pumping is provided by a Leybold-Heraeus TOPS 360 turbomolecular pumping system which consists primarily of a 360 L/s turbo pump backed by a dual stage rotary vane pump. Thermocouple, cold-cathode and Bayard-Alpert type ionization gauges near the detector end of the mass spectrometer supply pressure information. The slit is positioned 11 5/16 inches from the edge of the last set of parallel plates--the deflection plates. Titanium slits of 0.5, 1, 2, and 3 mm can be interchanged, but require the vacuum system to be interrupted to provide access. The vacuum envelope is defined by standard 4 inch o.d. stainless steel beam pipe.

General Configuration

Figure 2-7 shows the TOF components in greater detail. Ions enter a grounded, 47 inch long, 3/4 inch diameter stainless steel flight tube after traversing the velocity compaction region. The velocity compaction portion of the mass spectrometer was disabled for this work and was not used. As the ions exit the field free region inside the flight tube, they receive a final $\sim$2 kV acceleration before striking a stainless steel impact plate.

Detector

Secondary electrons generated by collision of the high velocity ions with the metal impact plate are collected and amplified by a stacked pair of Galileo chevron microchannel plates (MCP's) with an active diameter of 25 mm (see Figure 2-8). An electron trap consisting of a 90% transparent trap grid and stainless steel deflection screen enhance the

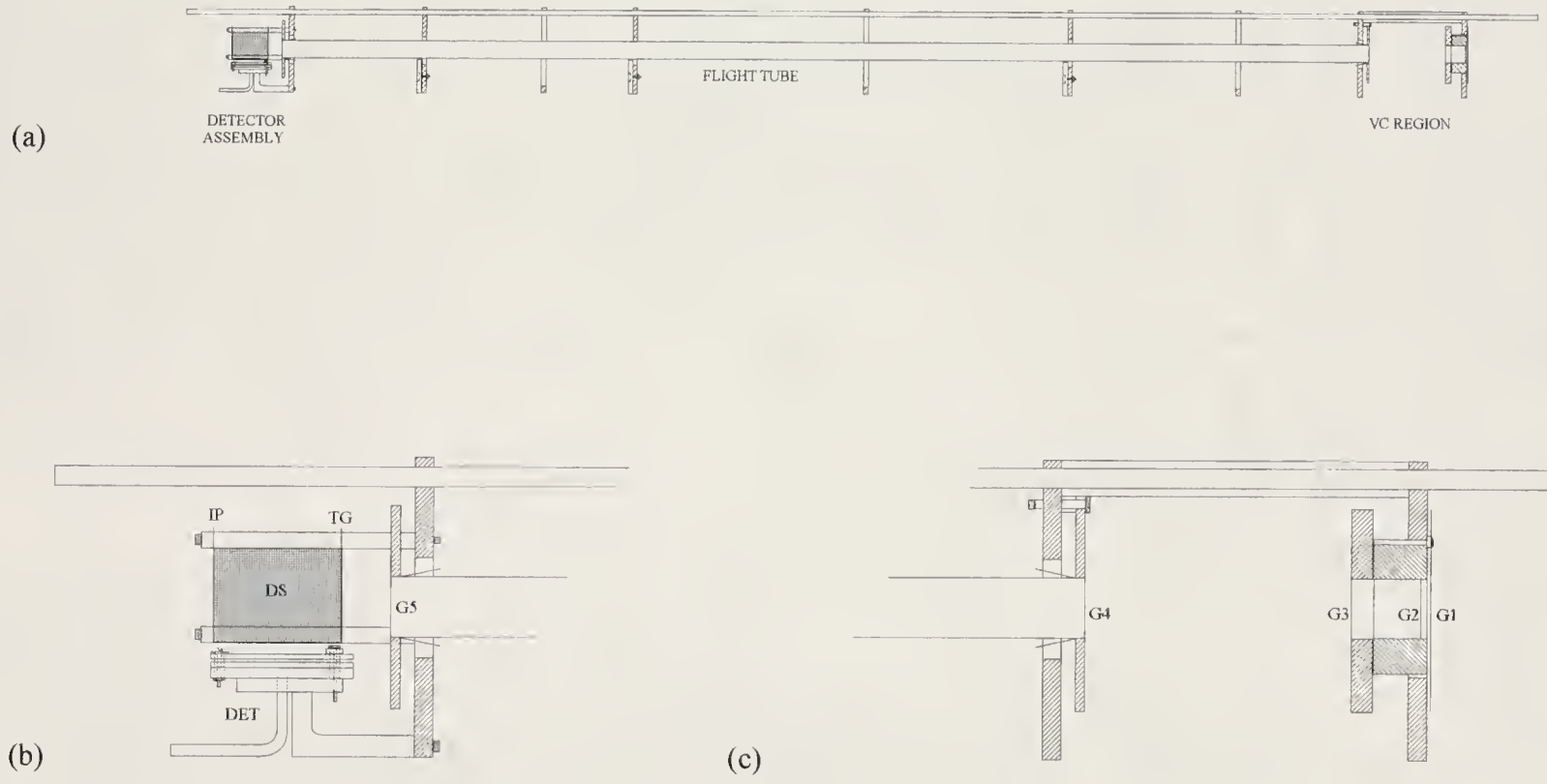

Figure 2-7 TOF mass spectrometer detail. (a) View of entire mass spectrometer; Drawn 1/8 scale; (b) Close up view (3×) of detector assembly; *IP* = Impact Plate, *TG* = Trap Grid, *DS* = Deflection Screen, *DET* = Detector; (c) Close up view (3×) of velocity compaction region; *G1* - *G5* indicate positions of 90% transparent grids, each at ground potential.

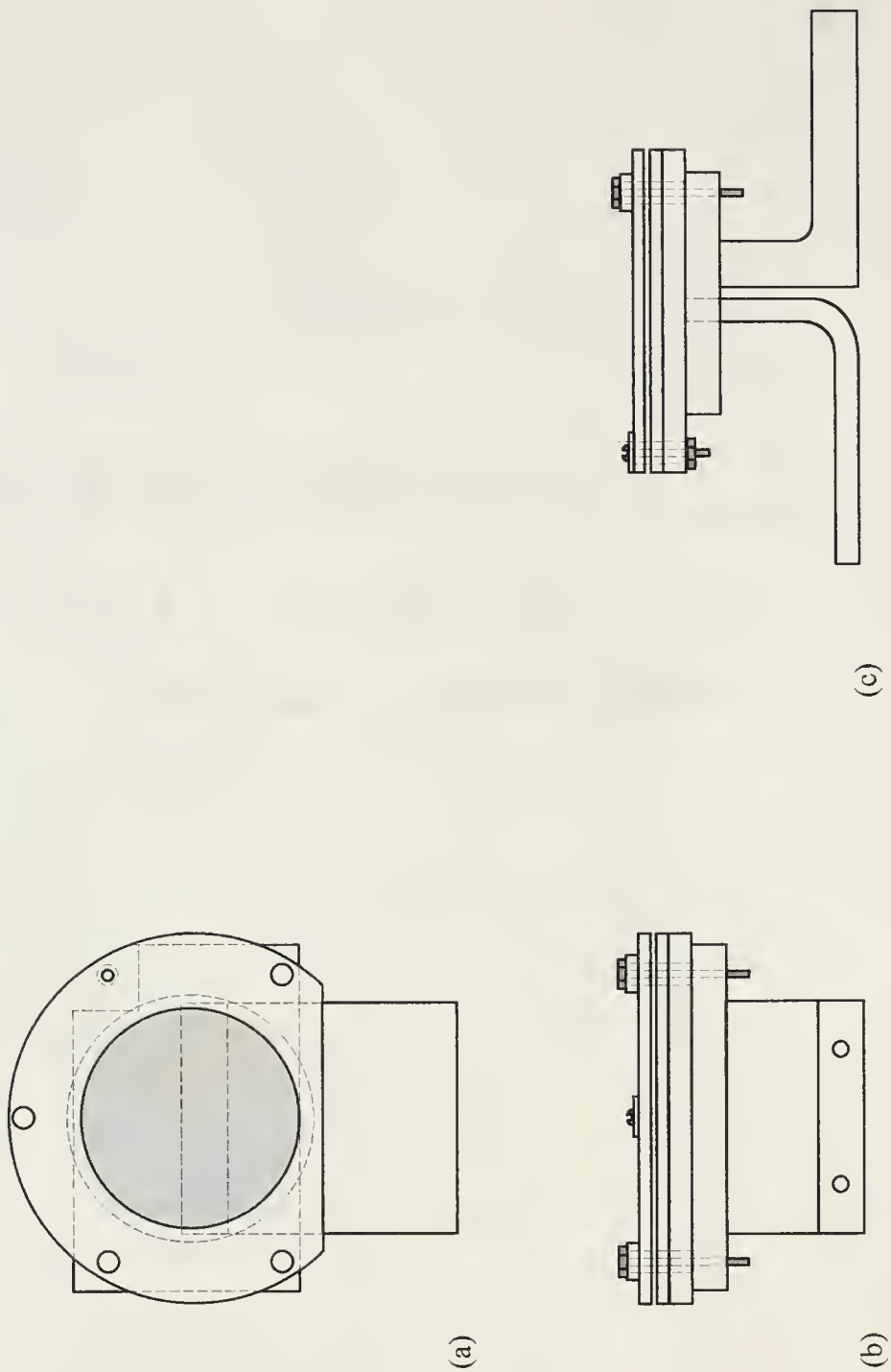

Figure 2-8 MCP assembly. (a) top view, (b) front view, and (c) side view. Drawn full scale.

collection efficiency. The trap grid and deflection canopy are kept at −1.9 kV by an Ortec 556 HV power supply. The impact plate, first MCP, and second MCP are each operated at −1.9 kV, −1.7 kV, and −0.1 kV, respectively, through a resistor string supplied by a separate Ortec 556 power supply.

SIMION negative ion potential energy plots are presented in Figure 2-9, and simulations for a 550 eV CO_2^+ beam impact and subsequent detection of secondary ions ranging from thermal energies to 10 eV are shown Figure 2-10.

The two-stage MCP configuration, operated with an 1.6 kV applied voltage differential, produces approximately a 10^6 output gain.[54] The detector signal is supplied through a partially shielded lead to a standard BNC connector. Additional amplification of the signal is provided by an Ortec 535 quad fast amplifier. The inverted signal is then supplied to a LeCroy 9400, 125 MHz digital storage oscilloscope (DSO). Triggering and other timing aspects associated with data collection are discussed in the next chapter.

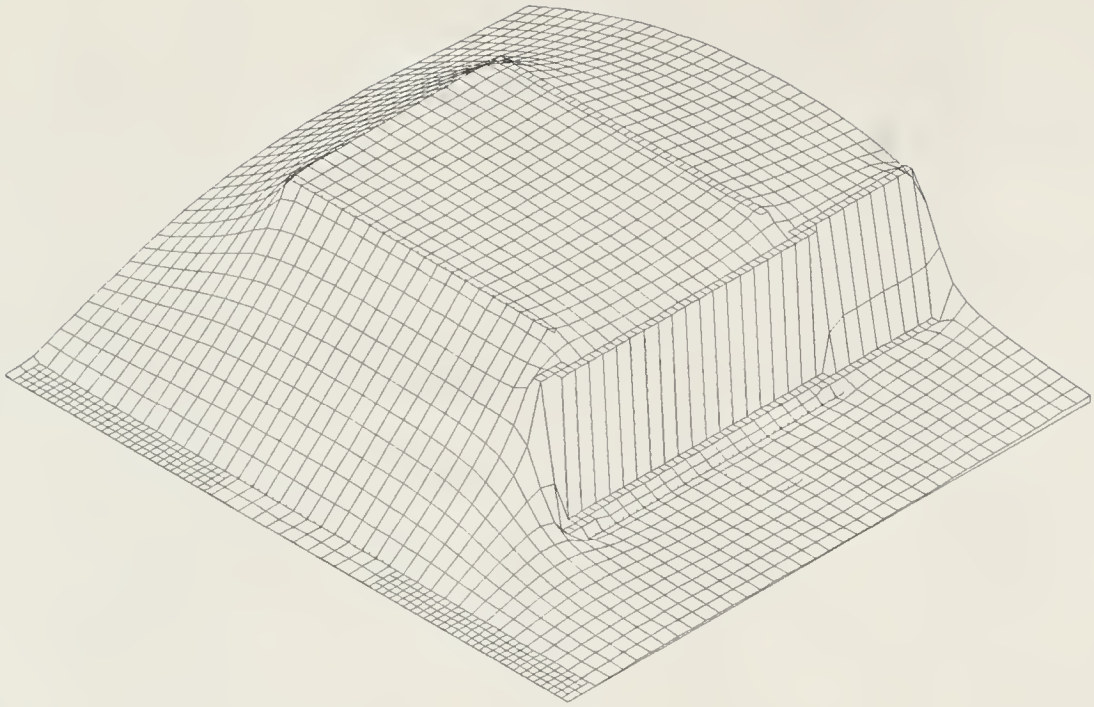

(a)

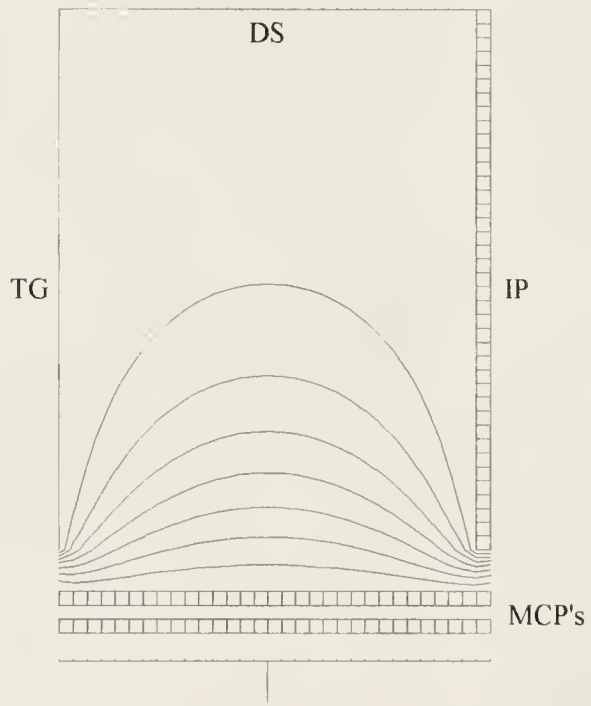

(b)

Figure 2-9 SIMION plots of (a) detector 3-D negative ion potential energy surface, and (b) Δ25 V contour lines in the electron trap region; Deflection Screen (*DS*) = Trap Grid (*TG*) = Impact Plate (*IP*)= -1900 V; Top MCP = -1700 V; Bottom MCP = -100 V.

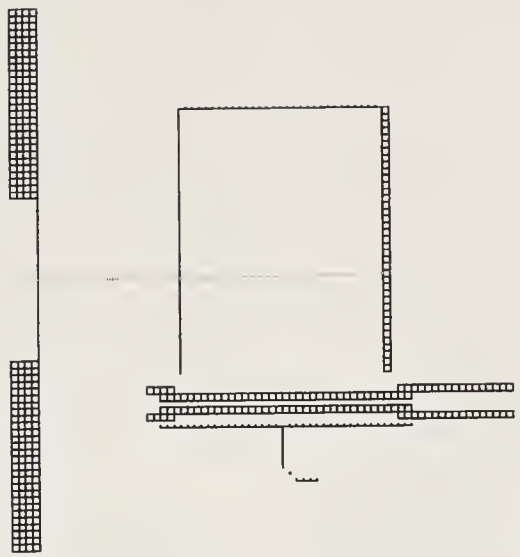

(a) 550 eV CO_2^+ beam

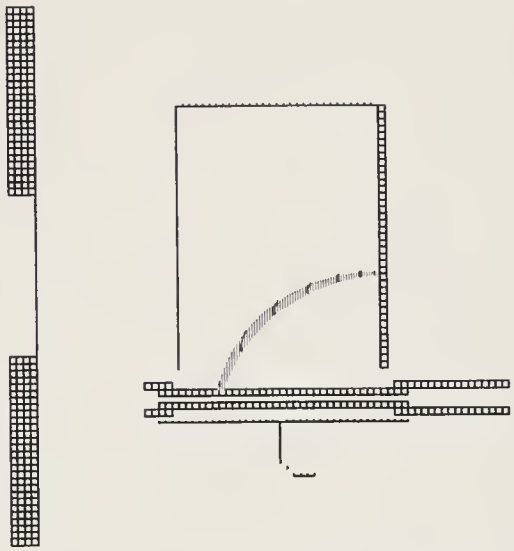

(b) 0.025 eV electrons

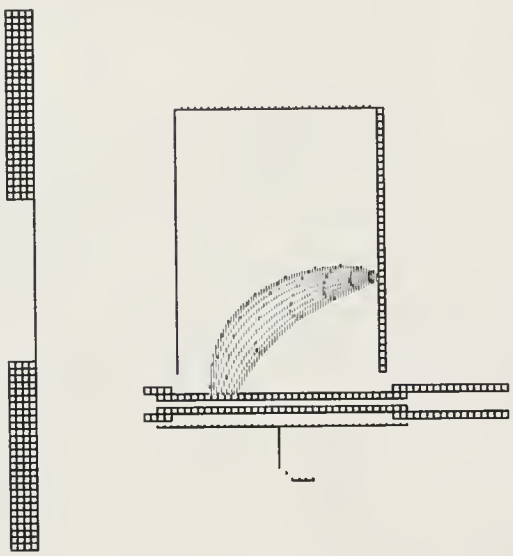

(c) 1 eV electrons

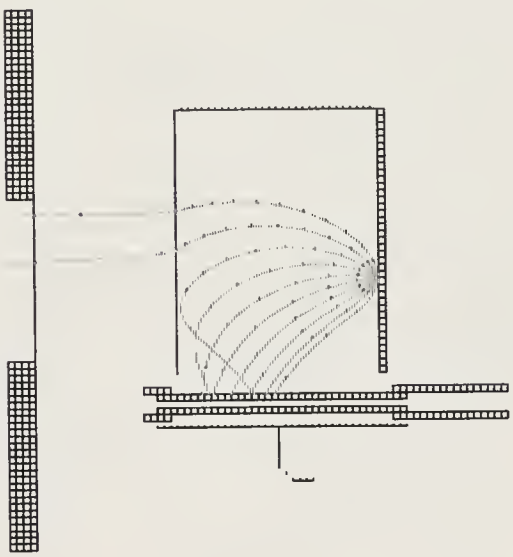

(d) 10 eV electrons

Figure 2-10 SIMION simulation of (a) 550 eV CO_2^+ beam impact with deflection plate (1/64 inch deflection noted); (b) through (d) depict the collection efficiency of the trap for stated e^- energies with an initial 180° angular dispersion. Ticks are 1 ns timing marks.

CHAPTER 3
BEAM DEFLECTION TIME-OF-FLIGHT MASS SPECTROMETRY

Introduction

A First Order Model

In 1973, J. M. B. Bakker[55] published the first paper addressing the theory of beam deflection as a technique to modulate a continuous ion beam for introduction into a TOF mass spectrometer. His elegant treatment of this rather complex topic continues to provide valuable insight into the behavior of ions as they move through a rapidly changing electric field perpendicular to the beam axis. Bakker described the modulation process in terms of a 'kink' introduced into a homogeneous beam of ions initially deflected downwards as it passes through an electrical field which suddenly experiences an inversion in the electric field which then deflects the beam upwards.

The ion beam profile for this model is shown in Figure 3-1. The kink lies between *e*-*e* and *a*-*a* and travels from left to right at the same velocity as the rest of the ion beam while simultaneously expanding in both the upward and downward directions. The *e* ions have the largest upward velocity component while the *a* ions have the largest downward velocity. Ions at the center of the kink possess little or no velocity component in the up or down direction. Of the ions affected by the step-function controlled electric field, only the ions within the boundary d_0-c_0-b_0-c_0 will actually pass through the slit *S*. Finally, it should also be noted that the velocity of the ions from left to right is unaffected by the

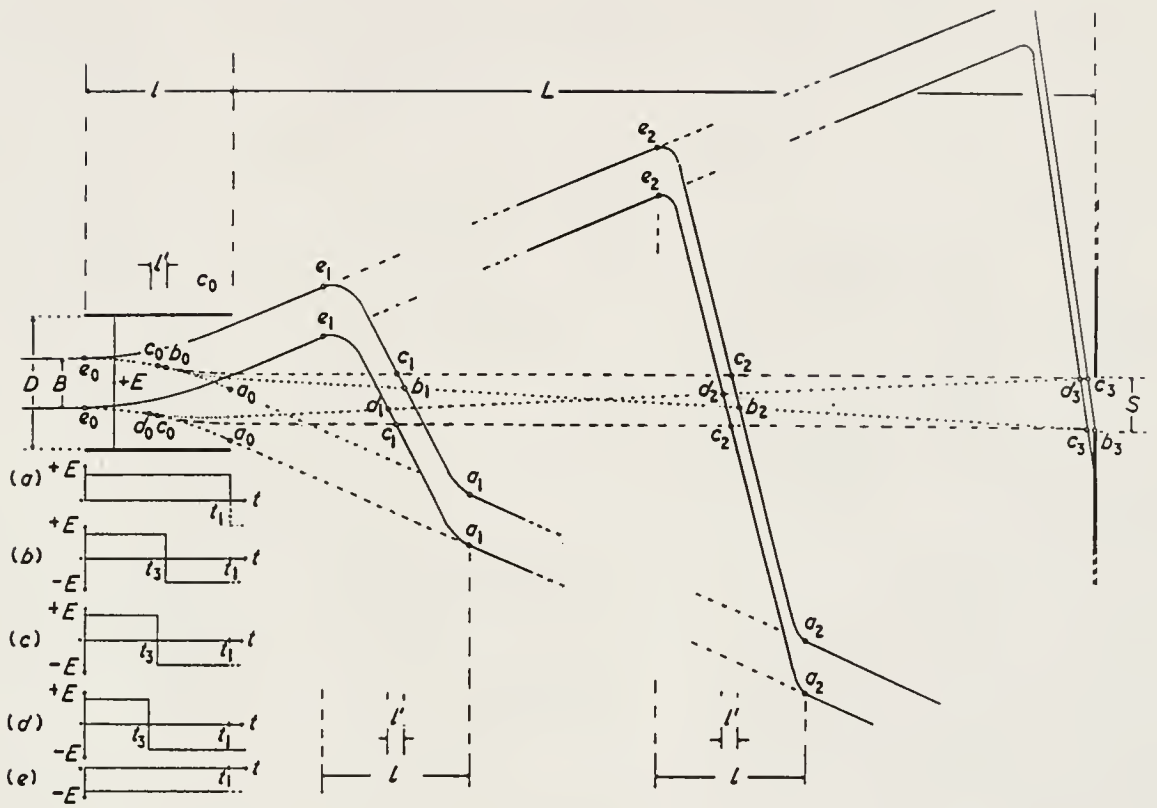

Figure 3-1 A monoenergetic ion beam of width B and consisting of ions with mass m and energy eU_1 traverses an electrical field of strength E controlled by a step function and produced between deflection plates of length l and separation D. The ions then travel through a field free space L until they reach a slit S. The position of eight ions at time T_0 (when the electrical field changes instantaneously) is indicated by a_0, a_0, b_0, c_0, c_0, d_0, e_0 and e_0. The electrical field experienced by these ions as they travel between the deflection plates is a function of their positions at time T_0, and the field profile for the a_0 ions is shown by Figure 3-1(a). Figure 3-1(b) shows the field encountered by the b_0 ion, and etc. The ion positions are shown for three consecutive instants of time, t_1, t_2 and t_3, after the field change, and are designated by corresponding subscripts. Note: the figure can also be interpreted as showing the relative positions of three monoenergetic ion beams with different masses at one instant of time, i.e. b_3-c_3-d_3-c_3 represents a packet of very light ions, b_2-c_2-d_2-c_2 represents a packet of medium weight ions, and b_1-c_1-d_1-c_1 represents a packet of very heavy ions. (Taken from Bakker.[55])

perpendicular electric field, and therefore the projected distances $e - a = l$ and $d - b = l'$ are constants.

Bakker not only provided a qualitative model of the beam modulation process, but he also derived expressions for the ion burst duration (pulse base width), resolution, and relative ion intensity for a theoretical beam-modulated TOF mass spectrometer (cf. Table 3-1). His treatment, however, was restricted to three distinct cases; the first (Table 3-1(a)) treats the idealized case of an instantaneous reversal in the electric field polarity, the second case deals with the more likely situation in which the deflection plate voltage, and thus the electric field, changes rapidly with respect to the transit time of the ions through the plates (Table 3-1(b)), and the final case (Table 3-1(c)) addresses the situation where the transit time is shorter than the time required to invert the electric field. Many of the equations are not exact solutions, but are approximations based on certain stated assumptions.

Table 3-1 Summary of Bakker Results

Waveform $V(t)$	Ion burst duration Δt (general)	Δt ($t_2 \gg t_1$)	Resolution $R = t_2/2\Delta t$ Ion intensity $I \propto \Delta t/t_1$
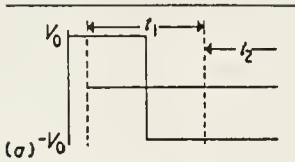	$\dfrac{(B+S)\,mD}{eV_0(2t_1^2+4t_1t_2+4t_2^2)^{1/2}}$	$\dfrac{(B+S)\,mD}{2eV_0t_2}$	$R=\dfrac{V_0L^2}{2DU(B+S)}=C_1$ $I\propto\dfrac{(B+S)\,DU}{V_0lL}$ $I=C_2$
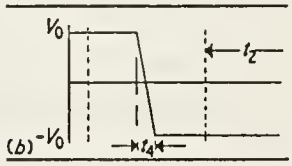	$\dfrac{(B+S)\,mD}{eV_0(2t_1^2+4t_1t_2+4t_2^2-\frac{1}{3}t_4^2)^{1/2}}$ $t_4<\frac{1}{3}t_1$	$\dfrac{(B+S)\,mD}{2eV_0t_2}$	$R=C_1$ $I=C_2$
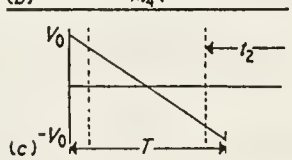	$\dfrac{2(B+S)\,mDT}{eV_0t_1(t_1+2t_2)}$ $T>t_1$	$\dfrac{(B+S)\,mDT}{eV_0t_1t_2}$	$R=\dfrac{t_1}{2T}C_1=\dfrac{l}{2T}\left(\dfrac{m}{2eU}\right)^{1/2}C_1$ $R=f(m^{1/2})$ $I=f(m^{-1/2})$

Bakker concluded that a beam-modulated TOF instrument operating in the regime described by the first two cases would have a resolution independent of ion mass, independent of the location where the ions were initially formed, and proportional to the square of the length on the drift space. In 1974, Baker[56] reported the construction of a beam-modulated TOF mass spectrometer, and provided an experimental confirmation of his theory.

A Modified Bakker's Model

Two attempts to refine Bakker's theory have been published recently.[57,58] Yefchak et al. explored the added effects of energy spread and angular divergence of the beam via a computer simulation. Approximate peak widths were calculated for the Bakker effect alone, the Bakker effect with energy dispersion, the Bakker effect with angular divergence, and all effects combined. The program modeled the motion of various ions by means of Runge-Kutta integration through the deflection plate region and onward to the aperture. Flight times for those ions found to pass through the aperture were added in the form of a histogram to generate a peak shape. According to Yefchak et al., the simulated peak variances were not well characterized, but were believed to fall within a few percent of the true values. The Bakker equations shown in Table 3-1(b) provided the mathematical basis for all of these calculations.

Ce Ma et al. also developed a computer simulation, based on simplified equations much like those of Bakker, to model the case when the voltage rise time on the deflector plate is short in comparison with the transit time of the ions between the plates (cf. Table 3-1(b)). The simulation was used to establish the m/z independence of the ion packet width, and to investigate the effects of varying the deflection plate voltage, the deflection voltage rise time, and the initial beam acceleration voltage on the ion packet width when the ion beam is swept past the slit; the slit was positioned near the entrance to the TOF

mass spectrometer rather than near the detector as with Bakker's work. Ce Ma et al. also investigated the effect of a Gaussian energy distribution on the ion peak width using a Monte Carlo method. Since no shutter function was included in any of these simulations, the peak width data pertained to base peak width. No pulse shape information was generated.

Applications

Beam deflection was first used in connection with TOF mass spectrometry as a simple gate. Futrell et al.[59,60] were among the first to use a deflection plate to reduce baseline noise caused by stray ions from a continuous high pressure ion source which enter the drift region between pulsed extractions and are accelerated down the flight tube. Glish and Goeringer[61] installed a set of deflector plates in a tandem quadrupole/TOF mass spectrometer used to study collision activated dissociations; these deflectors were used to gate the ions exiting the collision cell into the drift region for TOF analysis.

Since beam deflection provides an excellent method for sampling a continuous ion source, or a source which cannot be pulsed sufficiently fast for TOF measurements, it is beginning to find more and more applications--especially among analytical chemists. Beam deflection techniques have been successfully applied in tandem magnetic sector/TOF mass spectrometry by Enke's group at Michigan State University.[62,63] Pinkston et al.[64] recognized the advantages of beam deflection for ion pulse formation, and incorporated the technique into an electric sector/TOF mass spectrometer. Very recent applications include the design of an atmospheric pressure ionization/TOF mass spectrometer using a beam deflection method,[58] and the combination of gas chromatography with beam deflection TOF mass spectrometry.[57,65,66]

No doubt, the utilization of beam deflection techniques will continue to grow in the future as the need to "chop" continuous, or slowly pulsed ion beams increases.

However, the development of a more comprehensive theoretical model would certainly facilitate the prudent application of this sampling method. Bakker's model continues to serve well as long as a given instrument is designed and operated within one of the regimes where the equations apply. But what about when they do not apply? For instance, the case where the rise time of the voltage on the deflection plates is about the same as the transit time of the ions has not previously been treated. Additionally, since the ion transit time is mass dependent, it is conceivable that over a large mass range some of the ions might fall within one regime while others do not. In short, a more rigorous mathematical treatment is needed.

The novel application of beam deflection methods to chop an EI ionized, pulsed cluster ion source for TOF analysis is detailed below, along with the development of a more rigorous computational model.

Approach

Experiment

The basic components of the cluster ion source and mass spectrometer were described at length in Chapter 2. This discussion, therefore, will be limited to the beam deflection hardware and support equipment.

The last pair of steering plates (cf. Figure 2-5) in the ion optics assembly was also utilized for beam deflection; the high voltage pulse needed to sweep the beam back and forth across the slit was superimposed upon the experimentally determined steering voltage required for proper alignment of the beam. A schematic diagram of the basic experimental configuration along with typical operating parameters is shown in Figure 3-2.

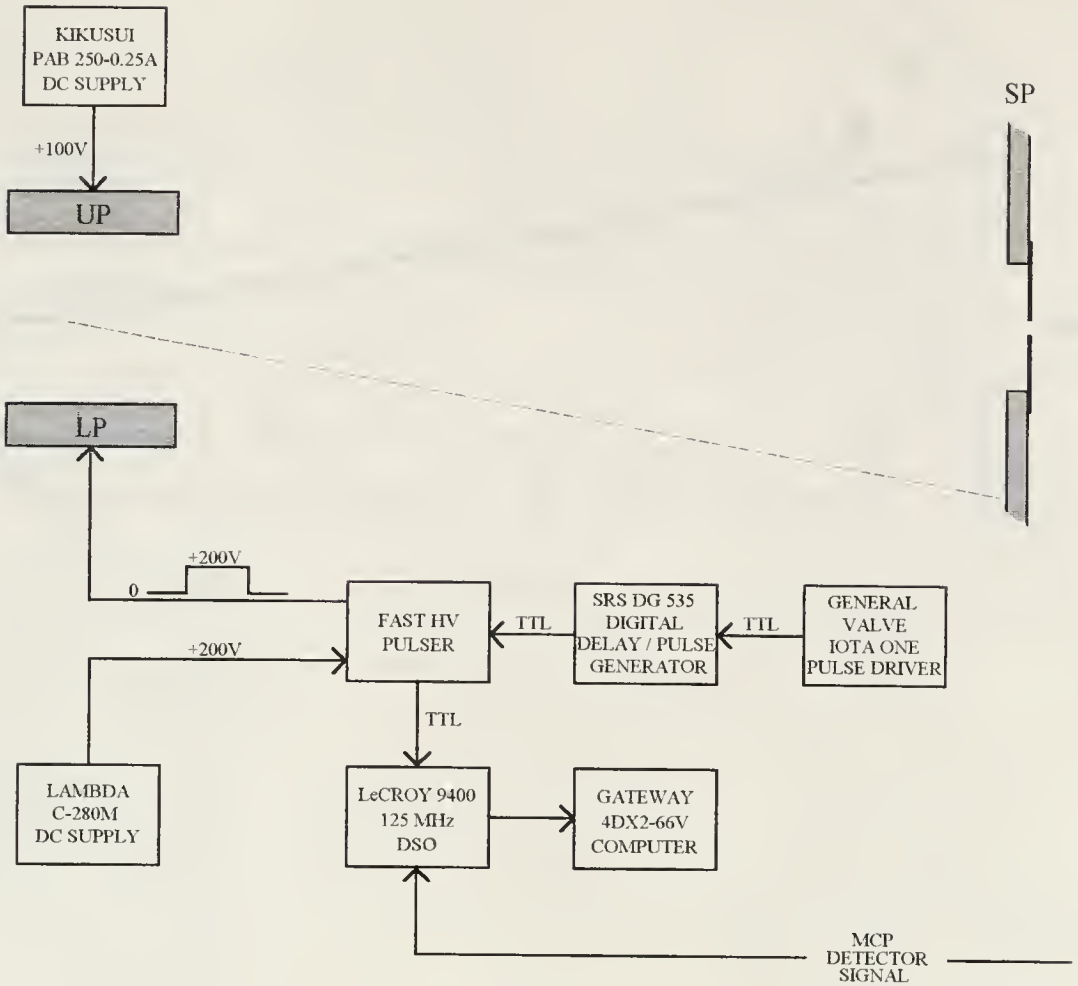

Figure 3-2 Beam deflection schematic. The Fast HV Pulser switches +200 V on and off the lower plate (*LP*) while a constant +100 V is applied to the upper plate (*UP*). Each sweep is initiated by a TTL pulse from the pulse driver. The slit plate (*SP*) is located 38.7 cm from the deflection plates, and the detector (not shown) is positioned 151.4 cm to the right of the slit.

The beam is bent by the variable electric field generated between the two parallel plates as the square wave is applied to the lower plate; the parallel plates are separated by a distance of one inch and are both one inch in length. The beam is then chopped by an interchangeable slit located 28.7 cm away from the deflection plates, and the resulting beamlet then enters a field free drift region. While traversing the drift tube, the chopped

beamlet separates into individual isomass packets which are finally detected by a stacked pair of microchannel plates located at the end of the flight tube (cf. Chapter 2). The timing is critical in this chopping process since the ion beam is not continuous, but is in fact mechanically pulsed. However, since the pulse duration is long (nominally a few hundred microseconds) compared to the time slice chopped out of the pulse (a few hundred nanoseconds or less) it is only necessary to synchronize the voltage swing so as to coincide with the pulse arrival time over the parallel plates. Ideally the slice should be taken from the middle of the beam pulse, thus avoiding the edges which were produced during non-equilibrium flow conditions in the nozzle.

By adjusting the delay from the SRS pulse generator, it is possible to control where the slice will be taken within the beam pulse. This truly unique feature makes it possible to study the spatial and temporal composition of beam pulses by taking mass spectral cross-sections at arbitrary positions along the entire length of the ion beam pulse. Just such a study was performed with CO_2 and is presented in Chapter 4.

The upper plate is held at a constant +100 V while the lower plate voltage is driven by a square wave of +200 V amplitude. The rise time (10 - 90%) of the leading edge of the square wave can be varied continuously from 30 to 2200 ns through the use of a novel fast switching circuit.[67] The schematic diagram is provided in Figure 3-3.

The electric field potential between the plates for the two limiting conditions, i.e. when the lower plate voltage is 0 V, and when it is +200 V, was modeled using SIMION and the results are shown graphically in Figure 3-4. It should be noted that significant fringing fields are predicted to exist. Ion beam trajectories were also computed and are presented in Figure 3-5. Because of the asymmetries involved with the electric field lines, as well as the difference in the rise and decay times of the high voltage square wave, only beam sweeps originating from the leading or rising edge of the wave (sweeps from bottom to top) were used to acquire mass spectra. Thus, when the high voltage is switched on, a TTL pulse from the Fast HV Pulser is used to trigger a LeCroy 125 MHz DSO which

captures the TOF spectrum and holds it until queried by a Gateway 2000 4DX2-66V computer via a National Instruments GPIB interface. These single-shot spectra are then added together to build the final mass spectrum. The entire beam deflection and data acquisition process is slaved to the pulse driver TTL output. The digital accumulation and final display of the summed spectra are controlled through software developed by David J. Burnsed.[68]

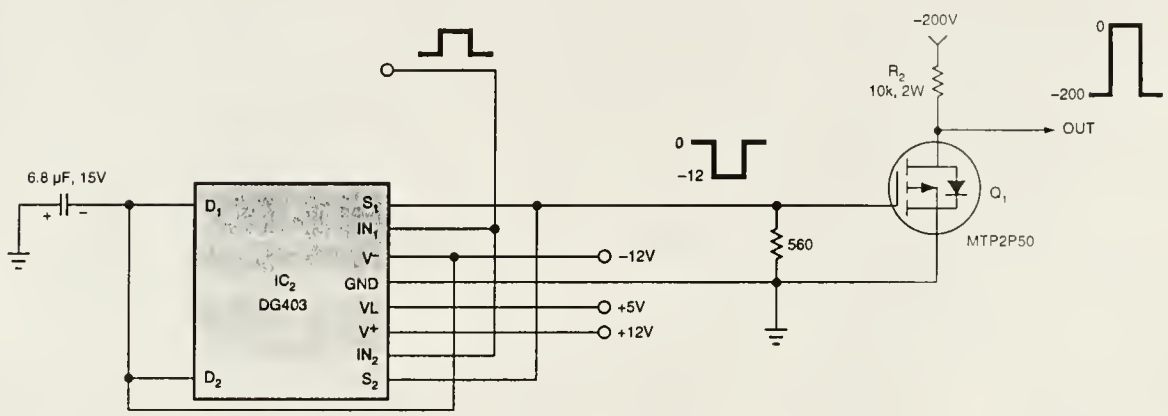

Figure 3-3 Fast HV Pulser switching circuit. A regulated power supply (not shown) provides the constant current needed to quickly charge the considerable input capacitance of the power MOSFET Q_1. A dual analog switch, with its two switches paralleled to reduce switching times, couples the supply to the MOSFET's gate on command. A TTL signal applied to the analog switch's IN_1 and IN_2 pins connects the -12 V supply applied to the switch's D_1 and D_2 inputs to its S_1 and S_2 outputs. The analog switch's outputs connect the MOSFET's gate, switching 200 V in nanoseconds (the pulse rise time, t_r = 32 ns and the fall time, t_f = 1400 ns). Note: varying R_2 affects t_r and t_f. (Taken from Burnsed.[67])

Figure 3-4 SIMION model of static beam deflection E-fields. (a) depicts the initial field conditions prior to the HV square wave; upper plate (*UP*) = +100 V and the lower plate (*LP*) = 0 V; (b) depicts the final field conditions after the lower plate has reached the maximum potential; *UP* = +100 V and *LP* = +200 V; Contours lines are shown for Δ10 V changes in the E-field; *SP* = Slit Plate.

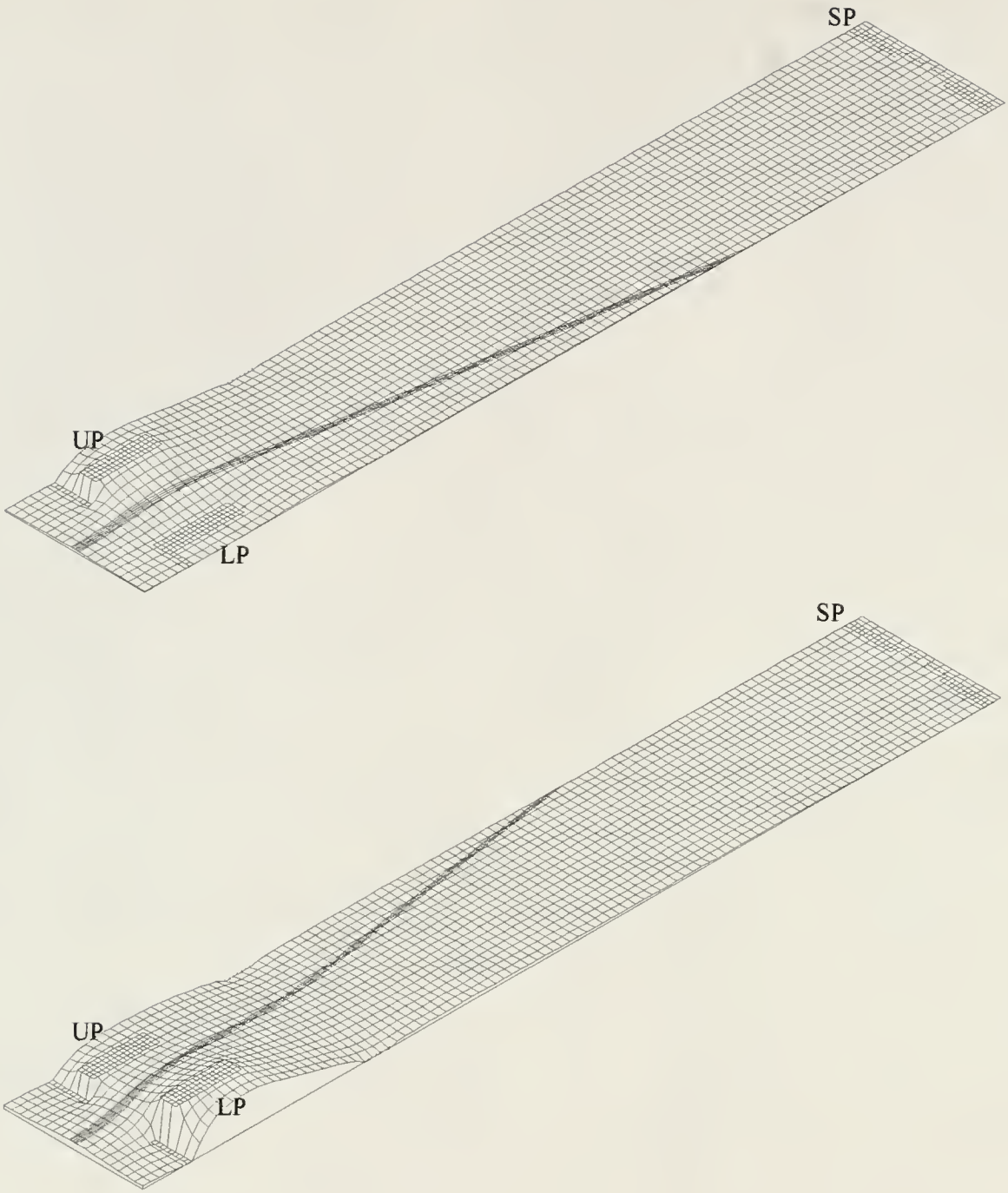

Figure 3-5 SIMION beam trajectories and 3-D view of the potential energy surface. (a) *y* displacement of 550 eV, 2 mm diameter ion beam when the Upper Plate (*UP*) voltage = +100 V and the Lower Plate (*LP*) voltage = 0 V; (b) displacement of the beam when *UP* = +100 V and *LP* = +200 V. *SP* = Slit Plate.

Theory

A computer code was developed to model the behavior of ions traversing the beam deflection TOF mass spectrometer. Unlike previous efforts, the goal from the very outset was to create a robust algorithm which could accurately describe ion trajectories, and predict the flight time and pulse shape of any given isomass packet for virtually any conceivable experimental configuration. To accomplish this, equations of motion were derived from first principles which address the variable electric field conditions encountered between the parallel plates as the applied voltage changes. Additionally, the velocity distribution within an isomass packet was modeled with a one-dimensional Boltzmann distribution, and a shutter function was constructed to describe the relative ion flux transmitted by a slit as a cylindrical beam is swept across it. The detailed mathematical treatment of these topics is provided in Appendix A.

Once the proper equations were in hand, the next step was to find general solutions within the constraints imposed by realistic beam deflection TOF mass spectrometer designs. A numerical approach was taken, thus a computer code was written to model ion beam behavior under a wide set of user defined conditions. The primary goals while encoding the program were to keep it completely general (i.e. not restricted to Bakker's three cases) while at the same time providing rigorously correct solutions, and to allow for maximum flexibility through numerous user defined parameters.

TRAJION substantially meets these goals. Programmed in PASCAL, TRAJION makes good use of the top-down programming technique; the highly structured PASCAL environment proved ideal for solving the complex beam deflection problem through the stepwise implementation of several procedures which address independent subproblems. TRAJION consists of six procedures and one relatively short main program segment. A flow chart detailing the general procedure call logic is shown in Figure 3-6. The complete source code is provided in Appendix B.

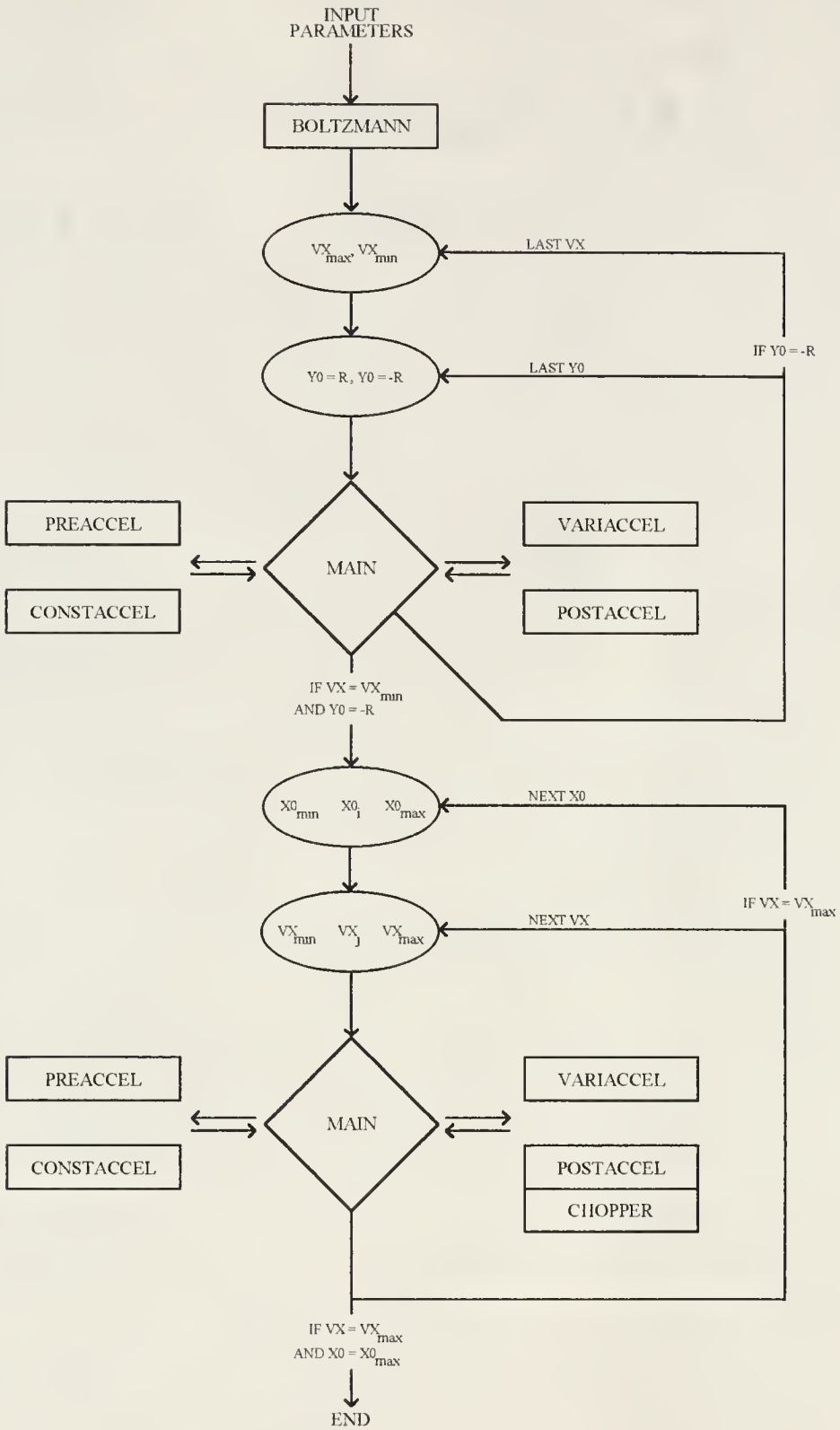

Figure 3-6 Simplified TRAJION flow chart. Procedures are indicated by rectangles.

Input parameters are supplied in part through nine user defined constants: 1) *XB*, the length of the parallel plates, 2) *XC*, the distance separating the parallel plates and slit, 3) *XD*, the distance separating the slit and detector, 4) *D*, the distance between the parallel plates, 5) *E*, the slit width, 6) *TAU*, the plate voltage decay time (Note: TRAJION solves the case where the voltage applied to the lower plate falls from its initial maximum value to a final lower value while the upper plate is held at ground potential, i.e. the ion beam is swept from top to bottom. However, due to axial symmetry either sweep direction can be effectively modeled merely by inputting the t_r or the t_f time value for the constant TAU), 7) *V0*, the initial maximum plate voltage, 8) *VTAU*, the final minimum plate voltage, and 9) *N*, the number of Boltzmann velocity bins and also 1/10 the number of time slices taken of the beamlet admitted through the slit.

An additional six parameters are supplied through answering prompts: 1) *M*, the mass-to-charge ratio, 2) *KE*, the beam kinetic energy, 3) *TEMP*, the beam temperature, 4) *R*, the beam radius, 5) *DX*, the number of trajectory loci to be calculated between the parallel plates, and finally 6) *DT*, the maximum acceptable flight time error for the two limiting trajectories which define an isomass packet. Thus, a total of fifteen adjustable parameters allow for tremendous flexibility.

Once these input values are assigned, the procedure BOLTZMANN is called. It generates an $N \times 2$ array, *VXDIST*, which contains the discreet velocity distribution for the ion beam (the tails are truncated at 5%); the velocity distribution data are also written to the file "BOLTZMAN.TXT."

The main program segment calculates successive ion trajectories through the beam deflection apparatus in a step-wise fashion. Each trajectory begins at time zero, at a predefined position, *X0*. The ion position is tracked by the main program segment through a series of appropriate procedure calls. PREACCEL handles the ion motion prior to entering the parallel plate region, CONSTACCEL addresses ion motion between the plates before the electric field changes, or after the field change has occurred (i.e. when

the electric field is constant), VARIACCEL addresses ion motion while the electric field is changing, and POSTACCEL tracks the ion position once the ion emerges from the parallel plates and terminates when the ion strikes the slit plate or (if the ion passes through the slit) the detector. Which procedures are called, and when, is determined by the main program segment logic. By design, the first calculated trajectory will impact the slit plate, the *X0* value is then increased by an amount proportional to *DT*, and the process is repeated until the first solution trajectory is found which passes through the slit.

Since the beam is swept downward, the fastest ions at the top, rearward portion of the beam which pass through the slit last establish the maximum initial distance from the parallel plates, *LASTX*, while the slowest ions at the top rearward portion of the beam establish the maximum flight time to the detector, *LASTT*. The fastest ions at the bottom, forward portion of the beam which pass through the slit first, establish the minimum flight time to the detector, *FIRSTT*. After comparing the initial *x*-coordinate of the slowest ions at the bottom, forward portion of the beam first to pass through the slit with the starting position of the fastest ions in the same region of the beam, the minimum initial distance from the parallel plates, *FIRSTX*, is also assigned.

Thus, limiting ion trajectories are used to define the initial spatial extent, and the final temporal width of the solution ion packet. The two flight times, *FIRSTT* and *LASTT*, bracket the arrival times of all other solution trajectories. This base width time interval is divided into *N* equal time segments which define the channels in the array *MCADIST* where subsequent trajectory flight times and intensities will be accumulated to create the final pulse shape histogram. Further, the initial *x* starting positions, *LASTX* and *FIRSTX*, bracket the starting positions (*X0*'s) for all the remaining trajectory calculations. The line segment defined by *LASTX* − *FIRSTX* is divided into 10*N* equal segments of width *DELTAX* whose midpoints will now serve, in turn, as the final set of *X0*'s. Additionally, complete trajectory data for the *FIRSTX* and *LASTX* trajectories are written to the file "TRAJECT.TXT."

A nested pair of FOR loops now takes control of the remaining trajectory calculations; the first loop steps through the final set of initial starting positions, *X0*'s, and the nested loop assigns the *x*-velocity, *VX*; the nested FOR loop steps through the entire Boltzmann velocity distribution, *VXDIST*, for each *X0*. Thus a total of $10N^2$ trajectories are computed. The main program segment handles these computations through a series of appropriate procedure calls as before, only now an additional procedure is called for each solution trajectory to calculate the cross-sectional area of the beam which passes through the slit. The area calculated by the procedure CHOPPER is then multiplied by *DELTAX* and the appropriate Boltzmann density to yield a relative intensity scalar. The flight time to the detector and the intensity scalar are then used to build a pulse shape histogram. The final accumulated data contained in *MCADIST* are written to the file "PULSE.TXT." A diagram illustrating the basic histograming process is shown in Figure 3-7.

Experimental

Before any meaningful cluster ion research could be accomplished, the performance characteristics of the new cluster ion source and beam deflection TOF mass spectrometer had to be determined. A dual approach was utilized to combine both experiment and theory in order to gain the maximum amount of information about the new system in the least amount of time. Of particular concern was the effect of the collinear beam deflection technique on the time, intensity, and resolution of the final mass peaks.

Computer simulations were run for a 550 eV monoenergetic ion beam over the mass range of 1 to 10^6 amu. Two series of calculations were performed for a 3 mm slit using different deflection voltage rise times: t_r = 2200 ns and t_r = 30 ns. All the code parameters were matched as close as possible to the actual experimental setup. The beam axis (or centerline) trajectories between the parallel plates for each run were plotted and

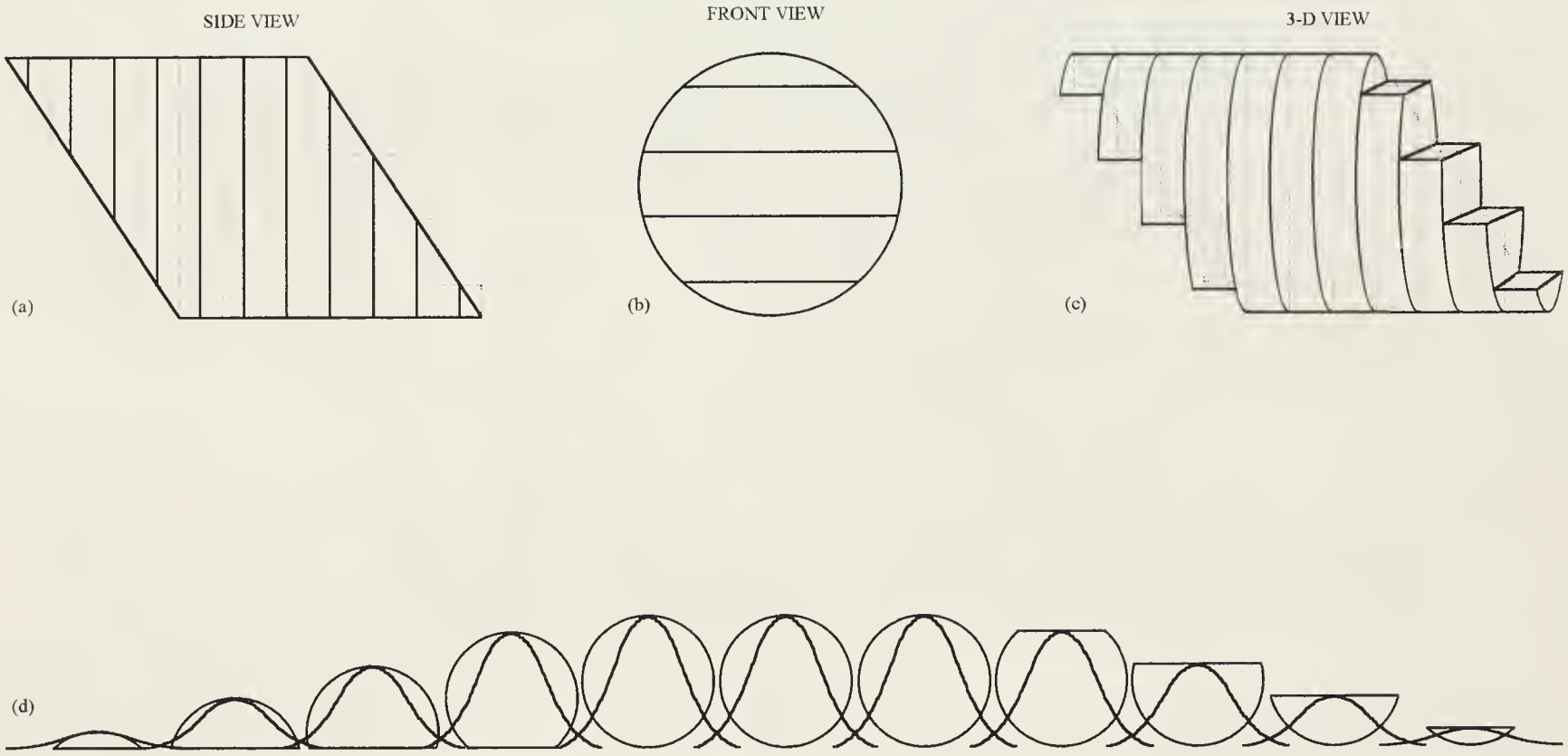

Figure 3-7 Beam sampling algorithm illustration. (a) The vertical solid lines indicate time slices through the solution beamlet as it traverses the slit plane. The planar cross-sections are then used to generate the solid volumes indicated by the dotted lines; (b) Front view of solution beamlet with time slices indicated by the horizontal solid lines; (c) A three dimensional representation of the solid volumes generated by TRAJION to approximate the true beamlet volume; (d) Scaling diagram illustrating the combined intensity effects of procedures CHOPPER and BOLTZMANN to create the final composite isomass pulse shape histogram.

are shown in Figures C-1 through C-14 of Appendix C. The complete trajectory data are displayed along with the trajectory plots in accompanying tables.

Preliminary experiments were also run to test the effect of various experimental configurations on the overall equipment performance. Once the optimum operating parameters were established (i.e. pulse valve settings, Einzel lens and steering plate voltages, etc.) a series of experiments was conducted to elucidate the effects of slit size and deflection voltage rise time on the signal intensity and resolution. Fifteen different configurations were tested using five slit geometries (none, 3 mm, 2 mm, 1 mm and 0.5 mm) and three different deflection voltage rise times (2200 ns, 500 ns and 30 ns). Carbon dioxide at a stagnation temperature of about 100°F and 2 to 15 psig pressure was used throughout. The pulse valve was selected to fire at between 2 to 8 Hz with 200 μs duration. The 0.030 inch i.d. nozzle was positioned 4.7 cm away from the skimmer. The electron gun and collector were positioned $\sim$5.8 mm away radially and produced a continuous stream of 120 eV electrons through the 1 mm slit opening in the gun face which was axially positioned flush with the nozzle tip. The nozzle voltage was maintained at +550 V while the skimmer was held 5 V below it at +545 V. Both Einzel lenses were kept at +340 V. Steering plate voltages were adjusted at the beginning of each day's run to maximize the signal intensity of the undeflected CO_2 pulsed beam. The final spectra were accumulated from 500 to 2,000 shots, depending on the signal-to-noise (S/N) ratio produced by the given configuration being tested. Typical source pressures were 2×10^{-6} torr base, to 2×10^{-5} torr with the valve firing. Pressures in the ion optics and beam deflection region were generally $\sim5\times10^{-7}$ torr while the pressure in the detector region was 1×10^{-6} torr.

A final set of TRAJION simulations were also performed. Trajectory calculations for a CO_2^+ beam with a mean energy of 550 eV were computed for each of the five slit configurations using all three deflection voltage rise times. The internal beam translational temperature (Boltzmann energy spread) was set at 10 K and the beam diameter was

defined as 1 mm. The resulting fifteen 101-channel, pulse shape histograms are presented as Figures C-15 through C-17 in Appendix C.

Results and Discussion

The reduced data for the monoenergetic beam centerline trajectory study are presented in Tables 3-2 and 3-3 as the length of the segment chopped out, or sampled, from the beam by the beam deflection technique. Since the beam is assumed to be homogeneous, the sampled beamlet length for a given ion mass is directly proportional to the final pulse intensity. As shown in Figures 3-8 and 3-9, the initial TRAJION calculations predict a mass dependent intensity function for ions up to about 10^3 amu when the beam is swept slowly (t_r = 2200 ns) across the 3 mm slit; however, an enhanced sensitivity for lower mass ions is not indicated when the beam is swept quickly (t_r = 30 ns). Thus, if a slow deflection voltage rise time and large slit are utilized, intensity corrections would have to be made before quantitative comparisons based on peak intensities could be made.

Fortunately, the peak positions (flight times) remain proportional to the square root of the ion mass as in standard TOF methods. Graphical proof of this statement is given for both the slow and fast beam sweep cases in Figures 3-10 and 3-11. The sampled beamlet midpoint positions for the seven representative ion masses (see Tables 3-4 and 3-5) were plotted against time to ascertain whether a common starting position, and thus a constant flight path length, existed. For both cases, all the beamlet midpoints were precisely aligned at the same time at a point approximately 12.43 mm into the parallel plates--just short of halfway. Thus, even for a collinear beam deflection TOF system in which the slit and detector have not been offset to compensate for the off-axis beam displacement generated by the electric field between the parallel plates, each isomass ion

Table 3-2 Temporal and Spatial Beamlet Lengths
(tr = 2200 ns, KE = 550 eV, 3 mm slit)

m/e	w (ns)	w (mm)
1	120.999	39.419127
10	120.999	12.465423
100	120.999	3.941913
1000	135.515	1.396077
10000	428.417	1.395784
100000	1355.103	1.395756
1000000	4281.448	1.395752

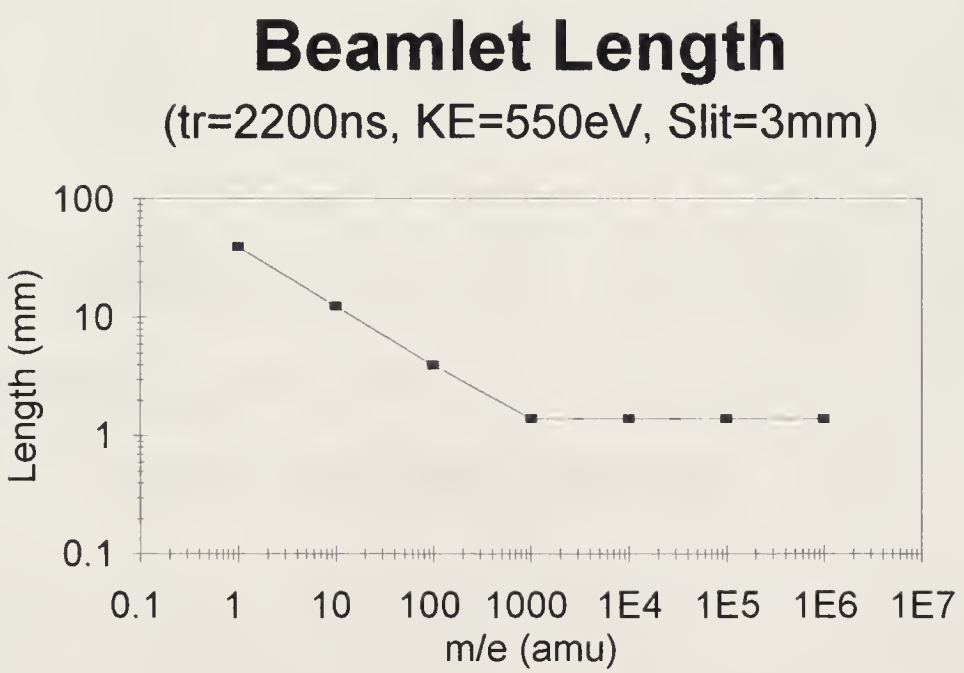

Figure 3-8 Plot of beamlet length as a function of ion m/e.

Table 3-3 Temporal and Spatial Beamlet Lengths
(tr = 30 ns, KE = 550 eV, 3 mm slit)

m/e	w (ns)	w (mm)
1	4.283	1.395318
10	13.547	1.395623
100	42.842	1.39571
1000	135.482	1.395748
10000	428.433	1.395752
100000	1354.825	1.395753
1000000	4284.33	1.395751

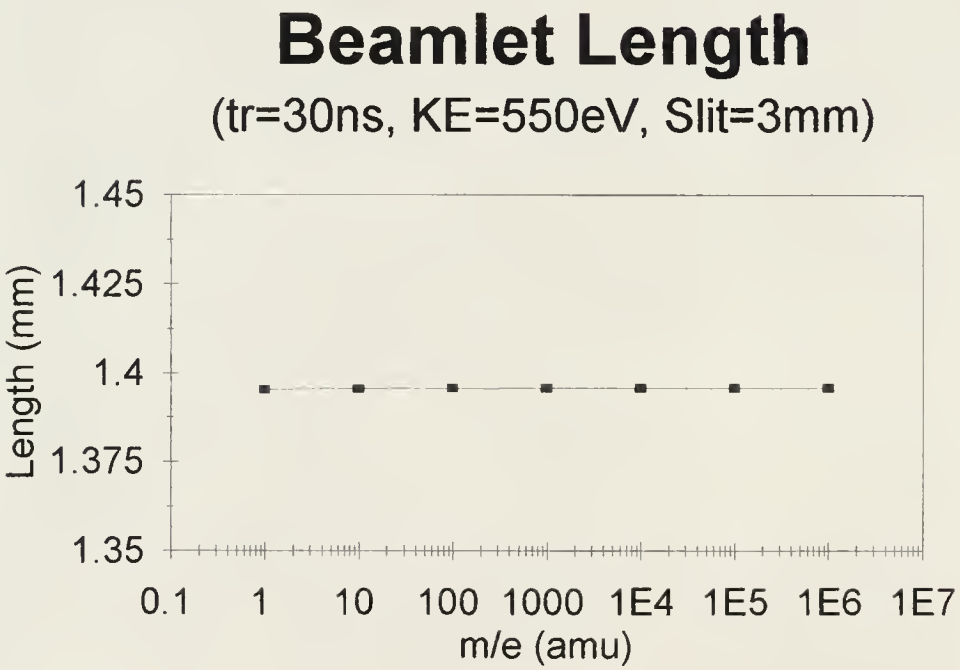

Figure 3-9 Plot of beamlet length as a function of ion m/e.

Table 3-4 Beamlet Position Data
(tr = 2200 ns, KE = 550 eV, 3 mm slit)

m/e	x (mm)	t (us)
1	-345.83778	0
	25.4	1.1395335
10	-100.80216	0
	25.4	1.2250155
100	-23.315092	0
	25.4	1.4953345
1000	1.1711105	0
	25.4	2.351843
10000	8.855657	0
	25.4	5.0783695
100000	11.299598	0
	25.4	13.686937
1000000	12.073828	0
	25.4	40.905356

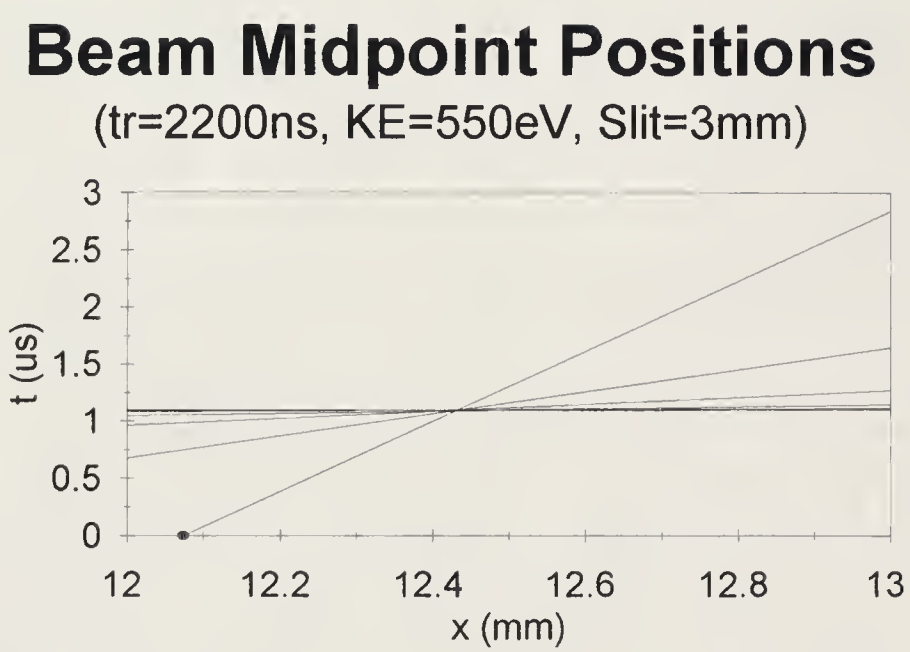

Figure 3-10 Plot of isomass beamlet midpoint positions vs time. Parallel plate midpoint position is at 12.7 mm.

Table 3-5 Beamlet Position Data
(tr = 30 ns, KE = 550 eV, 3 mm slit)

m/e	x (mm)	t (us)
1	7.558599	0
	25.4	0.0547655
10	10.888122	0
	25.4	0.1408635
100	11.943573	0
	25.4	0.413052
1000	12.277595	0
	25.4	1.273762
10000	12.383248	0
	25.4	3.9955575
100000	12.416662	0
	25.4	12.60263
1000000	12.427229	0
	25.4	39.820576

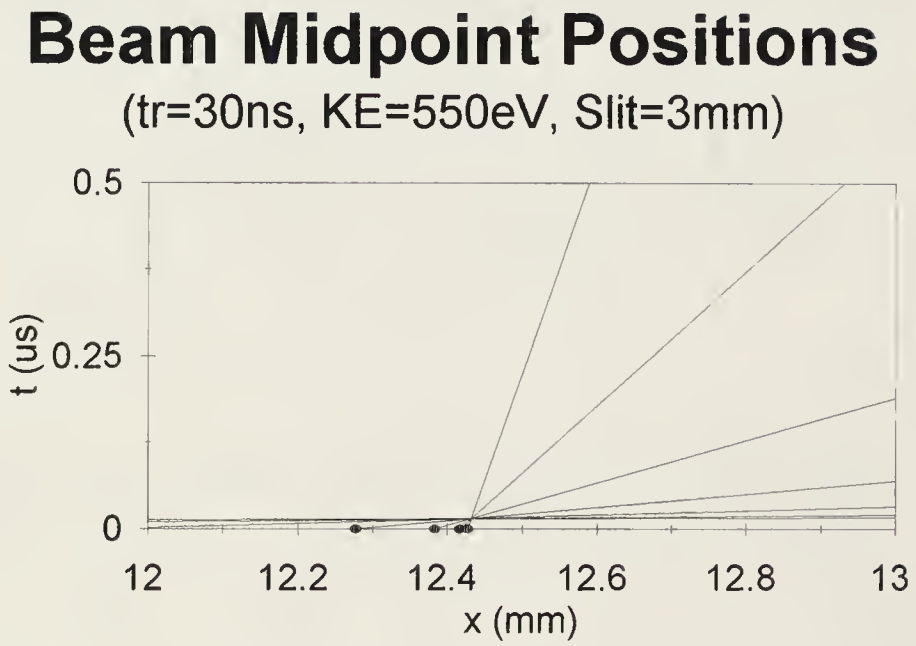

Figure 3-11 Plot of isomass beamlet midpoint positions vs time. Parallel plate midpoint position is at 12.7 mm.

packet traverses a constant path length ensuring standard TOF methods still apply for peak identification.

The results of the experiments conducted to characterize the equipment performance under various slit and deflection voltage rise time configurations are summarized graphically in Figure 3-12. The CO_2^+ peak resolution, as measured by the full-width at half the maximum intensity (FWHM), shows a marked improvement for all five slit configurations when the deflection voltage rise time is decreased from 2200 ns to 500 ns, but changes very little when the rise time is further decreased to 30 ns. This same general trend was predicted by the TRAJION simulations for a 1 mm diameter CO_2^+ beam with a Boltzmann translational energy spread of 10 K (see Figure 3-13).

The effect of slit size on peak resolution is not as clear. The relative positions of the five resolution curves in Figure 3-12 seem almost random; in fact, their relative positions probably have very little meaning at all. Because of the complexity of the ion source and mass spectrometer systems, it is very difficult to reproduce exactly the same operating conditions from one day to the next since the equipment had to be completely shut down at the end of each day to preclude possible damage from loss of utilities in the laboratory. Perhaps the largest source of error resulted from the visual alignment of the nozzle, ion optics, and slit, which had to be accomplished after each slit configuration change. As the TRAJION calculations bear out, even slight misalignments can cause portions of the chopped beamlet to miss the detector, or impact the sides of the flight tube wall. In fact, the TRAJION results indicated that significant wall collisions may occur for slits larger than 2 mm. In addition, it was later discovered, after these series of experiments were completed, that Teflon insulating discs located at the beginning of the TOF mass spectrometer were acquiring a static charge from ion impact and were thus making it extremely difficult at times to focus and steer the beam onto the detector at the end of the mass spectrometer. The problem has since been corrected.

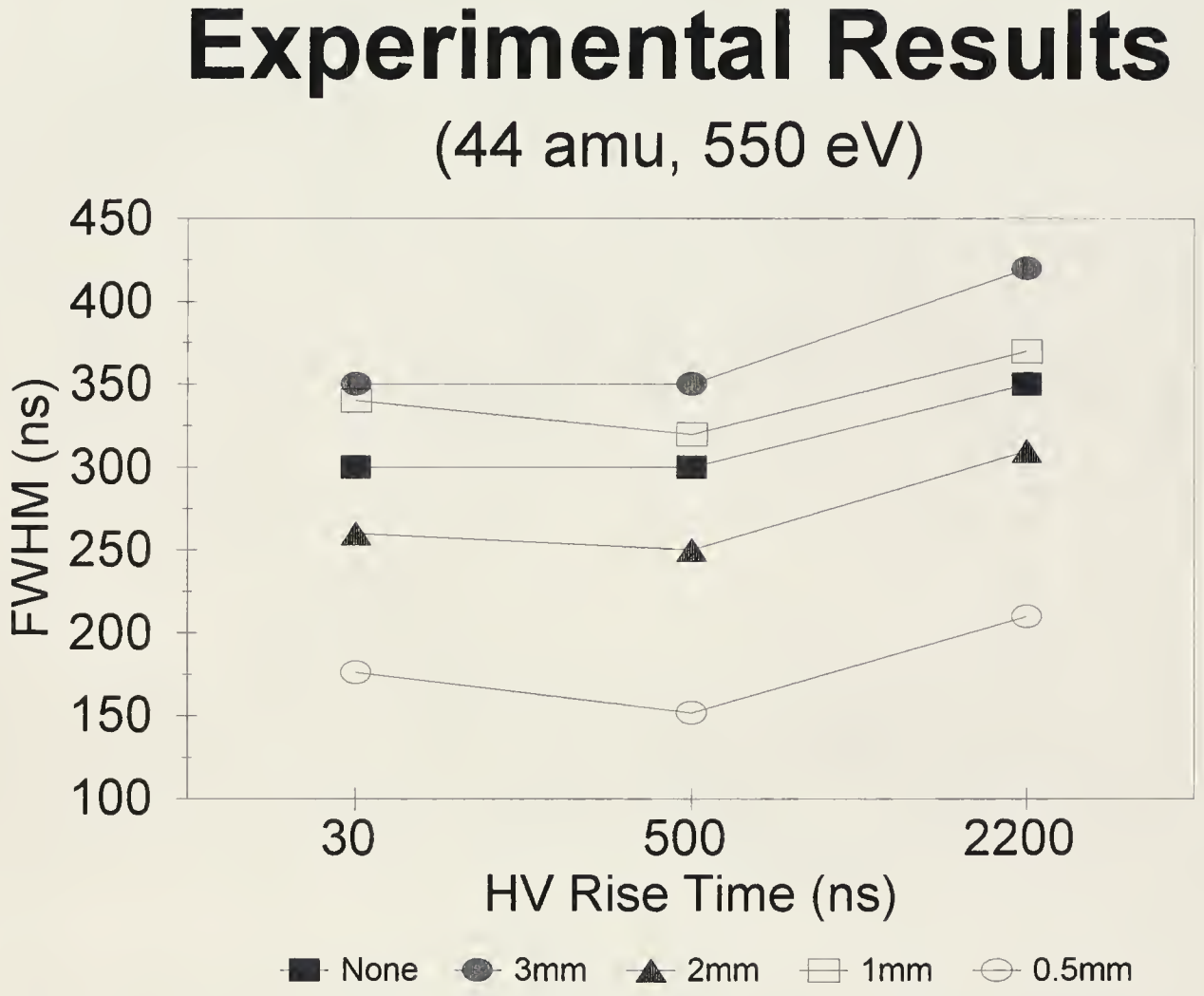

Figure 3-12 Effect of HV rise time on pulse FWHM for 5 slit configurations (none, 3 mm, 2 mm, 1 mm and 0.5 mm).

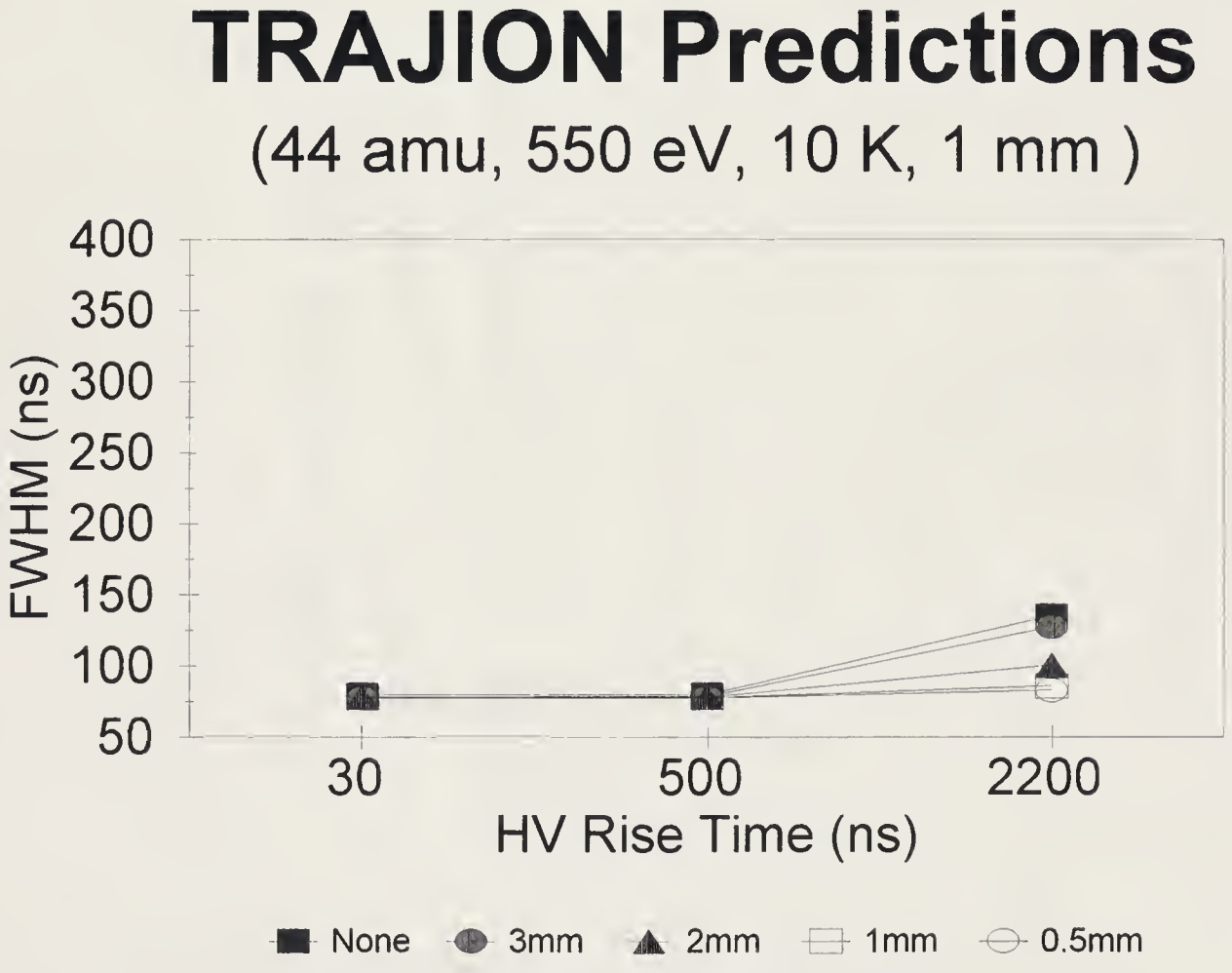

Figure 3-13 Effect of HV rise time on pulse FWHM for 5 slit configurations (none, 3 mm, 2 mm, 1 mm and 0.5 mm).

The TRAJION results were based on an estimated 1 mm beam diameter and 10 K energy spread in the beam translational motion. The beam spot could not be measured experimentally with available equipment, but the SIMION ion optics model predicted a converging beam whose focal point was positioned just in front of the parallel plates when both Einzel lenses are held at +340 V (cf. Fig. 2-5). The SIMION model then suggests an initial beam diameter of nearly zero which then diverges to just under 1 mm as the beam exits the parallel plate region. Likewise, the beam kinetic energy spread was not directly measured, but a plausible value was chosen. Thus, the values selected for input into the computer code were likely not exact matches to the true experimental values, and this, along with the aforementioned variability introduced into the experimental effort, accounts for the modest differences between Figure 3-12 and Figure 3-13. Peak intensity attenuation when going to smaller slits and faster beam deflection rise times was born out in both the experimental effort and the TRAJION simulations.

Thus, both experiment and theory agree that by varying the deflection voltage rise time the sensitivity/resolution trade-off can be changed. This allows for the resolution and sensitivity to be tailored to meet the needs of each particular experiment.

The physical picture of beam deflection when the beam is not monoenergetic is actually quite complex to visualize. The differing energies means that even ions of like mass will experience differing displacements in the electric field between the parallel plates; thus, one can think of the ion beam as a series of coaxial beams of differing energies (and velocities) which are swept back and forth across the slit by varying amounts, thus resulting in an overall elongation of the beam spot at the two sweep position extremes. This effect is illustrated in Figure 3-14. Thus, just as expected, if the energy spread is too great, TOF mass spectrometry cannot be successfully employed. Fortunately, one of the hallmarks of using supersonic expansions is that they generate exceedingly cold ion beams with closely matched velocities near the center of the expansion where the beam is sampled by the skimmer.

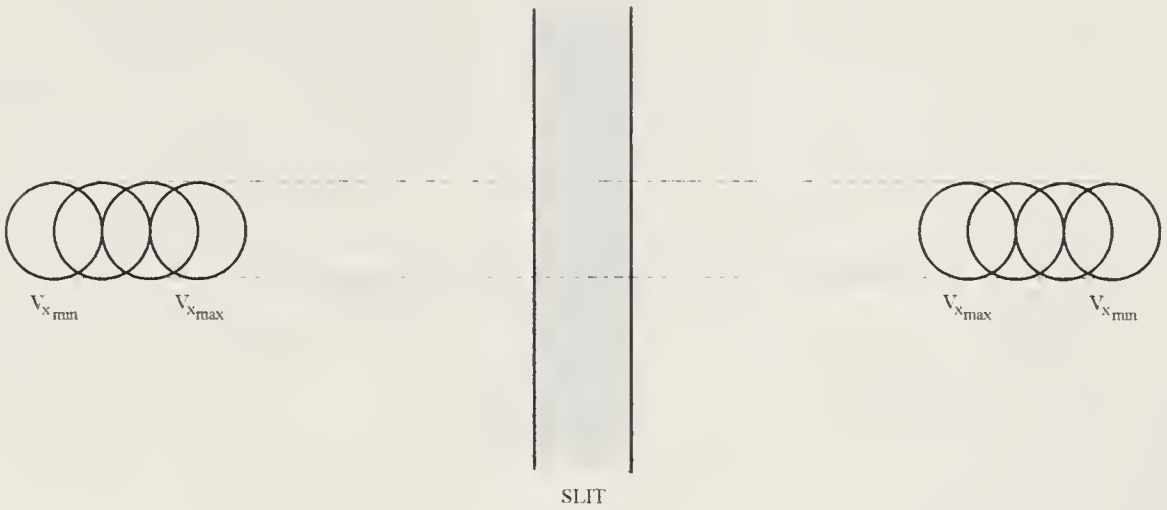

Figure 3-14 Beam spot diagram for an isomass beam with varying translational energies and therefore velocities varying between Vx_{min} and Vx_{max}. The maximum beam displacement (at the slit plane) for the two highest static field conditions is shown.

The TRAJION code is a good design tool which certainly aids the user tremendously in developing a better understanding, if not intuition, of the behavior of this rather complex system. By no means has a completely comprehensive understanding of the beam deflection technique in TOF mass spectrometry been reached, nevertheless a sufficient working knowledge of the effects of changing various parameters was obtained to allow the research to progress to the next stage--the formation and characterization of cluster ions.

CHAPTER 4
SURVEY OF INITIAL CLUSTER ION RESULTS

Introduction

Having gained a basic understanding of the general behavior of the experimental apparatus itself, the next step was to complete the characterization of the new pulsed source and beam deflection TOF mass spectrometer by actually forming cluster ions and comparing the results to available scientific literature.

The cluster ions were generated using three separate gases: He, N_2 and CO_2. The cluster ions were produced through EI ionization of the gas as it exits the nozzle. Since this process is rather inefficient, many neutral species remain to aggregate around these seed ions resulting in cluster ion growth. Thus, these rapid three-body ion-molecule association reactions which occur very early in the supersonic expansion should be quite sensitive to the initial gas density or pressure.

Saenger and Fenn [48] predicted a minimum pulse duration (valve open time) of about 10 μs for a pulsed supersonic free jet to reach a fully developed flow comparably cold to that obtained from a continuous source. Because of the novel in-line switching technique used to sample the beam pulse "on the fly" for TOF mass analysis, a unique opportunity existed to actually examine the composition of a pulsed beam by generating a temporal cross-sectional profile of the beam pulse.

Thus, the effect of the source stagnation pressure on the observed clustering was investigated, and the effect of where the sample is taken (or chopped) from each beam pulse was also studied.

Experimental

Each experiment was conducted under essentially the same equipment configuration. The gas stagnation conditions were typically 105°F at variable pressures of 2 to 45 psig. The pulse valve was set for 200 μs pulses and fired at 3 or 8 Hz. The nozzle (0.030 inch i.d.) was held at +550 V, the skimmer (2 mm i.d.) voltage was +545V and each Einzel lens was maintained at +340 V. The electron gun and collector were positioned 5.8 mm away radially and produced a continuous stream of ~120 eV electrons through the 1 mm gun slit opening which was axially positioned flush with the nozzle tip. A 3 mm slit was used in obtaining the He cluster ion spectrum and the beam pulse profile spectra; the rest of the data were collected with no slit installed. A beam deflection voltage rise time of 30 ns was used throughout. Expansion chamber pressures varied widely with the stagnation conditions but were generally $\leq 5\times10^{-5}$ torr when the valve was firing. Post skimmer pressures in the ion optics and beam deflection regions were routinely in the mid 10^{-7} torr range while the pressure near the detector was 1×10^{-6} torr.

Each gas was supplied from pressure regulated K-bottles and was introduced into the pulse valve inlet via 1/4 inch tubing. The He and CO_2 experiments were run without a filter to remove particulate material and water vapor; the N_2 work was done later, with the benefit of a new gas manifold system and in-line filter (a Sporlan "Catch-all" filter drier containing 5 in^3 of desiccant).

Pressure effects on CO_2 clustering were investigated at four different pressures: 2 psig, 15 psig, 30 psig and 45 psig. Each spectrum was accumulated from 500 single-shot spectra.

Pulse profile data were obtained using CO_2 as well. The delay from the SRS Digital Delay/Pulse Generator into the Fast High Voltage Pulser (cf. Figure 3-2) was varied from 500 μs to 1,000 μs while collecting data from a stable CO_2 pulsed beam. Since the SRS unit is triggered by the TTL signal from the Iota One Pulse Driver,

changing the delay of the SRS output TTL signal into the Fast High Voltage Pulser provides a simple, yet very precise method of selecting where the TOF beamlet sample will be chopped out of the gross beam pulse. These data were collected in a series of accumulated spectra of 500 shots each.

Great care was taken not to introduce systematic errors while conducting the CO_2 stagnation pressure and pulse profile studies. Each of these series was completed in a single day to eliminate changes in the equipment parameters which accompany each fresh start-up. Additionally, adjustments to the equipment while running were kept to a minimum to ensure that the observed effects could be attributed to the variable under study (i.e. stagnation pressure, deflection voltage delay).

Results and Discussion

The He spectrum is shown in Figure 4-1. Three He containing ion peaks are clearly evident: He^+, HeH^+ and He_2^+. This spectrum (an accumulation of 500 single-shot spectra) was obtained with a He stagnation pressure of 15 psig and did contain a small air contaminant as evidenced by the characteristic nitrogen, oxygen and water peaks.

The N_2 spectrum presented in Figure 4-2 shows clear evidence of nitrogen clustering. N^+, N_2^+, $N(N_2)^+$, $(N_2)_2^+$, $(N_2)_3^+$, $(N_2)_4^+$, $(N_2)_5^+$ and $(N_2)_6^+$ ion peaks each appear well above background. This spectrum was obtained with an N_2 stagnation pressure of 15 psig as well, and represents the accumulation of 1,000 single-shot spectra. Small H_2O^+ and O_2^+ peaks are also seen.

Figure 4-3 displays the results of expanding CO_2 with a stagnation pressure of 45 psig. A rich array of cluster ions resulted. The primary series observed was $(CO_2)_n^+$ where n = 1 to 7; however, mixed clusters resulting from further additions of H_2O and O_2 were also detected. Thus, $(CO_2)_n(H_2O)_m^+$ where m = 1 or 2, and $(CO_2)_nO_2^+$ were formed, and are due to impurities in the gas handling system.

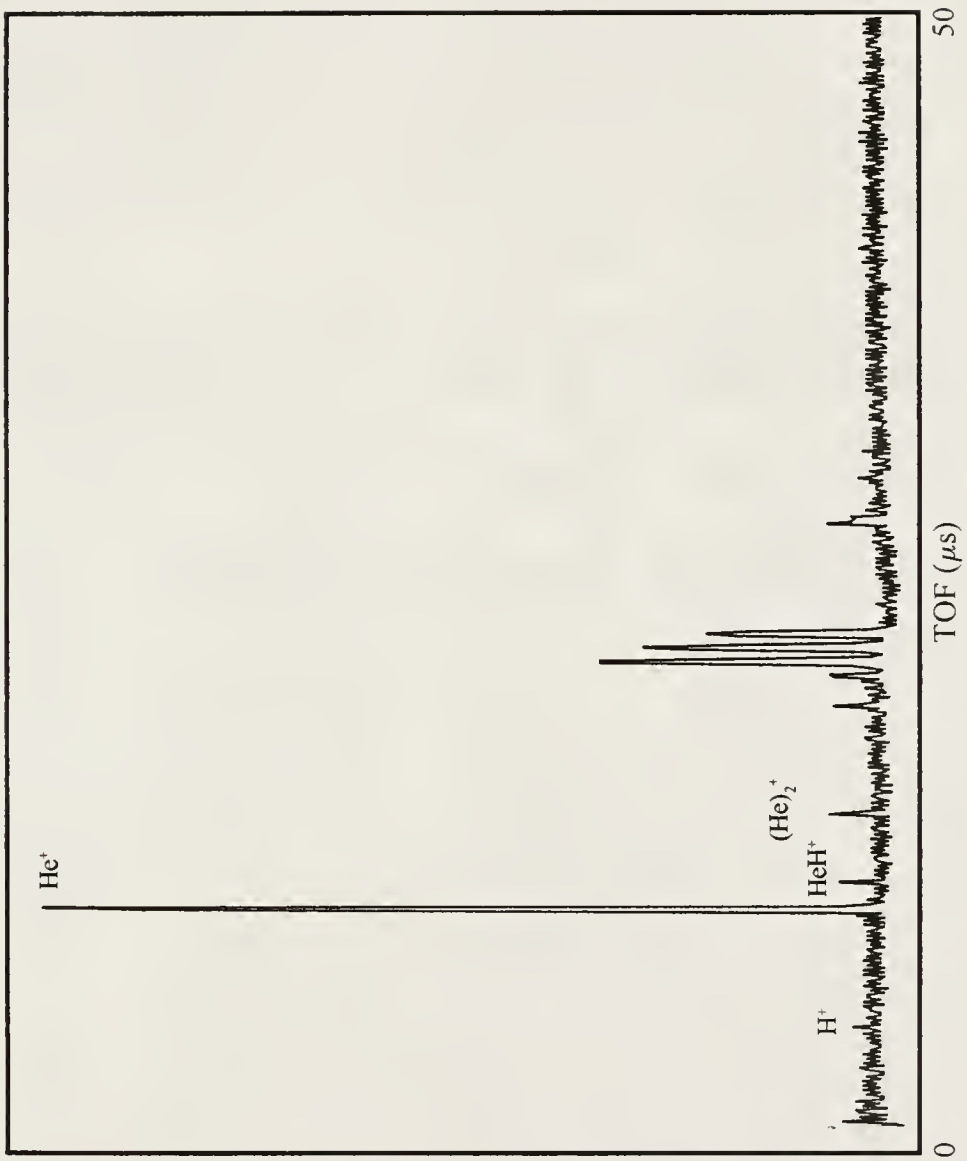

Figure 4-1 TOF mass spectrum of He expansion.

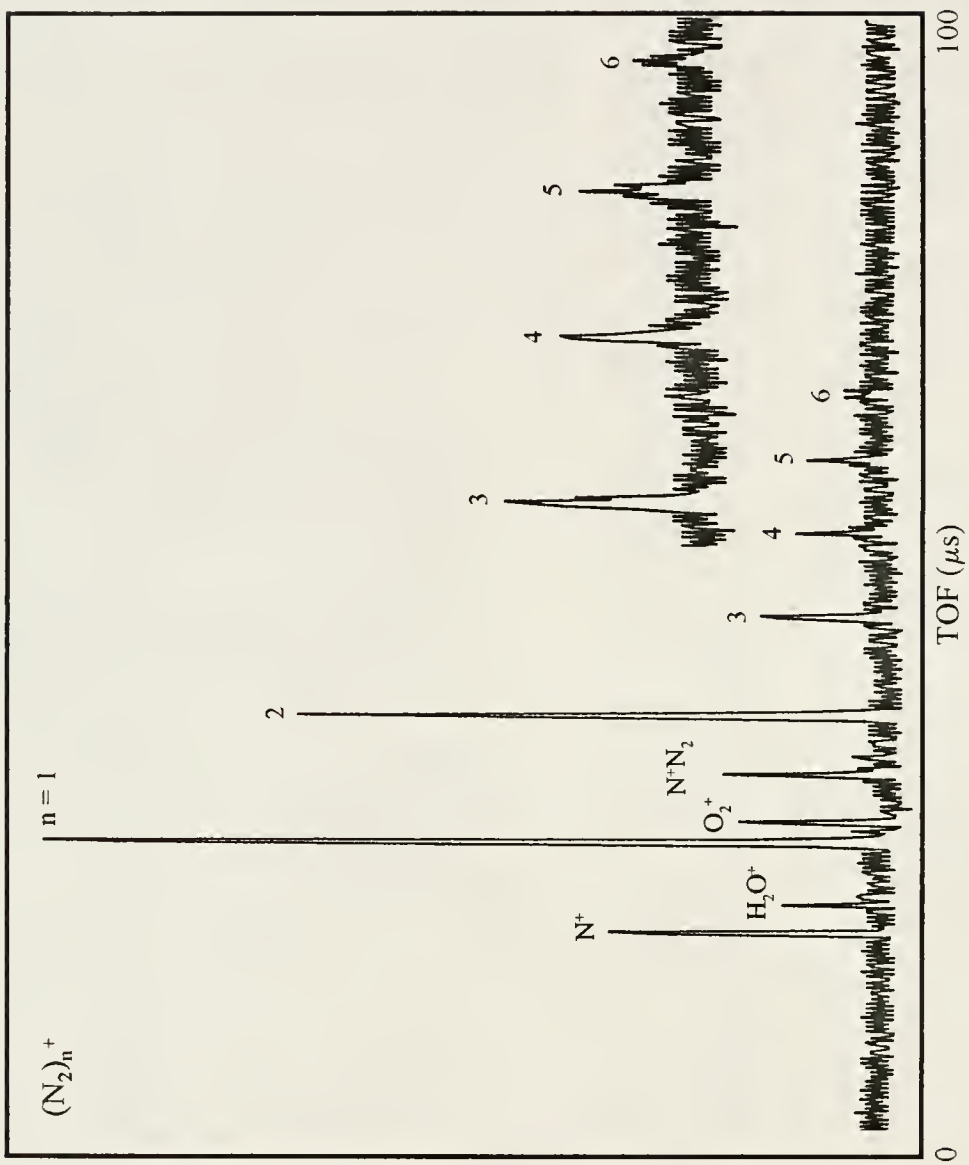

Figure 4-2 TOF mass spectrum of N_2 expansion.

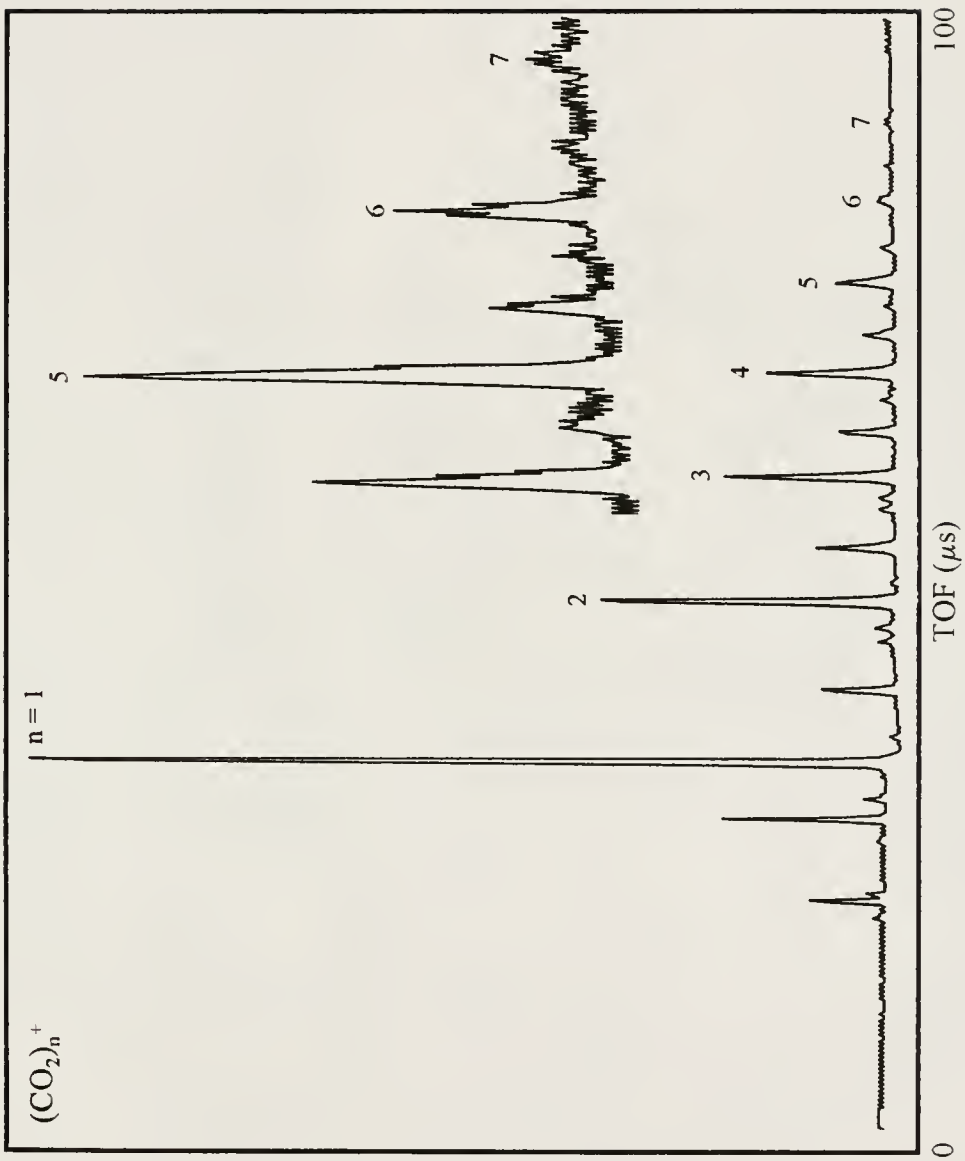

Figure 4-3 TOF mass spectrum of CO_2 expansion.

The results of these three cluster ion experiments demonstrated that the ion source and beam deflection TOF mass spectrometer were indeed fully operational. The initial design and construction of the ion source and ion optics was patterned after the high intensity ion source developed by Young Bae et al. at SRI International.[31] Though some significant equipment differences exist, our results compare quite favorably to those reported by Young Bae's group for $(He)_n^+$, $(N_2)_n^+$ and $(CO_2)_n^+$ cluster ion genesis. However, slightly smaller clusters were observed in our apparatus ($n \leq 7$) as compared to theirs ($n \leq \sim 10$)

Johnson et al.[29] reported the synthesis of CO_2 cluster ions by successive nucleation onto a monomer ion during a free jet expansion as a function of the distance between the electron beam (200 eV energy, 100 μA, 1 mm diameter) and the nozzle (1.0 mm diameter, 1.5 atm. CO_2 stagnation pressure at room temperature). As per Figure 4-4, the results from a distance of 2.8 cm show only a single peak from the CO_2^+ monomer--thus, in the absence of subsequent collisions, the primary ion produced by electron impact is the monomer, with very little contribution to higher clusters from the ionization of neutral clusters formed in the jet. However, they found the degree of clustering increased dramatically as the electron beam was moved toward the nozzle. Higher clusters were successively formed until, at 0.2 cm distance, a distribution peaking at $n = 7$ and continuing through about 17 was obtained. At that distance (0.2 cm), the pulsed beam density was estimated to be about $10^{17}/cm^3$, sufficiently high that three-body clustering represents a significant loss mechanism for the nascent CO_2^+ species formed by electron impact.

Though the effect of varying the distance between the nozzle and electron gun in our system was not investigated, it seems quite probable that a similar proximity effect would exist for a well collimated e-beam. Because of the simple e-gun design utilized in this work (electrons are accelerated through a 1 mm wide slit without the benefit of any focusing lenses or steering plates, cf. Figure 2-3) the electron stream is probably not well

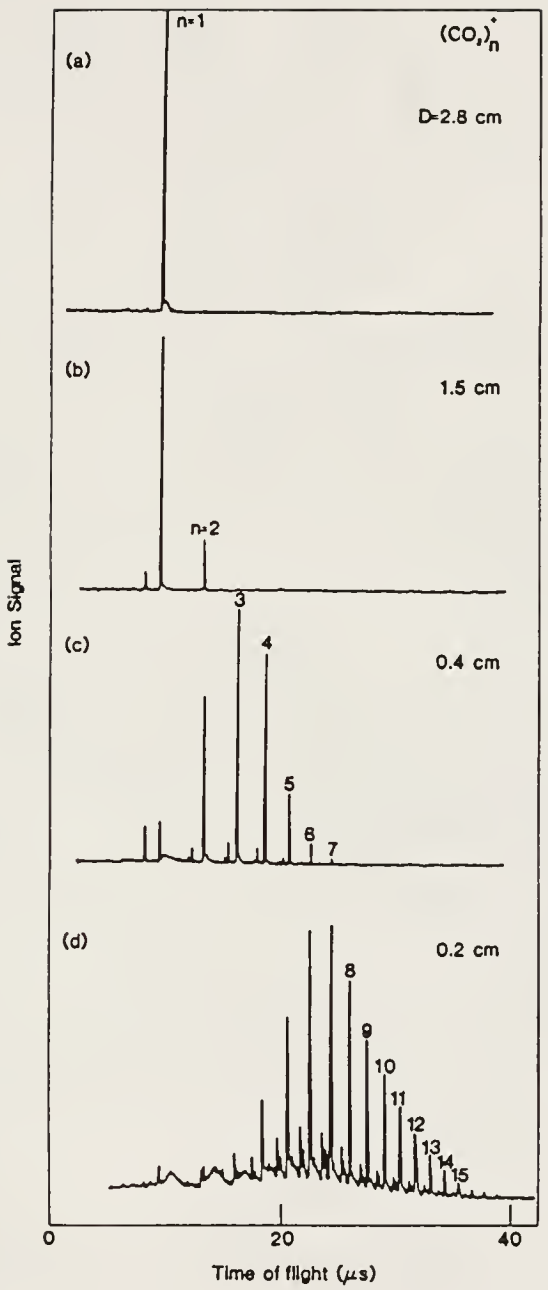

Figure 4-4 TOF mass spectra as the distance between the electron beam and the nozzle is varied. The clusters are the result of successive attachments of CO_2 to CO_2^+, not from the ionization of neutral CO_2 clusters. The sharp features between the main peaks correspond to $(CO_2)_n^+$ with added O_2 or H_2 and are due to impurities in the gas handling system; collision-induced dissociation of the higher clusters during the extraction from the high-density jet give rise to the broad peaks. (Taken from Johnson et al.[29])

collimated, but is more likely characterized as a spray; thus, any attempt to make fine adjustments to where the e-beam intersects the expanding jet were deemed unpromising, especially in light of the good clustering results already obtained.

The effect of the source stagnation pressure on the beam intensity and degree of clustering are shown in Figure 4-5 for CO_2 gas pressures of 2, 15, 30 and 45 psig. The primary $(CO_2)_n^+$ cluster ion series shows increased clustering with increased pressure as expected. At 2 psig $n \leq 4$, whereas at a CO_2 stagnation pressure of 45 psig the maximum cluster size, n, increased to 7. Thus, an effective means of increasing the associative collisions which result in cluster growth is to simply increase the backing pressure of the source gas.

The CO_2 temporal beam pulse profile data are presented in Figures 4-6 and 4-7. Beam time slices taken in increasing 100 μs increments, beginning at 500 μs delay from the pulse valve driver TTL signal and continuing up to a full 1 ms delay, are shown in Figure 4-6. As clearly seen from the spectra, the most dramatic change in beam intensity takes place during the first 100 μs of the beam pulse leading edge. Figure 4-7 contains the results of a much closer examination of the first 100 μs of the beam pulse leading edge. The beam slices taken in 10 μs time increments reveal a rather sharp increase in intensity which reaches a maximum at about 550 μs delay and then begins to slowly decrease. This behavior agrees quite well with the undeflected beam pulse shapes observed on the DSO while adjusting the valve travel, steering plate voltages, etc. when the beam deflection voltage was turned off (see Figure 4-8).

Still the question remains as to whether any portion of the pulsed beam is comparably cold to that produced by a continuous beam under the same source conditions--or in other words, how much time is required for the pulsed supersonic jet to reach fully developed flow? A simple model was developed by Saenger and Fenn[48] for estimating the minimum valve open time for a pulsed nozzle to produce a beam like that

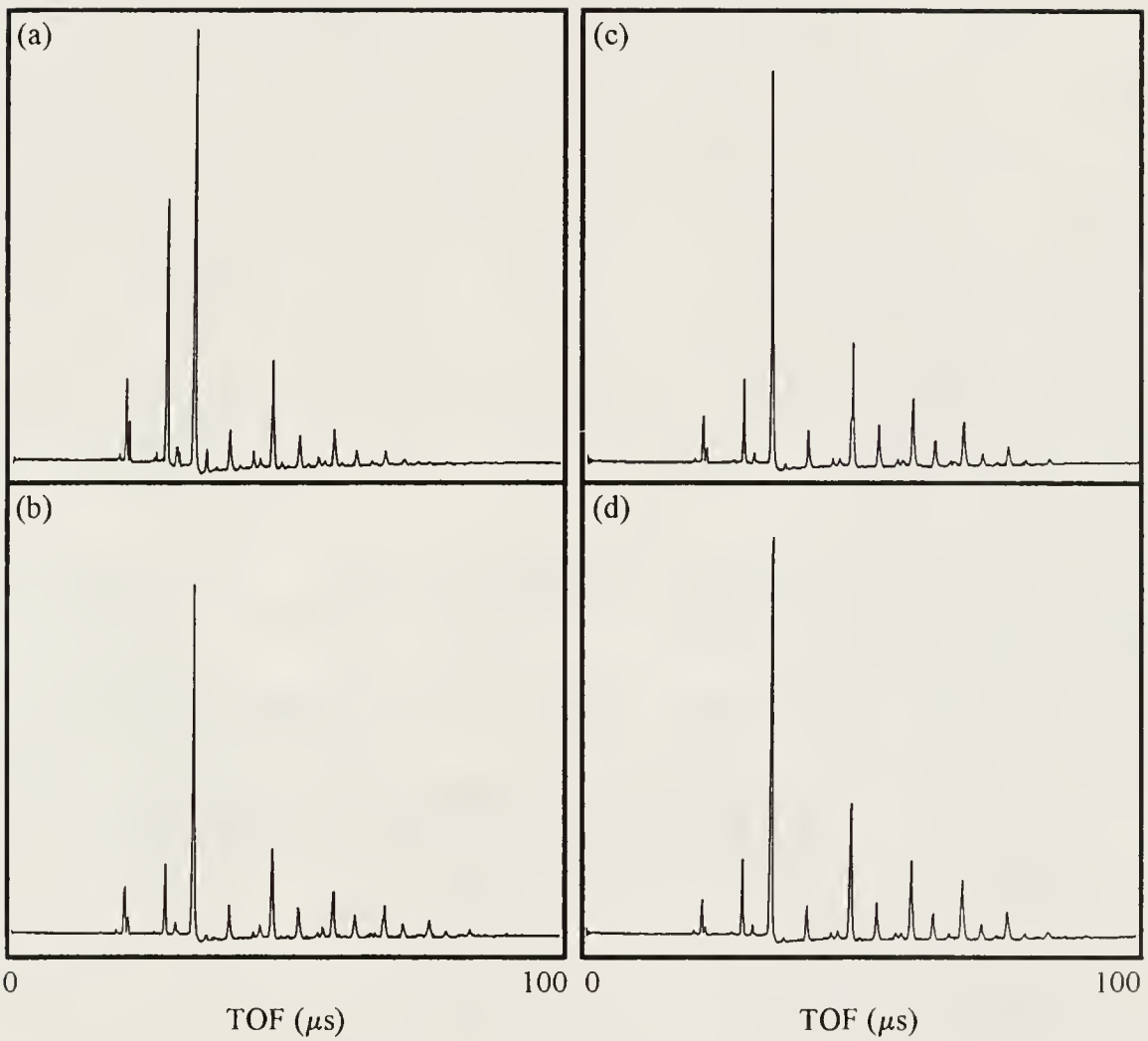

Figure 4-5 TOF mass spectra as a function of the CO_2 source stagnation pressure. Cluster results from (a) 2 psig, (b) 15 psig, (c) 30 psig, and (d) 45 psig backing pressures are shown. Each spectrum was accumulated from 500 single-shot spectra and is presented at the same scale.

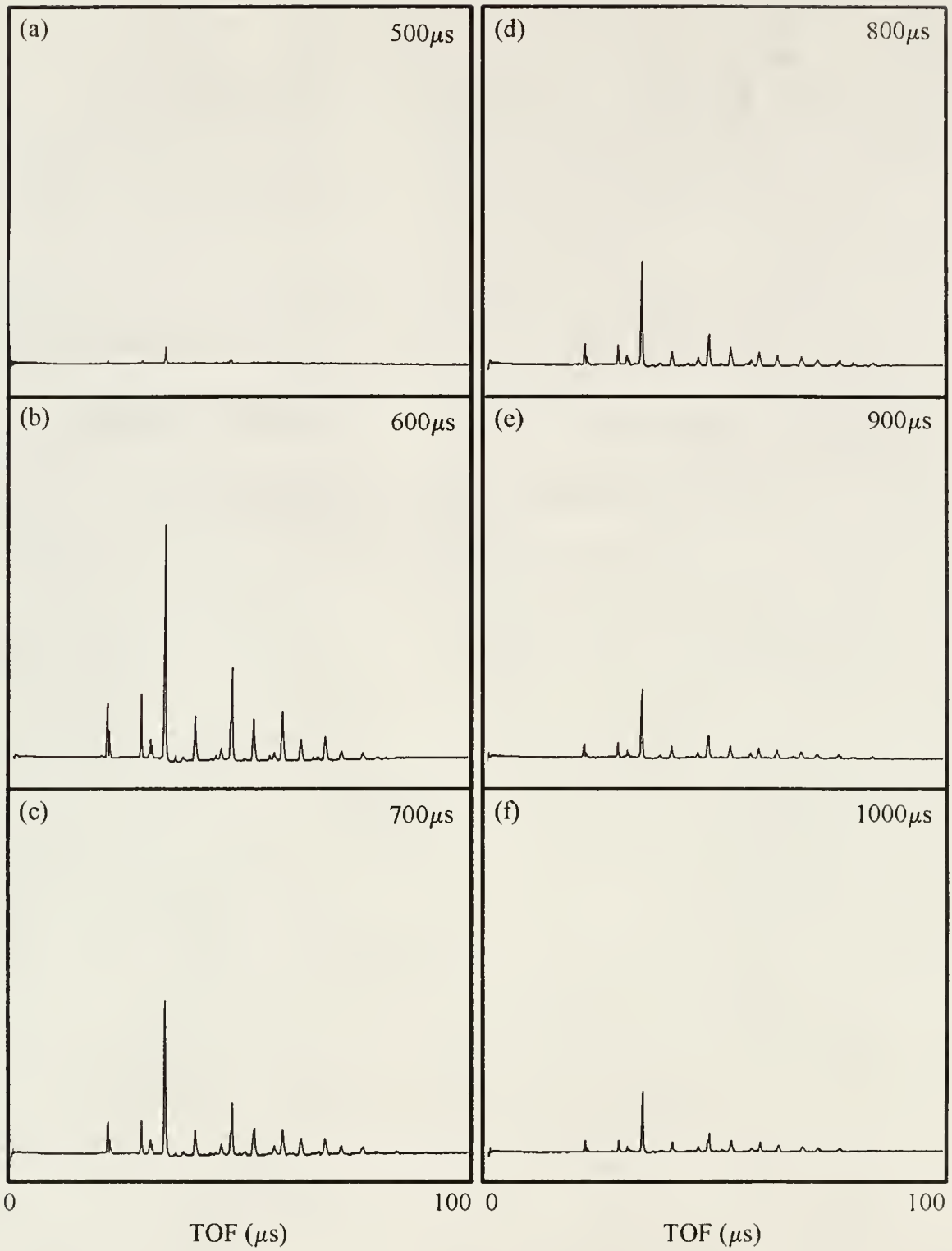

Figure 4-6 CO_2 pulse profile. TOF mass spectra taken at increasing intervals of 100 μs into the beam pulse. Each spectrum represents the accumulation of 500 single-shot spectra and is presented at the same scale.

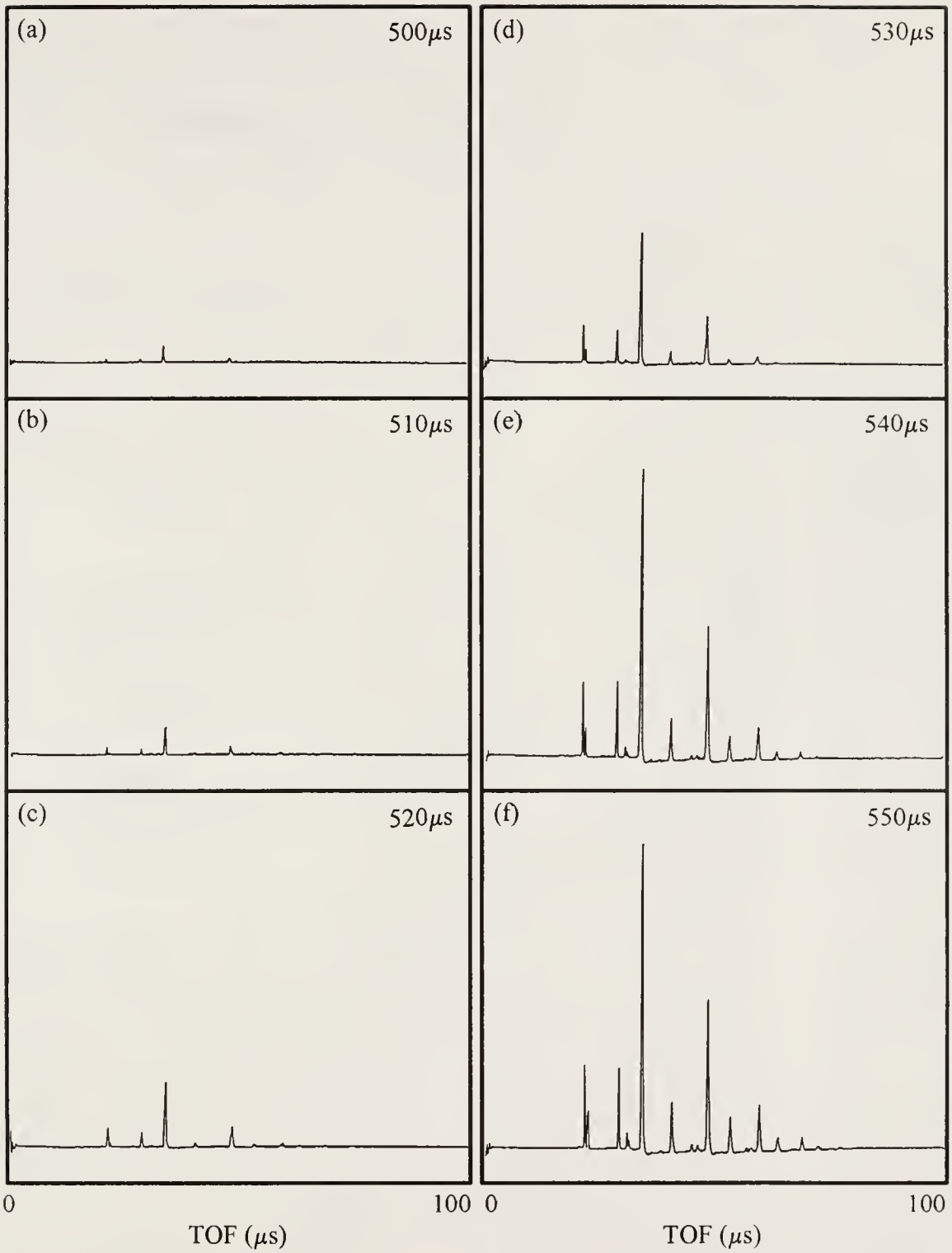

Figure 4-7 Profile of the CO_2 pulse leading edge. TOF mass spectra taken at increasing intervals of 10 μs into the leading edge of the beam pulse. Each spectrum represents the accumulation of 500 single-shot spectra and is presented at the same scale. (continued on next page)

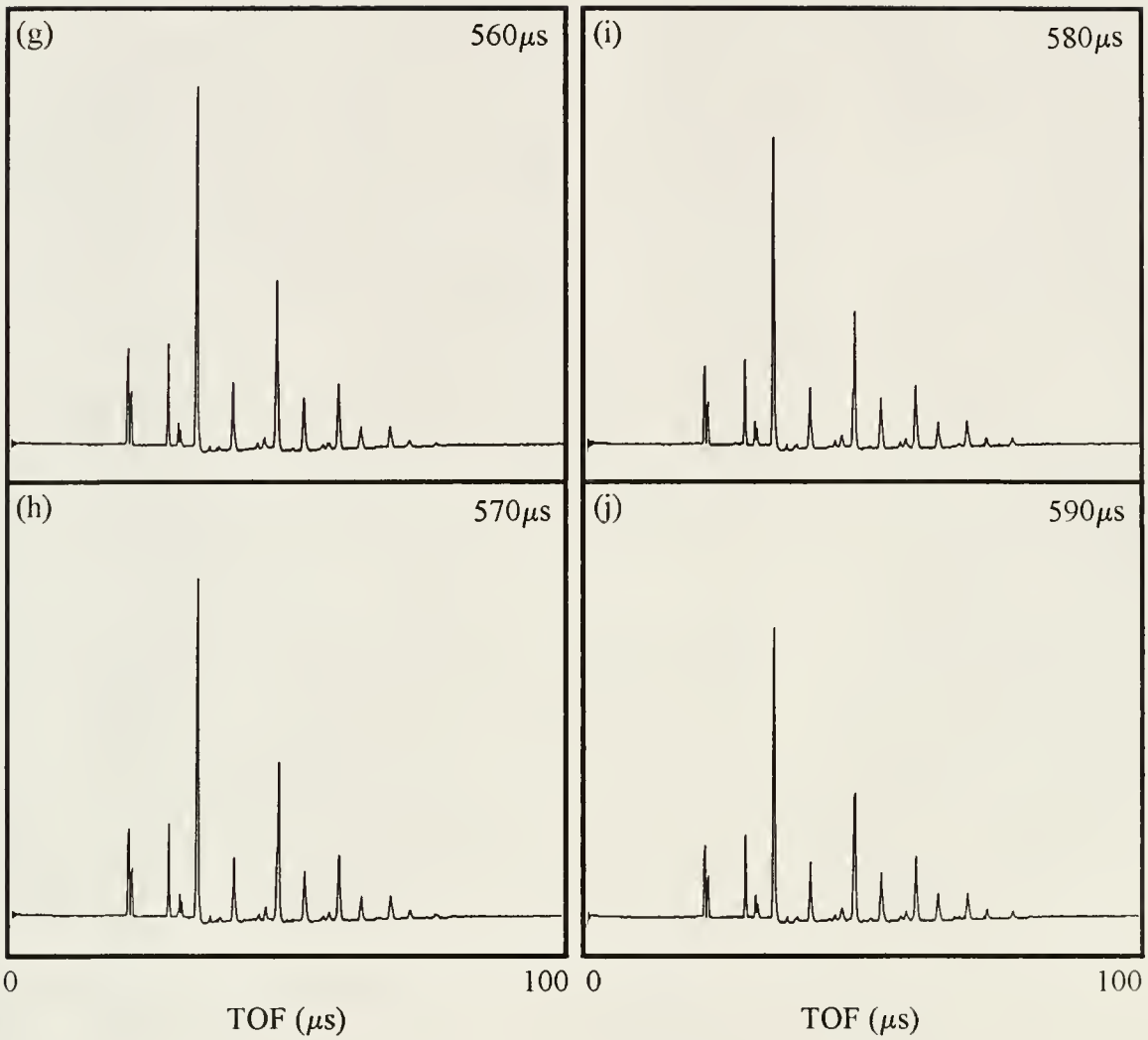

Figure 4-7 (continued)

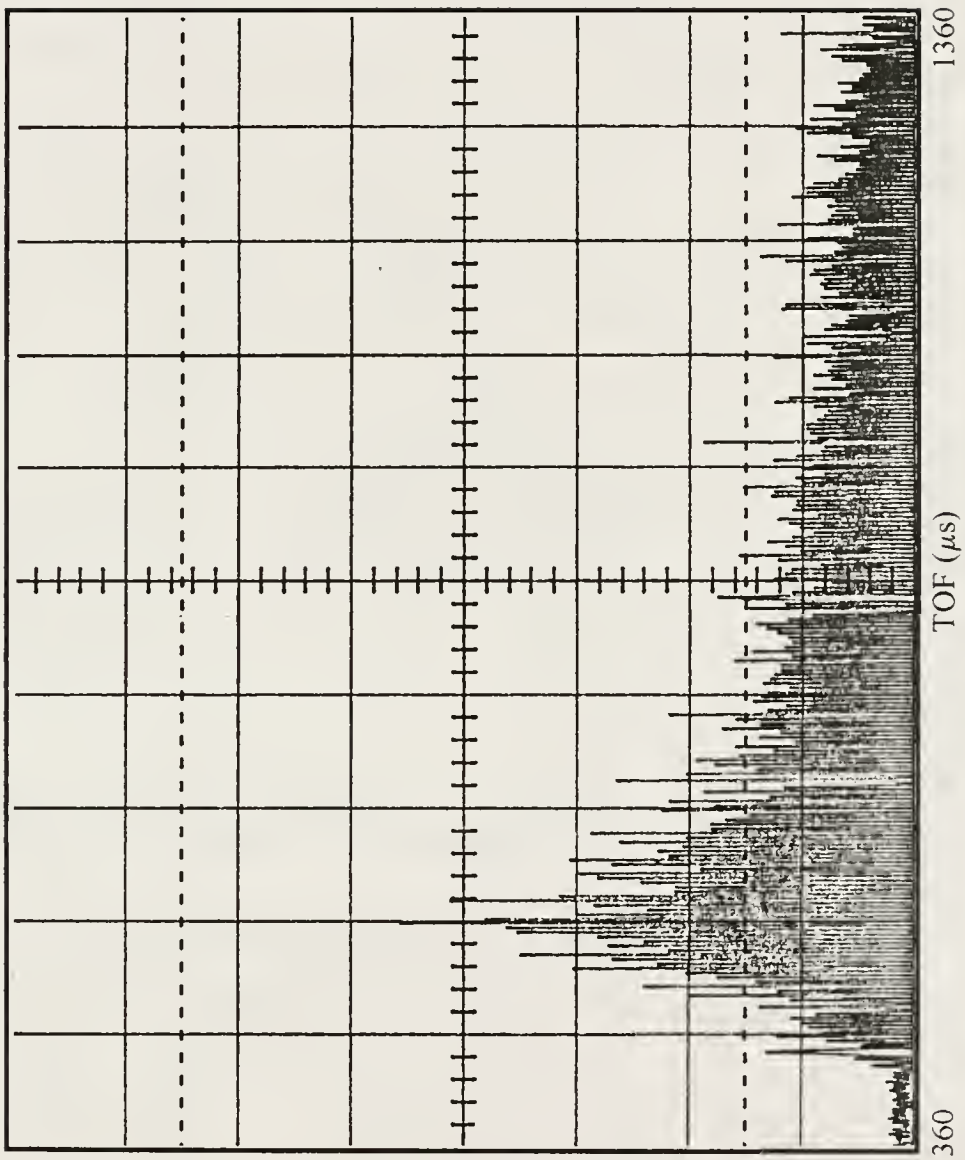

Figure 4-8 Single undeflected pulse of CO_2.

produced from a continuous source. They conclude by citing a general rule of thumb for estimating the minimum valve open time:

$$\Delta t_{min} = 4d / a_0 \qquad \text{(Eq. 4-1)}$$

where d is the nozzle diameter. The value a_0 is determined by the stagnation temperature, T_0, and is given by:

$$a_0 = (\gamma k T_0 / m)^{1/2} \qquad \text{(Eq. 4-2)}$$

where γ is the ratio of the constant pressure and constant volume heat capacities, k is the Boltzmann constant, and m is the molecular weight of the source gas.

However, since their model assumed the valve was an ideal shutter which opens and closes instantaneously, it simply serves only to define the minimum time that a valve must be fully open in order to insure at least some of the molecules reach a terminal state corresponding to the steady flow prescription for equivalent stagnation conditions. As Saenger and Fenn pointed out:

> ...it would seem a reasonably safe rule of thumb to require that the valve open time be at least $4d/a_0$. However, even this "conservative" estimate must be regarded only as a lower limit. No real valve has an opening mechanism that approximates the ideal shutter assumed in these calculations. Moreover, all the designs to date have dead volumes that act as capacitances and/or flow restrictions that may cause the effective values of P_0 [the stagnation pressure] and d to be less than their nominal values, at least for part of the pulse cycle. These factors will greatly complicate the calculation of true flow time requirements. Even rough estimate of their effects can only be made with reference to a specific valve design.[48]

It would appear from the pulse profile data obtained for CO_2, that the maximum flow from the pulsed nozzle occurs about 50 μs after the valve has begun to open. This result agrees well with the valve response characteristics reported by General Valve[53] which suggest ~ 50 μs is required for the valve to fully open. However, the pulse intensity is never truly "flat topped" but actually begins to decrease slowly beyond this initial sharp rise. It should be noted, moreover, that the nozzle used in these experiments is actually a stainless-steel capillary 46.5 mm long and thus a free jet expansion does not really exist, but rather a capillary expansion. As noted by Saenger and Fenn, flow restrictions and capacitance effects from such a long nozzle result in exceedingly complex flow conditions.

The distribution of the heavy-mass beam components appears to be slightly skewed toward the trailing end of the beam pulse--at least by the time it arrives over the deflection plates. This may in fact be due to the separation of the isomass groups within the beam pulse which occurs during the flight to the beam deflection region. If the beam pulse from our apparatus is indeed peaked (as all the experimental evidence indicates) then it is not at all unreasonable to imagine that the separation of these peaked isomass distributions would account for the slightly increased density of higher mass beam components found when chopping further into the pulse.

Because the beam pulse is affected not only by the pulse valve and nozzle hardware, but also by the source gas flow properties, the delay between the TTL pulse and arrival of the maximum beam pulse intensity is not a constant, but in fact changes slightly depending on the source gas employed. The optimum beam deflection delay can be quickly found by simply adjusting the SRS Digital Delay unit for the maximum peak intensities on the DSO. This procedure was, in fact, adopted from the very start and was generally used to determine the appropriate timing delay prior to the start of any data accumulation.

CHAPTER 5
MIXED CLUSTERS FROM C_2F_6 / N_2 COEXPANSION

Introduction

Even while calibrations and final equipment corrections were still being made, we observed that when Freon 116 (C_2F_6) was used as the source gas, a curious peak at mass 97 frequently appeared; the peak was sometimes quite pronounced while at other times it was barely visible--or not present at all. It was also noted that trace amounts of H_2O, N_2 and/or O_2 were often visible in the mass spectra due to air impurities introduced into the gas handling system.

Three plausible explanations of the peak origin were considered . The peak could be due to some impurity in the Freon 116 bottle (i.e. a hydrocarbon impurity) in which case it should appear whenever Freon 116 is present, and its intensity should be proportional to the Freon 116 concentration. A second possibility was that the peak was due to $C_2F_3O^+$, which would ostensibly require an ion-molecule reaction involving $C_2F_5^+$ and O_2, or perhaps O_2^+ and C_2F_6, and should therefore only occur in the presence of oxygen. The formation of the mixed cluster $CF_3N_2^+$ provides yet a third alternative, and would of course require the presence of nitrogen. A meticulous literature search indicated that the existence of $CF_3N_2^+$ had not been previously reported.

Early data collected without the benefit of gas manifold and filter system suggested a correlation existed between the appearance of the characteristic air peaks and the occurrence of the 97 amu peak. Even after installing a manifold and filter, numerous attempts to completely eliminate any traces of H_2O, N_2 or O_2 were unsuccessful, but a

reproducible trend did emerge. The 97 peak could be observed while supplying C_2F_6 to a gas mixing vessel initially filled with N_2. As the C_2F_6 concentration increased, the characteristic EI ion peaks would increase in intensity as well, while the N_2 peaks diminished. Of particular interest was the fact that the 97 peak, though initially not present at all with the pure N_2, would grow in and reach a maximum, then die away almost completely, even as the C_2F_6 concentration continued to increase.

Additionally, the 97 amu peak maximum appeared to be correlated to the appearance of high-mass ion peaks ($m > 138$ amu). These peaks appeared only during a certain N_2 : C_2F_6 mixture concentration range, and indicate the formation of cluster ions since their mass exceeded that of any possible parent ion. In fact, a peak at mass 147 was often observed in coincidence with the 97 amu peak and could conceivably be attributed to $C_2F_5N_2^+$, since CF_3^+ and $C_2F_5^+$ are the two most abundant ions produced during the EI ionization of C_2F_6.

Though the experimental evidence seemed to point toward the existence of $CF_3N_2^+$ (and $C_2F_5N_2^+$), it remained to additional, carefully planned experiments to show definitively which of the three proposed explanations (or combination of explanations) was indeed correct. If $CF_3N_2^+$ and $C_2F_5N_2^+$ are indeed being formed during the coexpansion of C_2F_6 and N_2, then a +2 amu mass shift should occur when $^{15}N_2$ is used instead of $^{14}N_2$; the 97 and 147 amu peaks should move to 99 and 149 amu respectively. The occurrence of such a shift would suffice to establish the existence of the proposed mixed clusters.

Experimental

A stainless steel mixing vessel (~40 mL capacity) equipped with a gas manifold and Bourdon pressure gauge was used to control the source gas composition. The manifold assembly was constructed from four Nupro SS-4H packless, bellows valves and 1/4 inch o.d. stainless steel tubing; the gas handling system was therefore completely

bakeable. Both the C_2F_6 and the N_2 were supplied from pressure regulated bottles through 1/4 inch o.d. copper tubing to the gas manifold system. The manifold valve design allowed the mixing chamber to be evacuated via a mechanical pump without breaking any of the gas lines. Additionally, the pressure of each supplied gas could be measured using the single mechanical pressure gauge. The mixed gas then passed through a filter/drier and entered the stagnation region around the pulse valve.

A final attempt was made to eliminate any trace amounts of H_2O or O_2 from the gas handling system through the use of standard vacuum techniques. As in many of the previous C_2F_6/N_2 coexpansion experiments, the mixing vessel, while not in use, was evacuated through the mechanical pump and baked with heat tape at $\sim 150°F$; however, for this particular run, after the mixing vessel had cooled down the morning of the experiment, the filter/drier was packed in dry ice to create a cryogenic pump to remove water and other low volatiles from the source gas stream. The Freon 116 used in these experiments was procured from Matheson and the natural abundance N_2 was obtained from BiTech.

The experiment was begun with only N_2 at 15 psig supplied to the mixing vessel--the C_2F_6 manifold valve was closed. After the equipment parameters had been adjusted and a good N_2 spectrum had been obtained, the N_2 manifold valve was closed and the C_2F_6 valve was opened, allowing only 15 psig C_2F_6 to flow into the mixing vessel as the pulse valve continued firing. Thus, the C_2F_6 concentration, though initially zero, gradually increased over time as the N_2 concentration decreased. This dynamic concentration effect was monitored spectroscopically by acquiring TOF mass spectra of the pulsed beam every 15 minutes; each spectrum was accumulated from 2,000 single-shot spectra acquired at a collection rate of 4 Hz.

The system was configured with no slit, and a deflection voltage rise time of 30 ns was used throughout. The pulse valve was set at 200 μs duration and 8 Hz. The source gas stagnation temperature was $\sim 108°F$. The 0.030 inch i.d. nozzle was held at +550 V,

while the 2 mm i.d. skimmer was maintained at +545 V. Both Einzel lenses were held at +340 V. As always, the electron gun supplied 120 eV electrons with a measured current of ~200 μA at the collection plate. Typical pressures during the run were $\leq 5\times10^{-5}$ torr in the ion source chamber, 5×10^{-7} torr in the ion optics/beam deflection region, and 1×10^{-6} torr near the detector.

Because of the sensitivity/resolution trade off mentioned in Chapter 3, a second series of spectra were collected using a 0.5 mm slit and deflection voltage rise time of 2200 ns in order to gain better resolution. (A faster deflection voltage rise time was not used due to unacceptable reduction in S/N). The experimental parameters were essentially the same except the first Einzel lens was held at +340 V and the second Einzel lens was kept at +200 V; this Einzel lens configuration was found to yield better peak resolution when employing a 0.5 mm slit and deflection voltage rise time of 2200 ns. Also, the filter/drier was not cooled with dry ice for this series of spectra, but was simply left at room temperature.

A third experiment was conducted very much like the one described above except $^{15}N_2$ (99 atom %) was used. One liter of $^{15}N_2$ was obtained from Cryogenic Rare Gas at a cost of $460. In order to observe a 2 amu isotopic shift, high resolution was deemed more desirable than high sensitivity; thus, the 0.5 mm slit configuration was employed. System parameters were optimized using $^{14}N_2$ before introducing $^{15}N_2$ into the system. The filter/drier was not cooled.

As before, the mixing vessel was initially filled with $^{15}N_2$, but a pressure of only 9 psig was possible due to the rather large volume of the lecture bottle in which the 1 L of $^{15}N_2$ was supplied. After the initial spectrum of pure $^{15}N_2$ was obtained, the pressure had fallen to 7 psig and this, then, was the stagnation pressure maintained throughout the rest of the experiment through the addition of C_2F_6 at 7 psig (the $^{15}N_2$ manifold valve was now closed). As in the previous two experiments, 2,000 single-shot spectra were accumulated every 15 minutes and used to track the ion beam composition as the relative

concentrations of C_2F_6 and $^{15}N_2$ changed with time. The nozzle and skimmer potentials were at +550 V and +545 V respectively, the first Einzel lens was held at +340 V, and the second Einzel lens was kept at +200 V. Therefore, aside from the source gas pressure changes, essentially the same system conditions existed as were noted for the $^{14}N_2$ experiment using a 0.5 mm slit.

Results and Discussion

The results of the $C_2F_6/^{14}N_2$ coexpansion experiment conducted without a slit are displayed in Figure 5-1. Figure 5-1(a) was taken prior to opening the C_2F_6 manifold valve, and therefore establishes the mass spectrum arising from the expansion of essentially pure nitrogen without the presence of C_2F_6. Figure 5-1(b) was collected immediately after the C_2F_6 valve was opened. The series shows the change in the ion beam composition as the source gas ratio of C_2F_6:$^{14}N_2$ was increased. The last spectrum, Figure 5-1(q), was obtained after evacuating the mixing vessel, and then filling it with C_2F_6 at 15 psig; it therefore establishes the mass spectrum arising from the expansion of essentially pure C_2F_6.

In an attempt to better depict the overall trend observed during the 3 1/2 hours in which the experiment was run, every other spectrum (9 of the 17 total) were carefully analyzed and converted into the stacked, 3-dimensional graph shown in Figure 5-2. Each spectrum was painstakingly analyzed to establish each peak position as precisely as possible. Normalized peak intensities were also estimated by triangularizing each peak and computing the area contained within. Flight times were also converted into ion masses. The peak width measured for the N_2^+ peak (28 amu) was ~270 ns FWHM for a resolution ($m/\Delta m$) of 51.

Figures 5-1 and 5-2 both clearly show enhanced cluster composition within the beam occurring only during a certain time period; of course, since the source gas

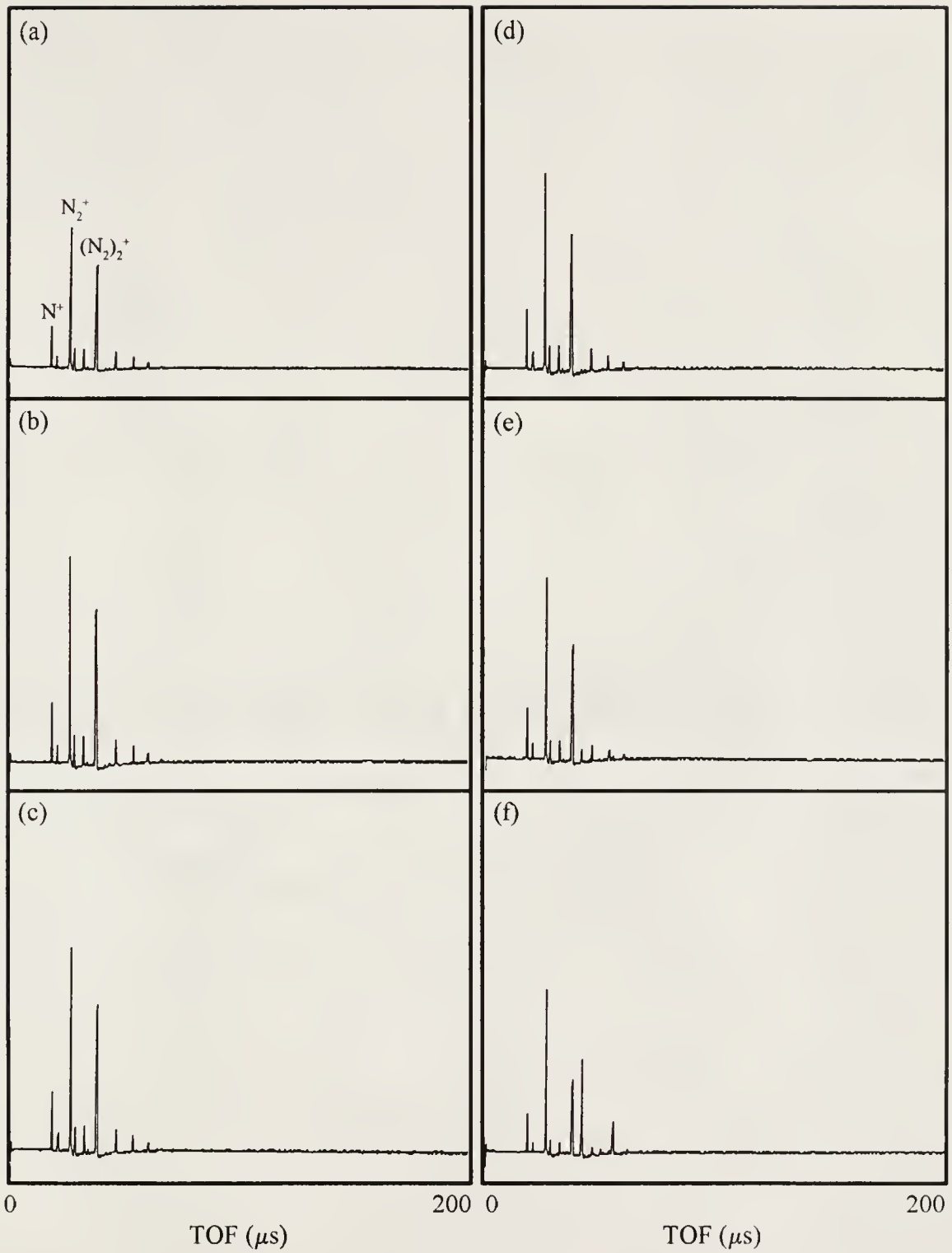

Figure 5-1 TOF mass spectra of N_2/C_2F_6 coexpansion. (a) Pure N_2; (b) Initial spectrum taken when addition of C_2F_6 was started and N_2 valved off; Spectra (c) - (p) were taken at 15 minute intervals as $[C_2F_6]$ increased; (q) ~ pure C_2F_6. (continued on next two pages)

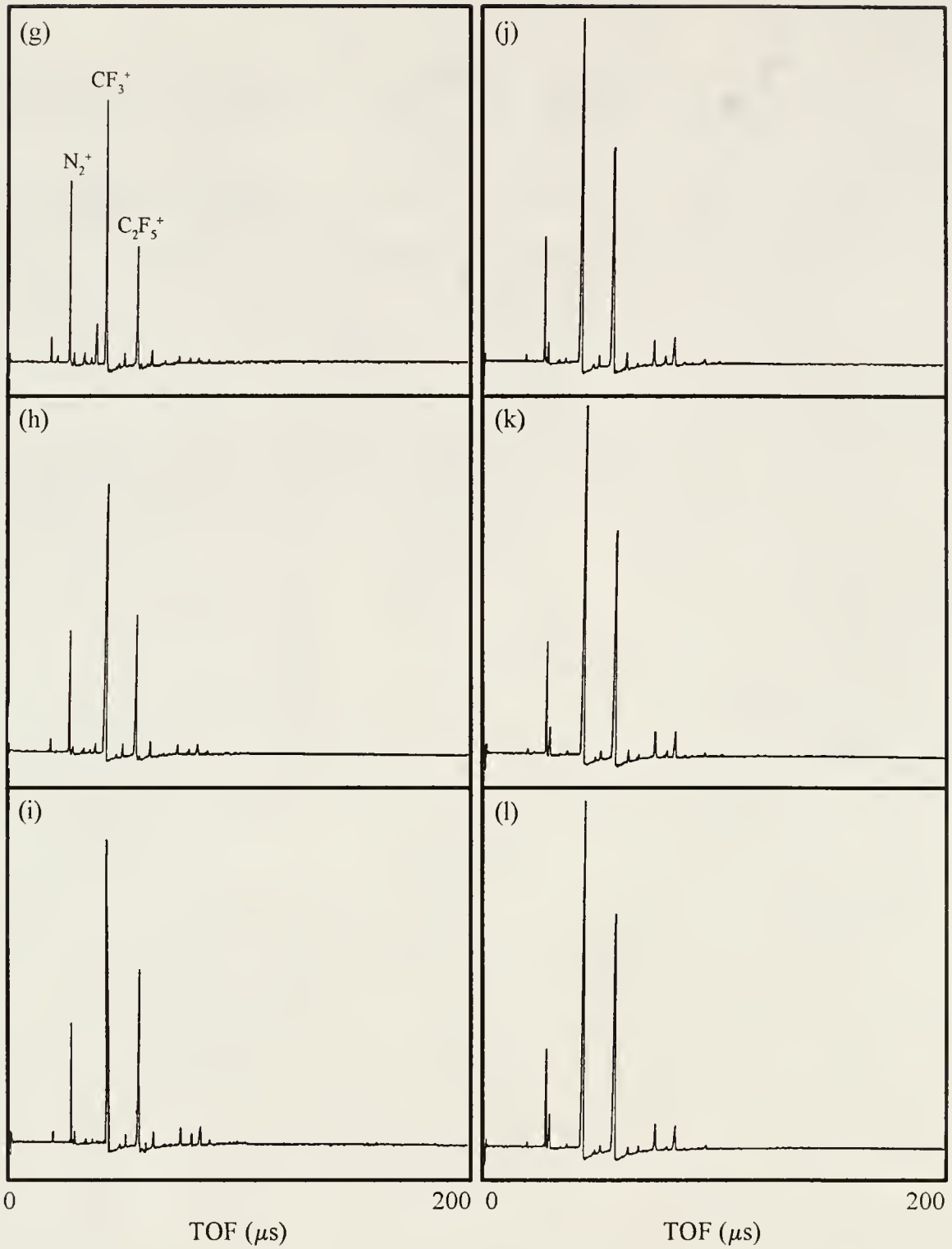

Figure 5-1 (continued)

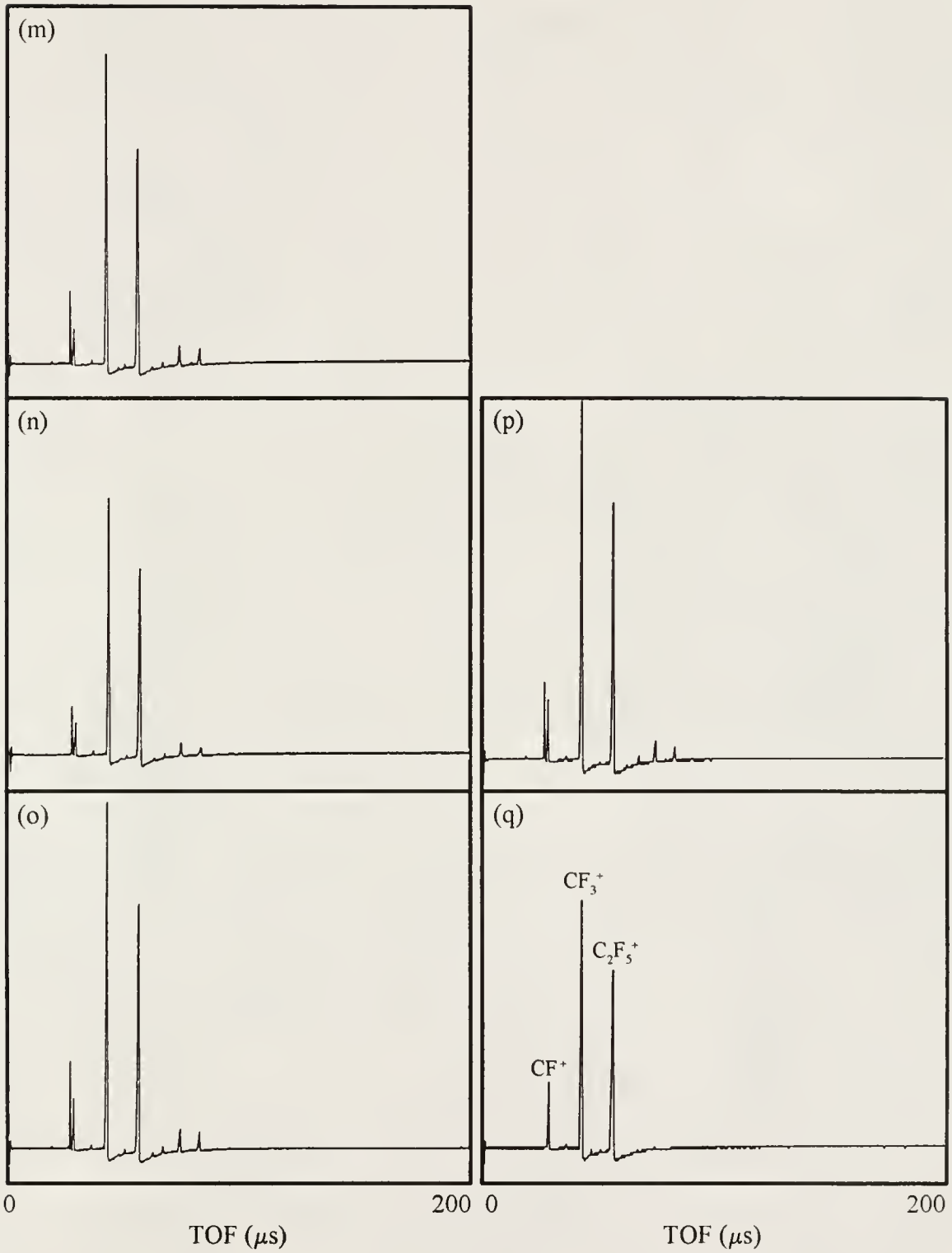

Figure 5-1 (continued)

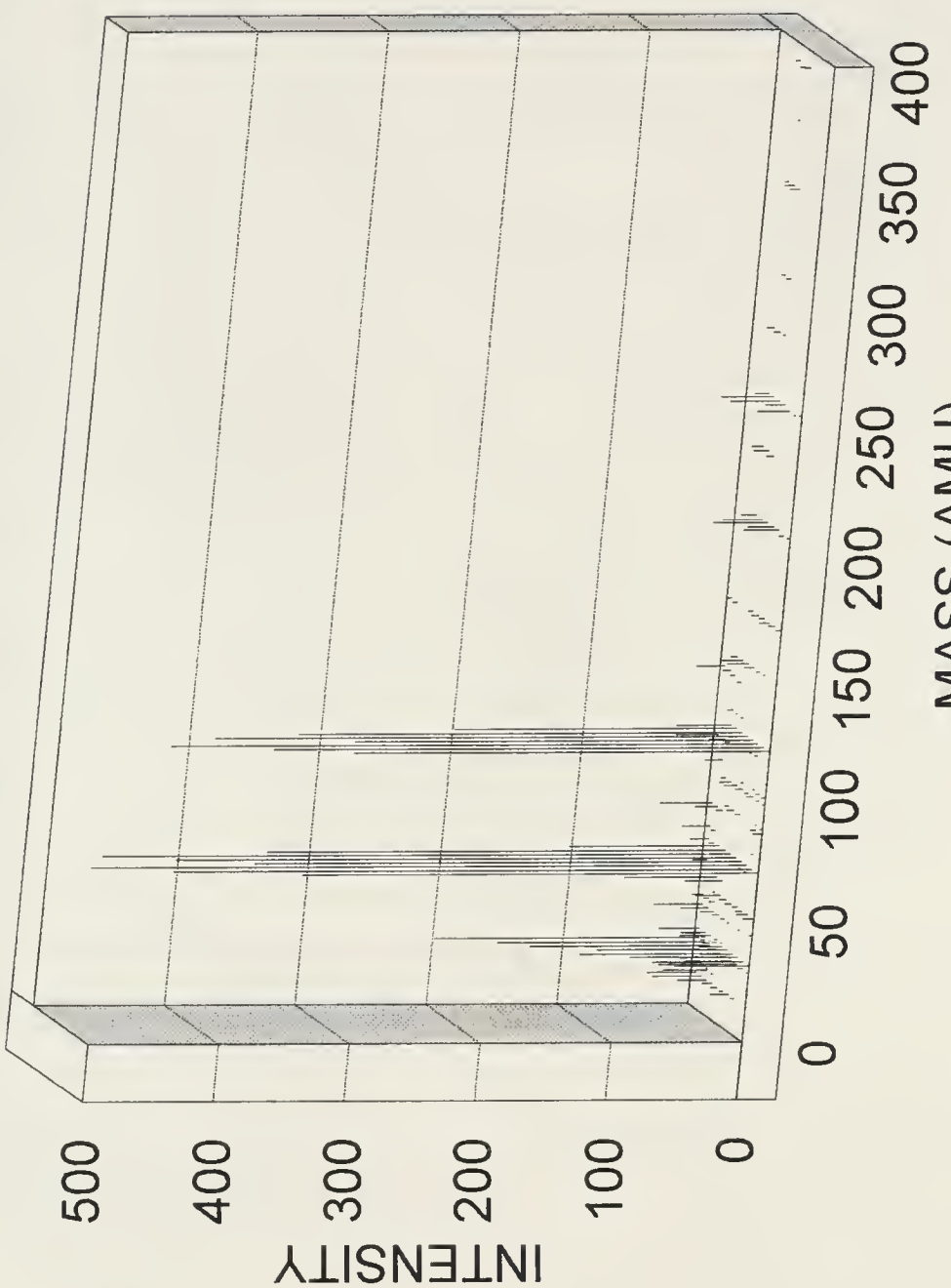

Figure 5-2(a) 3-D view of mixed cluster study spectra. Pure nitrogen spectrum is against the back wall.

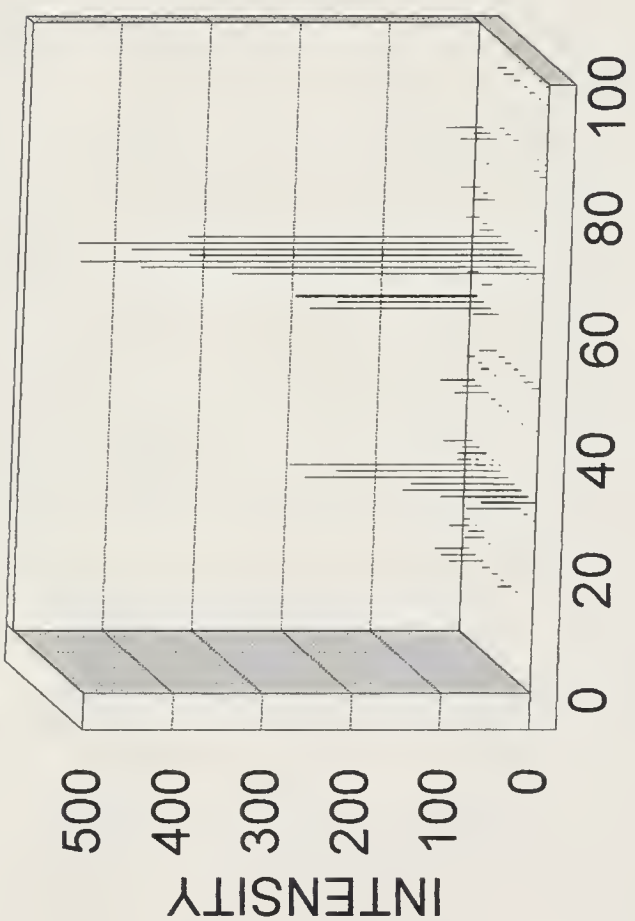

Figure 5-2(b) Expanded view of 0 - 100 amu region.

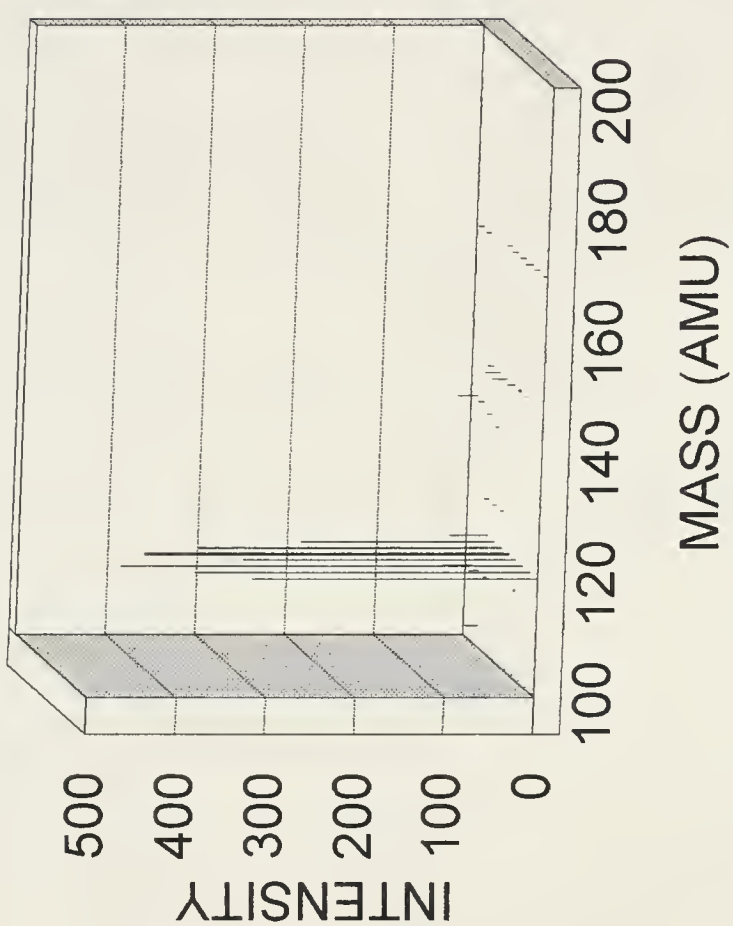

Figure 5-2(c) Expanded view of 100 - 200 amu region.

composition is gradually changing with time, this indicates that the formation of the heavy-mass clusters is favored only when a specific C_2F_6:$^{14}N_2$ composition is present in the source gas. The 97 peak intensity is also greatest during this period of enhanced clustering; a closer view of this segment of the mass spectrum is shown in Figures 5-2(b) and 5-2(c).

A similar series was obtained using the 0.5 mm slit. Though the sensitivity was reduced significantly from that obtained without a slit, the resolution measured for the N_2^+ peak increased to 199 (m/Δm). Thus, by combining the information from both runs, a more precise understanding of the system behavior can be had. Since the 0.5 mm slit run provided better resolution, the spectrum containing the highest intensity 97 peak was chosen for comparison with the $C_2F_6/^{15}N_2$ results in which an isotopic shift is predicted. The spectrum selected is presented in Figure 5-3 along with a calibration curve in Figure 5-4 of the square root of the ion mass vs. the TOF.

The spectra collected during the $C_2F_6/^{15}N_2$ experiment were characterized by reduced peak intensities due to the lower source pressure which we were forced to use. However, the suspected mixed clustering was still observed with a resolution comparable to that of the $C_2F_6/^{14}N_2$ work using the 0.5 mm slit. Again, the best spectrum was chosen, in which the peaks of interest were most pronounced, to compare with the best $C_2F_6/^{14}N_2$ spectrum. The selected spectrum along with a mass calibration curve are shown in Figures 5-5 and 5-6 respectively.

Thus, the outcome of the ^{15}N isotope study remained in the careful analysis of two spectra. A mass shift of +2 amu was indeed observed for the 97 and 147 peaks as shown in Figure 5-7. As depicted in the graphical comparison of the two spectra, the large CF_3^+ and $C_2F_5^+$ peaks are aligned, as well as the peaks identified as $CF_3(H_2O)^+$, $CF_3(C_2F_6)^+$ and $C_2F_5(C_2F_6)^+$. It should be noted that a rather large $(N_2)_2^+$ peak appears in the $C_2F_6/^{14}N_2$ spectrum and not in the $C_2F_6/^{15}N_2$ spectrum. This is not totally unexpected since the $^{15}N_2$ stagnation pressure was only about half that for the $^{14}N_2$ run; the stagnation conditions of

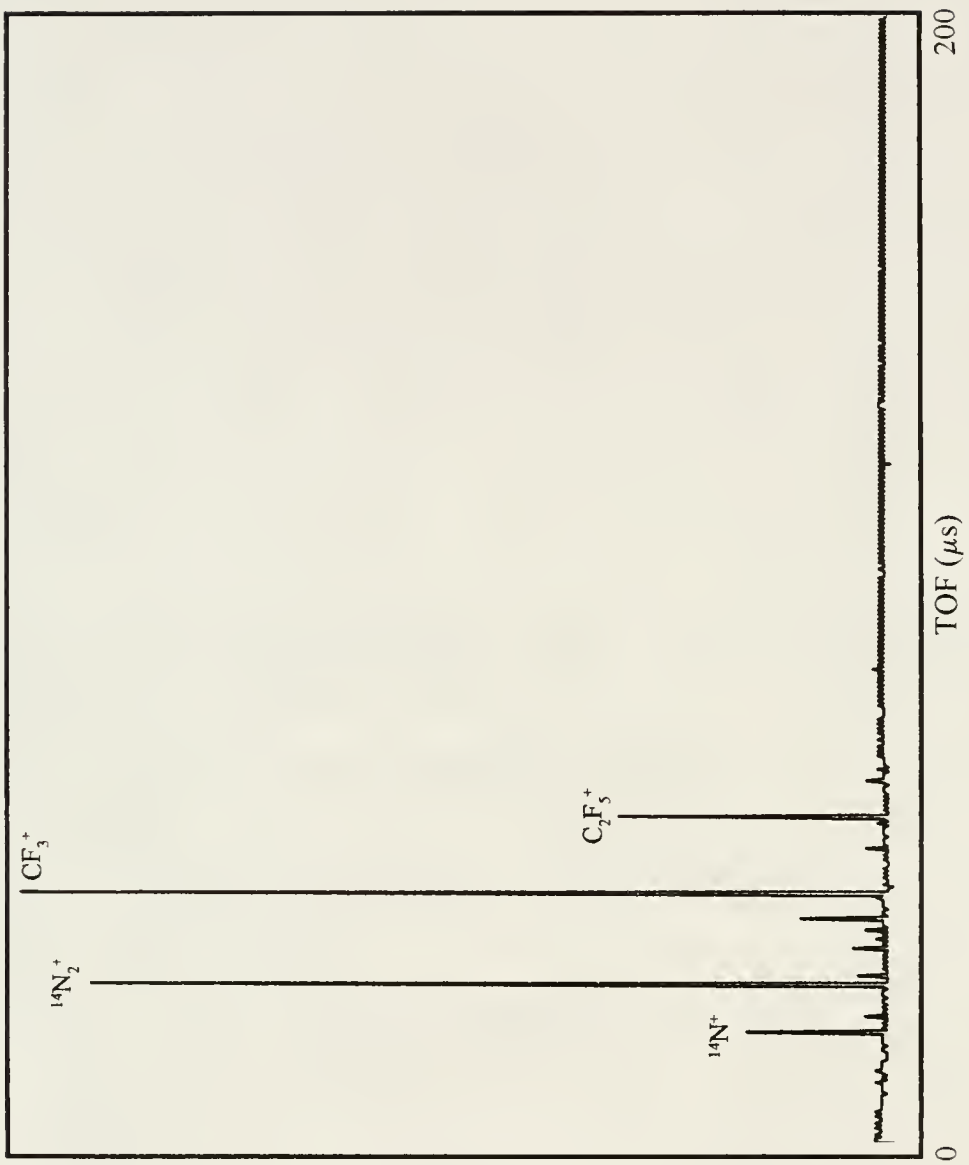

Figure 5-3 Best TOF mass spectrum from $C_2F_6/^{14}N_2$ experiment.

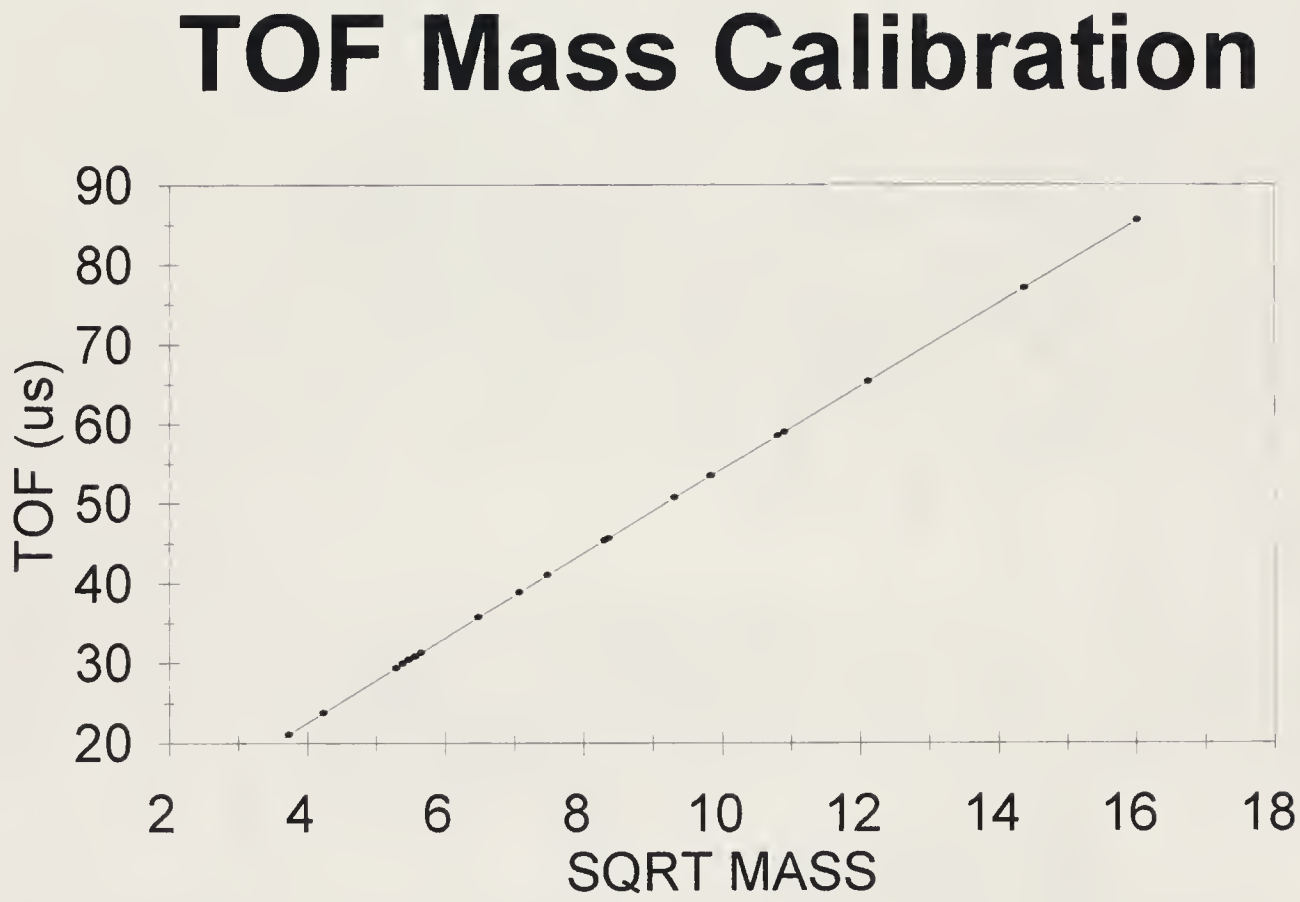

Figure 5-4 Mass calibration curve from N-14 experiment.

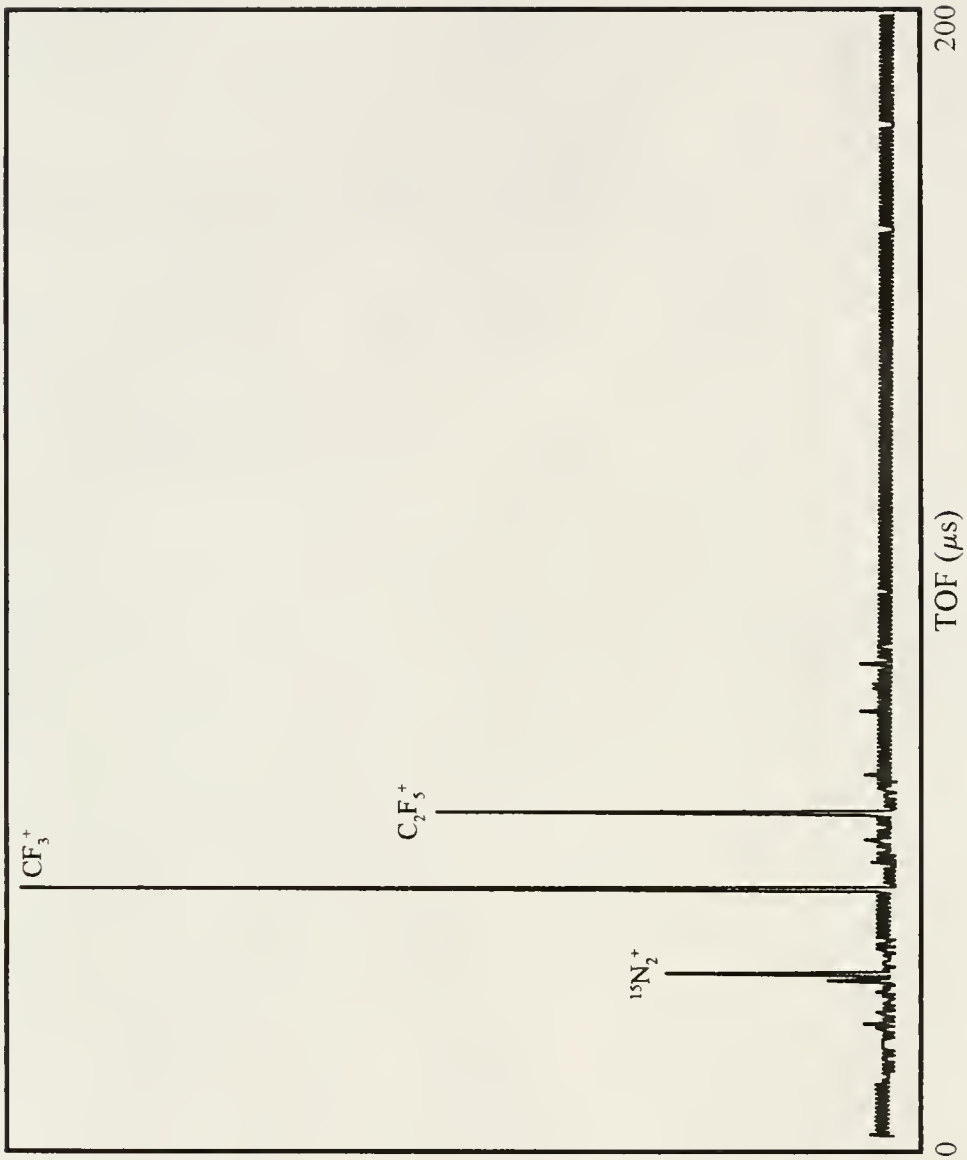

Figure 5-5 Best TOF mass spectrum from $C_2F_6/^{15}N_2$ expriment

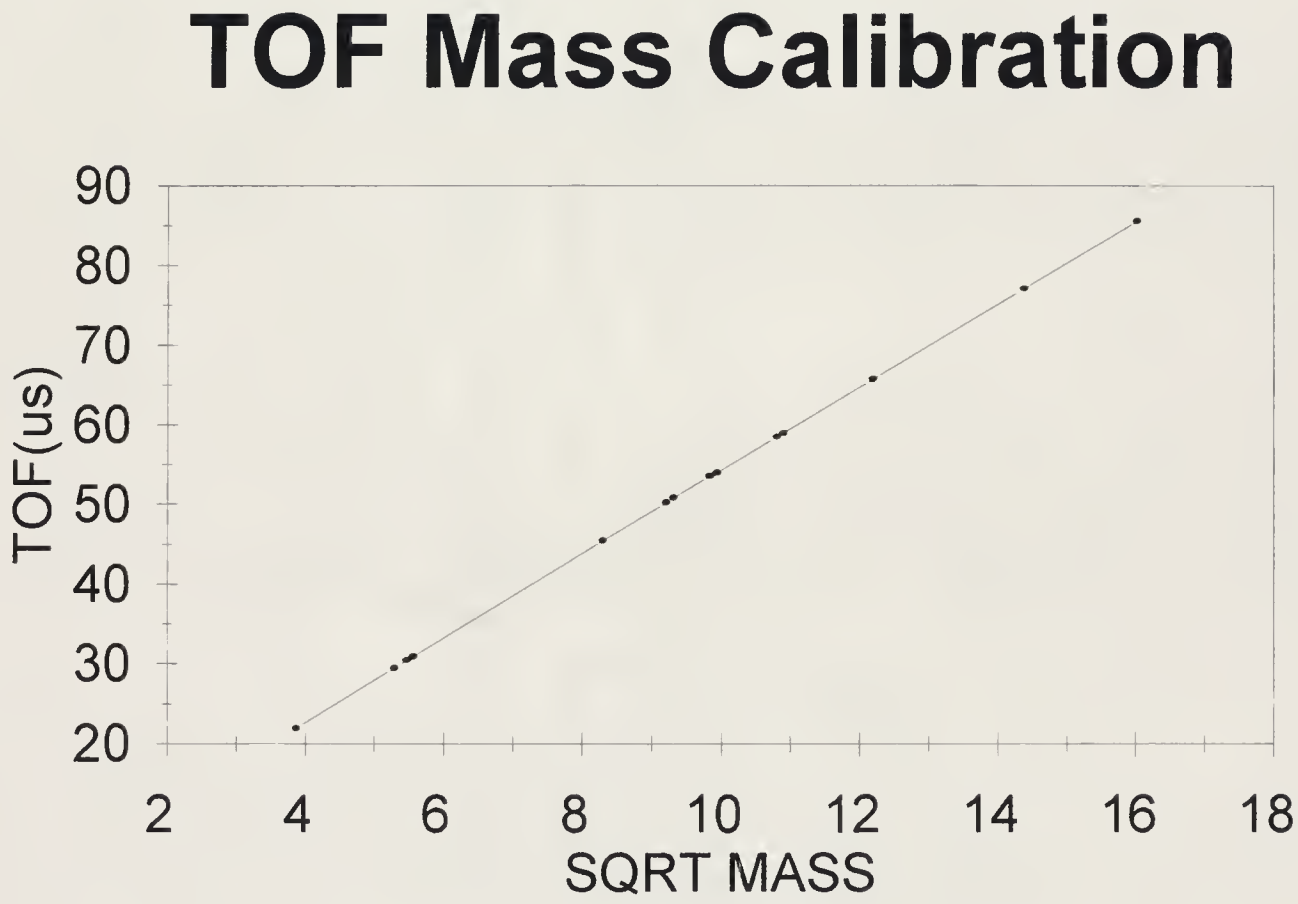

Figure 5-6 Mass calibration curve from N-15 experiment.

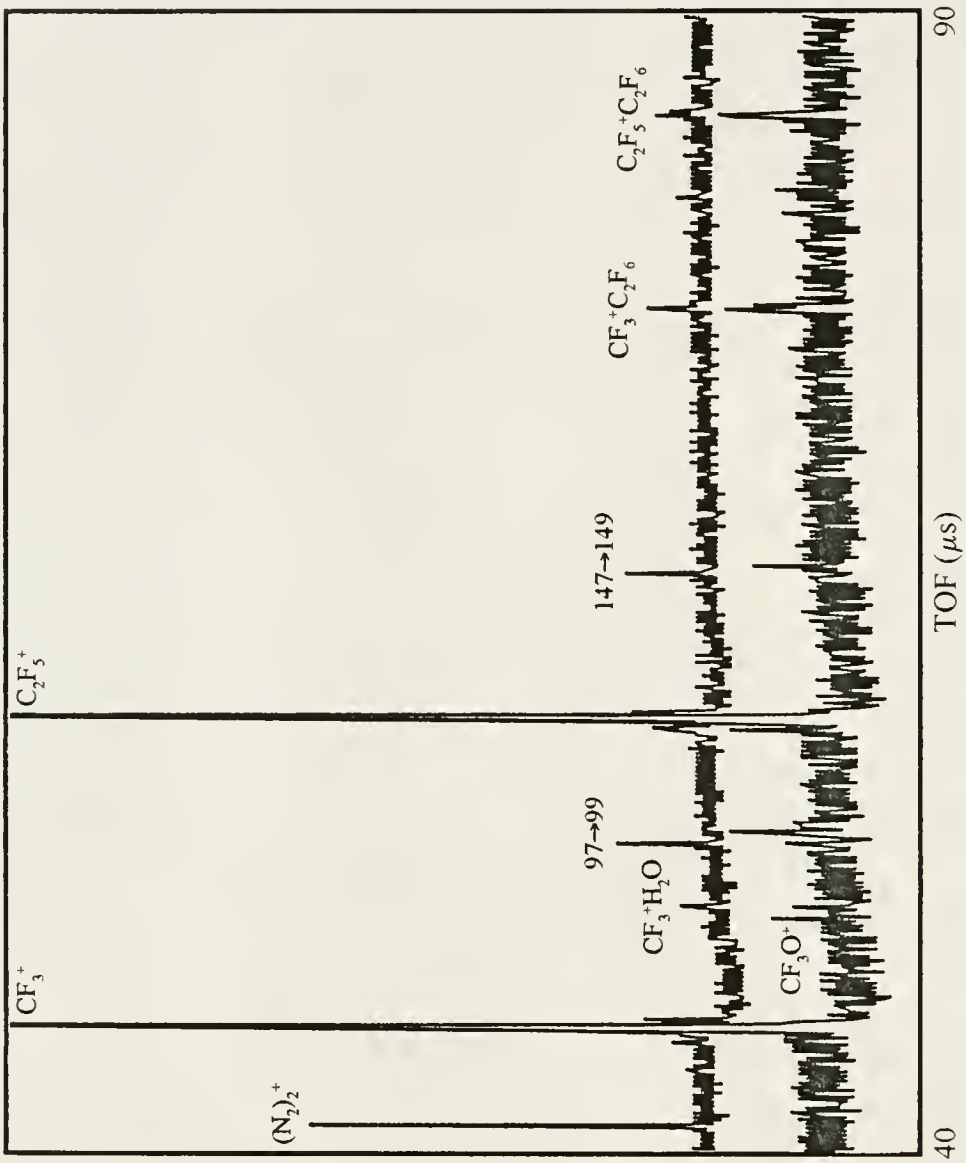

Figure 5-7 Comparison of $C_2F_6/^{14}N_2$ and $C_2F_6/^{15}N_2$ spectra. Isotopic shifts are noted.

the two experiments were not identical. Also, a small peak at 85 amu appears in the $C_2F_6/^{15}N_2$ spectrum, and is probably due to an O addition to CF_3^+.

Thus, the identity of the two peaks initially seen at 97 and 147 amu can now be assigned respectively as $CF_3(N_2)^+$ and $C_2F_5(N_2)^+$. Both peaks provide solid evidence of mixed clustering from the coexpansion of nitrogen and Freon 116 over a relatively narrow range of mixture concentrations. Possible structures are illustrated in Figure 5-8; the structures involving N_2 σ-orbitals (b, d) appear to be intuitively more stable. Geometry optimization calculations would, of course, provided quantitative information regarding their relative stabilities.

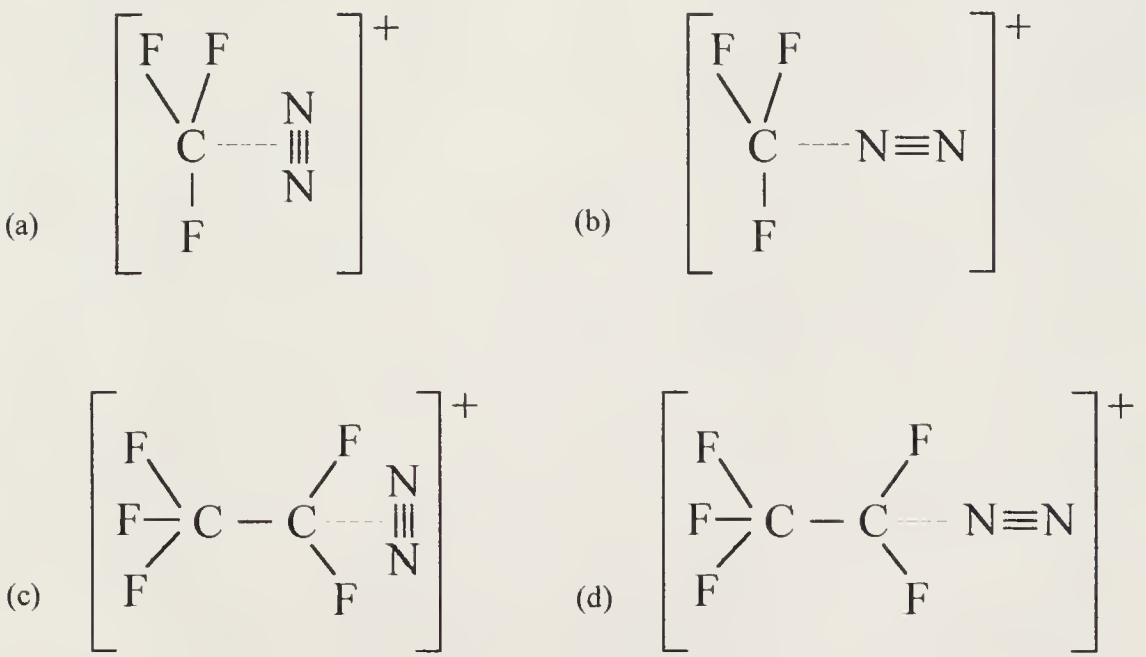

Figure 5-8 Possible structures for $CF_3N_2^+$ and $C_2F_5N_2^+$.

Empirical geometry calculations and phase studies for pure C_2F_6 neutral clusters have been accomplished.[69,70] Pure nitrogen cluster ion stabilities have also been investigated both experimentally and theoretically.[71,72] In a very recent paper by Shang et al.[3] the solvation effects of nonpolar solvents (including C_2F_6) on specific electronic transitions occurring in certain bicyclo-octanes were studied by forming neutral solute/solvent clusters in a supersonic expansion.[73] However, mixed cluster ions arising from the coexpansion of C_2F_6 and N_2 have not been previously reported.

Small ionic clusters are known to play an important role in stratospheric chemistry.[74] Moreover, the role played by chlorofluorocarbons (CFC's) in the depletion of the ozone layer has attracted world-wide attention and concern. It would seem that further investigation of the interaction between Freon 116 (and especially chlorine containing Freons) with nitrogen would likely add to our understanding of the novel chemistry which occurs many miles above the surface of the earth.

APPENDIX A
MATHEMATICAL DERIVATIONS

Purpose

In order to fully understand the behavior of an ion beam chopped (or modulated) via a beam deflection technique, it is first necessary to derive the equations of motion which apply. Next, a shutter function must be constructed which calculates the portion of the beam passed by the slit as a function of the beam position, and finally the thermal velocity distribution of each isomass packet must be adequately described. These sets of equations provide the mathematical framework for the ion trajectory code TRAJION (cf. Appendix B).

Equations of Motion

Because of symmetry, the beam deflection problem can be considered in just two dimensions, where fully accelerated cations of velocity v_x traverse the system in the positive x direction at constant velocity; ions encounter only perpendicular accelerations in the y direction while passing between two parallel deflection plates (fringing fields will not be addressed). Such a model can be readily divided into three separate regions as shown in Figure A-1. Region I is a pre-acceleration region where the ions drift towards the parallel plates, Region II. It is in Region II where the ions are accelerated perpendicular to the x-axis by varying the electric field between the plates, thus causing the beam to be swept across the slit. The ions are again in a field free environment once they enter

Region III where they drift toward the detector impact plate, but now with both x and y velocity components.

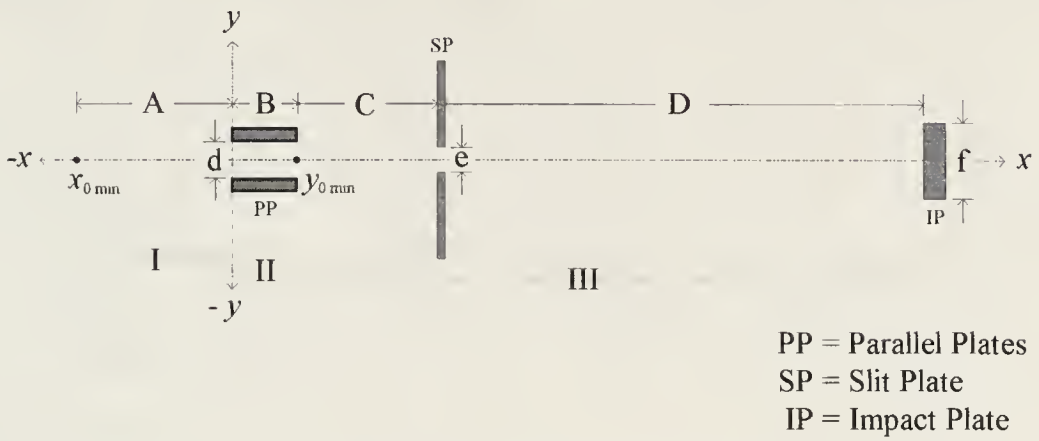

Figure A-1 Schematic diagram of a generic beam deflection apparatus.

In order to track the trajectory of a given ion, its position and velocity must be known for any time t; for convenience, we will define t_0 as the instant the electric field between the parallel plates begins to change, i.e. when the positive high voltage applied to the lower plate begins to decrease. Additionally, the beam entering the first pre-acceleration region is assumed to be well collimated and approaches the deflection plates in a path parallel to the plates.

Region I (Pre-acceleration)

Since ions receive no accelerations in this region, the equations of motion are quite simple. If an ion enters the region with an initial x-velocity, v_x , then we can write:

$$v_x = \frac{dx}{dt} \qquad \text{(Eq. A-1)}$$

and integrating over some distance $x - x_0$, and corresponding time, $t - t_0$, yields:

$$\int_{x_0}^{x} dx = \int_{t_0}^{t} v_x dt \qquad \text{(Eq. A-2)}$$

or

$$x - x_0 = v_x t - v_x t_0 \qquad \text{(Eq. A-3)}$$

where $t_0 \equiv 0$, and

$$v_x = \sqrt{\frac{2T}{m}} \qquad \text{(Eq. A-4)}$$

where m = mass, and T = kinetic energy. Substituting for t_0 and v_x gives the final result:

$$x(t) = x_0 + t\sqrt{\frac{2T}{m}} \qquad \text{(Eq. A-5)}$$

Similarly, an expression like Eq. A-3 can be written for the y component of motion:

$$y(t) = y_0 + v_y t \qquad \text{(Eq. A-6)}$$

but for a well collimated beam, $v_y \equiv 0$, thus

$$y(t) = y_0 \qquad \text{(Eq. A-7)}$$

where y_0 is the initial y displacement.

Region II (Acceleration)

Variable acceleration. Ions entering the region between the parallel plates can encounter at most three different electric field conditions: 1) ions already between the plates when the high voltage on the lower plate begins to swing negative (t_0) have experienced a constant maximum acceleration in the positive y direction, 2) once the voltage on the lower plate starts down, ions between the plates receive a variable, time dependent acceleration, and 3) ions still between the plates after the lower plate has reached its maximum negative value receive a constant maximum acceleration in the negative y direction. The time dependent, variable acceleration case will be considered first.

Since the electric field generated by the parallel plates is perpendicular to the ion motion v_x , Eqs. A-4 and A-5 still apply. However, the ions are no longer in a field free region, but are instead in a varying electric field. Thus:

$$\frac{dv_y}{dt} = a_y \qquad \text{(Eq. A-8)}$$

where a_y is the acceleration in the y direction. Integrating over the velocity range v_y - v_{y1} and corresponding time interval t - t_1 gives:

$$\int_{v_{y_1}}^{v_y} dv_y = \int_{t_1}^{t} a_y dt \qquad \text{(Eq. A-9)}$$

where $a_y = f(t)$. In order to evaluate the integral, the time dependence of a_y must be determined. Figure A-2 details the idealized behavior of the lower plate voltage over the decay period τ.

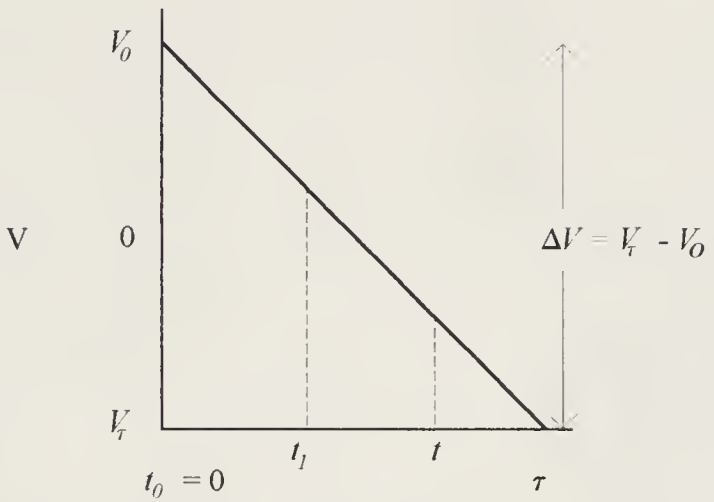

Figure A-2 Voltage on lower plate as a function of time.

In general, an ion of mass, m, and charge, q, will experience a force, F, parallel to the electric field, E, established between the parallel plates in accordance with the relationship:

$$F = Eq \qquad \text{(Eq. A-10)}$$

And of course, for non relativistic conditions we can always write:

$$F = ma \qquad \text{(Eq. A-11)}$$

thus

$$a = \frac{Eq}{m} \qquad \text{(Eq. A-12)}$$

But the electric field between the parallel plates is simply a function of the applied plate voltage, V, and the plate separation distance, d:

$$E = V/d \qquad \text{(Eq. A-13)}$$

and the plate voltage, according to our model (cf. Figure A-2), is a linear function of time

$$V = \left(\frac{\Delta V}{\tau}\right)t + V_0 \qquad \text{(Eq. A-14)}$$

therefore, we can now write a time dependent expression for a_y:

$$a_y(t) = \frac{q\Delta V}{md\tau}t + \frac{qV_0}{md} \qquad \text{(Eq. A-15)}$$

Eq. A-9 can now be written as follows:

$$\int_{v_{y1}}^{v_y} dv_y = \frac{q\Delta V}{md\tau}\int_{t_1}^{t} t\,dt + \frac{qV_0}{md}\int_{t_1}^{t} dt \qquad \text{(Eq. A-16)}$$

and evaluating the integral gives:

$$v_y - v_{y1} = \frac{q\Delta V}{2md\tau}\left(t^2 - t_1^2\right) + \frac{qV_0}{md}\left(t - t_1\right) \qquad \text{(Eq. A-17)}$$

Thus, the y-velocity of an ion traversing the parallel plate region while the electric field is changing is given by:

$$v_y(t) = v_{y_1} + \frac{q}{md}\left[\frac{\Delta V}{2\tau}\left(t^2 - t_1^2\right) + V_0\left(t - t_1\right)\right] \qquad \text{(Eq. A-18)}$$

In order to trace the trajectory of an ion, the position as well as velocity must be known. The y-coordinate can be found by integrating Equation A-18 as shown below:

$$v_y = \frac{dy}{dt} = v_{y_1} + \frac{q}{md}\left[\frac{\Delta V}{2\tau}\left(t^2 - t_1^2\right) + V_0\left(t - t_1\right)\right] \qquad \text{(Eq. A-19)}$$

and integrating linear combinations of Equation A-19 gives:

$$\int_{y_1}^{y} dy = \int_{t_1}^{t} v_{y_1}\,dt + \frac{q\Delta V}{2md\tau}\int_{t_1}^{t} t^2\,dt - \frac{q\Delta V}{2md\tau}\int_{t_1}^{t} t_1^2\,dt$$

$$+ \frac{qV_0}{md}\int_{t_1}^{t} t\,dt - \frac{qV_0}{md}\int_{t_1}^{t} t_1\,dt \qquad \text{(Eq. A-20)}$$

which evaluates to:

$$y - y_1 = v_{y_1}\left(t - t_1\right) + \frac{q\Delta V}{6md\tau}\left(t^3 - t_1^3\right) - \frac{q\Delta V}{2md\tau}t_1^2\left(t - t_1\right) + \ldots$$

$$+\frac{qV_0}{2md}\left(t^2-t_1^2\right)-\frac{qV_0}{md}t_1\left(t-t_1\right) \qquad \text{(Eq. A-21)}$$

Multiplying through and solving for y yields:

$$y=y_1+v_{y_1}\left(t-t_1\right)+\frac{q\Delta V}{6md\tau}t^3-\frac{q\Delta V}{6md\tau}t_1^3-\frac{q\Delta V}{2md\tau}t_1^2t$$

$$+\frac{q\Delta V}{2md\tau}t_1^3+\frac{qV_0}{2md}t^2-\frac{qV_0}{2md}t_1^2-\frac{qV_0}{md}t_1t+\frac{qV_0}{md}t_1^2 \qquad \text{(Eq. A-22)}$$

$$=y_1+v_{y_1}\left(t-t_1\right)+\frac{q\Delta V}{6md\tau}t^3+\frac{2q\Delta V}{6md\tau}t_1^3-\frac{3q\Delta V}{6md\tau}t_1^2t$$

$$+\frac{qV_0}{2md}t^2+\frac{qV_0}{2md}t_1^2-\frac{2qV_0}{2md}t_1t$$

$$=y_1+v_{y_1}\left(t-t_1\right)+\frac{q\Delta V}{6md\tau}\left(t^3-3t_1^2t+2t_1^3\right)+\frac{qV_0}{2md}\left(t^2-2t_1t+t_1^2\right)$$

or more succinctly:

$$y(t)=y_1+v_{y_1}\left(t-t_1\right)+\frac{q\Delta V}{6md\tau}\left(t^3-3t_1^2t+2t_1^3\right)+\frac{qV_0}{2md}\left(t-t_1\right)^2 \qquad \text{(Eq. A-23)}$$

Constant Acceleration. Ions between the parallel plates before ($t < 0$) or after the electric field has changed ($t > \tau$) experience a constant acceleration perpendicular to the x-axis. The magnitude of the force exerted on the ions under these conditions is the same in both cases, and is a maximum. The direction, however, is not the same, and is in fact

opposite for the two cases. Because of the obvious symmetry involved, a general solution for the constant acceleration case will be solved first.

As always, Equations A-4 and A-5 apply for motion in the *x*-direction. In order to determine the *y* component of the ion motion we begin by integrating Equation A-9 where a_y is now a constant:

$$\int_{v_{y_i}}^{v_y} dv_y = \int_{t_i}^{t} a_y dt \qquad \text{where} \quad a_y = \frac{qV}{md} \equiv \text{constant} \qquad \text{(Eq. A-9)}$$

which evaluates to:

$$v_y - v_{y_i} = \frac{qV}{md}(t - t_i) \qquad \text{(Eq. A-24)}$$

Rearranging to solve for the *y* velocity component at a given time, *t*, and adding the specific conditions for the two original cases yields the result:

$$v_y(t) = v_{y_i} + \frac{qV}{md}(t - t_i) \qquad \text{where} \quad V = V_0 \ \text{ if } \ t_i < 0 \qquad \text{(Eq. A-25)}$$

$$V = V_\tau \ \text{ if } \ t > \tau \ \text{ (cf. Fig. A-2)}$$

The y coordinate position is obtained by integrating Equation A-25 as follows:

$$v_y = \frac{dy}{dt} = v_{y_i} + \frac{qV}{md}(t - t_i) \qquad \text{(Eq. A-26)}$$

and

$$\int_{y_1}^{y} dy = \int_{t_1}^{t} v_y dt = \int_{t_1}^{t} \left[v_{y_1} + \frac{qV}{md}(t - t_1) \right] dt \qquad \text{(Eq. A-27)}$$

which integrates to:

$$y - y_1 = v_{y_1}(t - t_1) + \frac{qV}{2md}(t^2 - t_1^2) - \frac{qV}{md} t_1 (t - t_1) \qquad \text{(Eq. A-28)}$$

Thus we can now write an expression for the y position at any time, t:

$$y(t) = y_1 + v_{y_1}(t - t_1) + \frac{qV}{2md}(t^2 - t_1^2 - 2t_1 t + 2t_1^2) \qquad \text{(Eq. A-29)}$$

$$= y_1 + v_{y_1}(t - t_1) + \frac{qV}{2md}(t^2 - 2t_1 t + t_1^2)$$

or more concisely:

$$y(t) = y_1 + v_{y_1}(t - t_1) + \frac{qV}{2md}(t - t_1)^2 \qquad \text{(Eq. A-30)}$$

where $V = V_0$ if $t_1 < 0$

$V = V_\tau$ if $t > \tau$

Region III (Post-acceleration)

Once an ion enters the post acceleration region, Region III, it is once again in a field-free environment. Though the calculation of trajectory information is quite similar to that for Region I, it differs greatly in one respect--the y velocity component, though a constant, can no longer be assumed to be zero. Consequently, though Equations A-4 and A-5 continue to apply, the y component of motion must be re-examined.

As stated, ions exiting the parallel plate region have experienced a force parallel to the y-axis and thus they enter Region III with some fixed y velocity component, v_{y_1}. Thus, $v_{y_1} \equiv$ constant. Integrating as before to obtain the y coordinate position as a function of time:

$$\frac{dy}{dt} = v_{y_1} \qquad \text{(Eq. A-31)}$$

and

$$\int_{y_1}^{y} dy = \int_{t_1}^{t} v_{y_1}\, dt = v_{y_1} \int_{t_1}^{t} dt \qquad \text{(Eq. A-32)}$$

which reduces to:

$$y(t) = y_1 + v_{y_1}(t - t_1) \qquad \text{(Eq. A-33)}$$

where y_1 and v_{y_1} are the y displacement and velocity components, respectively, of the ion as it exits the parallel plates. These values must be determined by applying the appropriate equations previously derived for Region II.

Shutter Function

As the ion beam is swept across the slit, the portion of the beam which passes through the slit is a function of the slit size, beam diameter, and beam position. An intensity function based solely on the cross-sectional area of the beam in the plane of the slit opening can be generated if it is assumed the local ion density of the beam is uniform both radially and axially; this is actually a very good assumption even for a pulsed beam apparatus since the requirement for isotropy need only be met for the relatively small segment of the beam which is actually transmitted by the slit.

Four general geometries are possible for a cylindrically symmetric beam swept across a rectangular slit. These four cases are shown schematically in Figure A-3 and their area formulae are derived below.

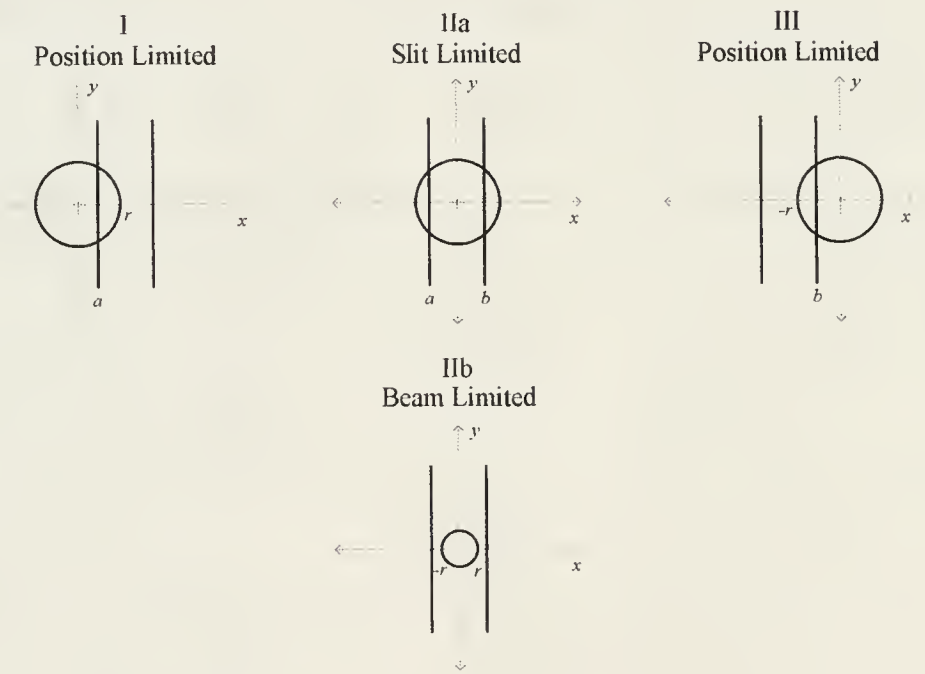

Figure A-3 Generalized diagrams of beam/slit geometries created as the ion beam sweeps from left to right across the slit opening. The slit limited case (IIa) is replaced by the beam limited case (IIb) when the beam diameter is less than or equal to the slit width.

Case I

As the ion beam first begins to move over the slit, the portion of the beam cross-section transmitted by the slit is bounded on the left by the slit edge and on the right by the extent of the beam itself. In order to calculate the area between this chord and arc we will choose the center of the beam as the origin for the coordinate system. Because of the symmetry involved, it will only be necessary to integrate the region above the x-axis and then multiply by two to obtain the total area, A, over the slit. Thus for a beam of radius, r, and the slit edge at $x = a$ we can write:

$$A = 2\int_a^r \left(r^2 - x^2\right)^{1/2} dx \qquad \text{(Eq. A-34)}$$

$$= 2\left(\frac{1}{2}\right)\left[x\left(r^2 - x^2\right)^{1/2} + r^2 \sin^{-1}\frac{x}{|r|}\right]_a^r$$

$$= 2\left(\frac{1}{2}\right)\left[r\left(r^2 - r^2\right)^{1/2} + r^2 \sin^{-1}\frac{r}{|r|} - a\left(r^2 - a^2\right)^{1/2} - r^2 \sin^{-1}\frac{a}{|r|}\right]$$

which simplifies to give the final area formula:

$$A = \left[r^2\left(\frac{\pi}{2}\right) - a\left(r^2 - a^2\right)^{1/2} - r^2 \sin^{-1}\frac{a}{|r|}\right] \qquad \text{(Eq. A-35)}$$

Case IIa

If the beam diameter is greater than the slit width, at some point during the beam sweep the leading edge of the beam cross-section will have passed over the slit while the trailing edge will not yet have entered the slit opening (cf. Figure A-3 (IIa)). When this occurs, the region of interest is now bounded on the left and on the right by the slit edges. This slit limited condition can be evaluated as before, but with different limits of integration. If the left slit boundary is at $x = a$ and the right slit boundary is at $x = b$ then:

$$A = 2\int_{a}^{b} \left(r^2 - x^2\right)^{1/2} dx \qquad \text{(Eq. A-36)}$$

$$= 2\left(\frac{1}{2}\right)\left[b\left(r^2 - b^2\right)^{1/2} + r^2 \sin^{-1}\frac{b}{|r|} - a\left(r^2 - a^2\right)^{1/2} - r^2 \sin^{-1}\frac{a}{|r|}\right]$$

and finally:

$$A = b\left(r^2 - b^2\right)^{1/2} + r^2 \sin^{-1}\frac{b}{|r|} - a\left(r^2 - a^2\right)^{1/2} - r^2 \sin^{-1}\frac{a}{|r|} \qquad \text{(Eq. A-37)}$$

Case IIb

If the beam diameter is less than or equal to the slit width then Case IIa will not occur. Instead, at some point the entire beam cross-section will be within the slit opening. The region of interest is now defined solely by the extent of the beam and:

$$A = 2\int_{-r}^{r} \left(r^2 - x^2\right)^{1/2} dx \qquad \text{(Eq. A-38)}$$

$$= 2\left(\frac{1}{2}\right)\left[r\left(r^2 - r^2\right)^{1/2} + r^2 \sin^{-1}\frac{r}{|r|} + r\left(r^2 - r^2\right)^{1/2} - r^2 \sin^{-1}\frac{-r}{|r|}\right]$$

$$= r^2\left(\frac{\pi}{2}\right) - r^2\left(\frac{-\pi}{2}\right)$$

which reduces to the familiar equation:

$$A = \pi r^2 \qquad \text{(Eq. A-39)}$$

Case III

Once the leading edge of the beam cross-section has moved pass the slit and the trailing edge is within the slit opening, we are once again faced with a geometry very much like that of Case I. In fact, it is the mirror image of Case I; the radius of the beam, r, now defines the left boundary and the slit edge forms the right boundary at $x = b$. Under these conditions:

$$A = 2\int_{-r}^{a} \left(r^2 - x^2\right)^{1/2} dx \qquad \text{(Eq. A-40)}$$

$$= 2\left(\frac{1}{2}\right)\left[b\left(r^2 - b^2\right)^{1/2} + r^2 \sin^{-1}\frac{b}{|r|} - (-r)\left(r^2 - (-r)^2\right)^{1/2} - r^2 \sin^{-1}\frac{-r}{|r|}\right]$$

which reduces to:

$$A = b\left(r^2 - b^2\right)^{1/2} + r^2 \sin^{-1}\frac{b}{|r|} + r^2\left(\frac{\pi}{2}\right) \qquad \text{(Eq. A-41)}$$

1-D Boltzmann Distribution

The final detected TOF pulse shapes is determined not only by the shutter function, but also by the thermal velocity spread within the isomass ion packets. Since in TOF mass spectrometry the arrival time of these packets provides the sole means of mass identification, the only velocity components of interest are those parallel to the flight tube; radial velocity spread is unimportant as long as the beam diameter does not become excessively large. Thus, a one-dimensional thermal velocity distribution added to the beam acceleration velocity will provide a quite accurate description of the on-axis motion of a given isomass packet within a beamlet chopped out of the beam pulse when swept across the slit.

Our approach will be to utilize a discreet one-dimensional Boltzmann velocity distribution, and from it generate population densities over a range of velocity increments. For a sample of N molecules at a temperature T, the x component velocity distribution can be written as:

$$\frac{1}{N}\frac{dN}{dv_x} = \sqrt{\frac{m}{2\pi kT}}e^{-mv_x^2/2kT} \qquad \text{(Eq. A-42)}$$

where k is the Boltzmann constant. The distribution is symmetrical about $v_x = 0$ which is also where dN/Ndv_x reaches a maximum value of $\sqrt{m/2\pi kT}$.

Though the integration of Equation A-42 cannot be expressed in closed form, this presents no real problem since the goal from the outset was to create a discreet Boltzmann distribution. Rewriting Equation A-42 as a discreet function gives:

$$\frac{1}{N}\frac{\Delta N}{\Delta v_x} = \sqrt{\frac{m}{2\pi kT}} e^{-mv_x^2/2kT} \qquad \text{(Eq. A-43)}$$

In order to evaluate this function, we must first choose a finite number of velocities to consider. If the maximum velocity $v_X(max)$ is defined as the positive x-velocity where the fraction $\Delta N / N \Delta v_x$ has fallen to 5% of its maximum value (and by symmetry $v_X(min) = -v_X(max)$), then a histogram can be constructed of i mean velocity bins of width Δv_x whose heights correspond to the fraction of molecules with velocities which fall within the range $\bar{v}_{x_i} \pm \Delta v_x/2$. Thus:

$$\frac{\Delta N_i}{N} = \sqrt{\frac{m}{2\pi kT}} e^{-mv_{x_i}^2/2kt} \Delta v_x \qquad \text{(Eq. A-44)}$$

where

$$\Delta v_x = 2 v_x(\max)/(i-1) \qquad \text{(Eq. A-45)}$$

and

$$v_x(\max) = \sqrt{(-2kT/m)\ln(0.05)} \qquad \text{(Eq. A-46)}$$

APPENDIX B
TRAJION SOURCE CODE

The following computer code was written for Turbo Pascal Version 4.0 as developed by Borland International, 4585 Scotts Valley Drive, Scotts Valley, CA 95066. The program output is directed into three separate text files: 1) "BOLTZMAN.TXT" which contains the Boltzmann velocity distribution based on the beam temperature, 2) "TRAJECT.TXT" which details the two defining trajectories of the user defined isomass ion packet, and 3) "PULSE.TXT" which contains the pulse intensity at the detector as a function of time , i.e. the pulse shape profile. TRAJION does not provide direct graphical output, but does create delimited files which are readily imported into standard graphics packages for display.

```
{$N+}
(* HARDWARE FLOATING POINT SELECTED *)

PROGRAM TRAJION v6;


(* 10 JAN 94 REVISION *)

(* COMPUTES ION TRAJECTORIES THROUGH TOF MS SYSTEM *)
(* ALL COMPUTATIONS PERFORMED WITH THE "MKS" SYSTEM *)
(* WRITES BOLTZMANN VELOCITY DISTRIBUTION TO "BOLTZMAN.TXT" *)
(* WRITES LIMITING ISOMASS PACKET TRAJECTORIES TO "TRAJECT.TXT" *)
(* WRITES BEAM INTENSITIES AS A FUNCTION OF TIME TO "PULSE.TXT" *)


CONST
    XB = 0.0254;              (* LENGTH OF PARALLEL PLATES *)
    XC = 0.2873;              (* DISTANCE BETWEEN PLATES AND SLIT *)
    XD = 1.5145;              (* DISTANCE BETWEEN SLIT AND DETECTOR *)
     D = 0.0254;              (* PLATE SEPARATION *)
     E = 0.003;               (* SLIT WIDTH *)
```

```
    F = 0.01905;              (* DETECTOR DIAMETER *)
  TAU = 2.2E-6;               (* PLATE VOLTAGE DECAY TIME *)
   V0 = 100;                  (* INITIAL PLATE VOLTAGE *)
 VTAU = -100;                 (* FINAL PLATE VOLTAGE *)
   DV = -200;                 (* CHANGE IN PLATE VOLTAGE *)
    Q = 1.6021892E-19;        (* ELEMENTARY CHARGE IN COULOMBS *)
    K = 1.38066E-23;          (* BOLTZMANN CONSTANT IN J/K *)
    N = 101;                  (* NUMBER OF BOLTZMANN VELOCITY BINS &
                                 HISTOGRAM CHANNELS; MUST BE ODD
                                 INTEGER; 10N BEAM SLICES *)

TYPE
  BOLTDIST = (VELOCITY, DENSITY);
  INDEX = 1..N;
  VXARRAY = ARRAY [INDEX, BOLTDIST] OF EXTENDED;

  SLITDIST = (TIME, INTENSITY);
  CHANNEL = 1..N;
  MCARRAY = ARRAY [CHANNEL, SLITDIST] OF EXTENDED;

VAR
  X, Y, VX0, VX, VY, T, DT, M, KE, Y0, X0, TEMP, R, AREA, FIRSTT, LASTT,
    FIRSTX, LASTX , DELTAT, DELTAX : EXTENDED;
  SENTINEL, STATUS : STRING;
  CH, DX, LCV1, LCV2 : INTEGER;
  VXDIST : VXARRAY;
  MCADIST : MCARRAY;
  OUTFILE1, OUTFILE2, OUTFILE3 : TEXT;


PROCEDURE BOLTZMANN (M, KE, VX0, TEMP : EXTENDED;
                     VAR VXDIST : VXARRAY);

(* COMPUTES DISCREET ONE DIMENSIONAL BOLTZMANN DISTRIBUTION *)

VAR
  dN_NdVmax, dN_NdVmin, Vmax, dV : EXTENDED;
  I : INTEGER;

BEGIN
  dN_NdVmax := SQRT (M / (2 * PI * K * TEMP));
  dN_NdVmin := dN_NdVmax / 20;     (* STARTS AT 5% OF MAX INTENSITY *)
  Vmax := SQRT ((- 2 * K * TEMP / M) * LN (dN_NdVmin / dN_NdVmax));
  dV := (Vmax * 2) / (N - 1);
  I := 1;
  WHILE I <= ((N + 1) / 2) DO
    BEGIN
      VXDIST [I, VELOCITY] := Vmax - ((I - 1) * dV);
      VXDIST [(N + 1 - I), VELOCITY] := - VXDIST [I, VELOCITY];
      VXDIST [I, DENSITY] := dV * dN_NdVmax * EXP ((- M / (2 * K *
        TEMP)) * SQR (VXDIST [I, VELOCITY]));
      VXDIST [(N + 1 - I), DENSITY] := VXDIST [I, DENSITY];
      I := I + 1
    END;
```

```
  FOR I := 1 TO N DO
    VXDIST [I, VELOCITY] := VXDIST [I, VELOCITY] + VX0;
  WRITELN (OUTFILE1, 'BIN #' :6, 'VX (M/S)' :16, 'DENSITY' :16);
  WRITELN (OUTFILE1, '=====================================');
  FOR I := 1 TO N DO
    WRITELN (OUTFILE1, I :6, VXDIST [I, VELOCITY] :16:2, VXDIST [I,
      DENSITY] :16:8);
  CLOSE (OUTFILE1)
END;


PROCEDURE PREACCEL (X0, Y0, VX : EXTENDED;
                    SENTINEL : STRING;
                    VAR T, X :EXTENDED);

(* DEFINES LINEAR TRAJECTORY BEFORE ENTERING PLATES *)

BEGIN
  VY := 0;
  Y := Y0;
  IF (SENTINEL = 'FX') OR (SENTINEL = 'LX') THEN
    WRITELN (OUTFILE2, X :15:9, Y :15:9, VY :13:3, T :19:12);
  X := 0;
  T := -(X0 / VX);
  IF (SENTINEL = 'FX') OR (SENTINEL ='LX') THEN
    WRITELN (OUTFILE2, X :15:9, Y :15:9, VY :13:3, T :19:12)
END;
(* RETURNS TO MAIN PROGRAM WITH ION AT X = 0 AND T <= TAU *)


PROCEDURE CONSTACCEL (DX : INTEGER;
                      SENTINEL : STRING;
                      VX, X0, Y0 : EXTENDED;
                      VAR T, X, Y, VY : EXTENDED);

(* CALCULATES LOCI BETWEEN PLATES WHEN T = 0 OR T > TAU *)


VAR
  XI, YTAU, VYTAU : EXTENDED;
  I, J : INTEGER;


BEGIN
  IF (T = TAU) AND (X = 0) THEN    (* FIRST X0 TRAJ ONLY *)
    FOR I := 1 TO DX DO
      BEGIN
        X := I * (XB / DX);
        T := TAU + (X / VX);
        VY := ((VTAU * Q) / (M * D)) * (T - TAU);
        Y := Y0 + ((VTAU * Q) / (2 * M * D)) * (T - TAU) * (T - TAU);
        IF (SENTINEL = 'FX') OR (SENTINEL = 'LX') THEN
          WRITELN (OUTFILE2, X :15:9, Y :15:9, VY :13:3, T :19:12)
      END
```

```
  ELSE IF (T = TAU) AND (X > 0) AND (X < XB) THEN   (* AFTER VARI *)
    BEGIN
      VYTAU := VY;
      YTAU := Y;
      I := 0;
      REPEAT
        I := I + 1;
        XI := I * (XB / DX)
      UNTIL XI > X;
      FOR J := I TO DX DO
        BEGIN
          X := J * (XB / DX);
          T := (X - X0) / VX;
          VY := VYTAU + ((VTAU * Q) / (M * D)) * (T - TAU);
          Y := YTAU + (VYTAU * (T - TAU)) + (((VTAU * Q) / (2 * M * D))
               * (T - TAU) * (T - TAU));
          IF (SENTINEL = 'FX') OR (SENTINEL = 'LX') THEN
            WRITELN (OUTFILE2, X :15:9, Y :15:9, VY :13:3, T :19:12)
        END
    END
END;
(* RETURNS TO MAIN PROGRAM WITH ION AT X = XB *)


PROCEDURE VARIACCEL (DX : INTEGER;
                     SENTINEL : STRING;
                     VX, X0, Y0 : EXTENDED;
                     VAR T, X, Y, VY : EXTENDED);

(* CALCULATES LOCI BETWEEN PLATES WHEN 0 <= T <= TAU *)


VAR
  I : INTEGER;
  T1, TI, XI, T0B, Y0B, VY0B : EXTENDED;


BEGIN
  IF (T < TAU) AND (X = 0) THEN      (* AFTER PRE *)
    BEGIN
      T1 := T;
      TI := XB / (DX * VX);
      T := T + TI;
      I := 1;
      WHILE (T <= TAU) AND (I <= DX) DO
        BEGIN
          X := I * (XB / DX);
          VY := (Q / (M * D)) * ((DV / (2 * TAU)) * ((T * T) - (T1 *
                T1)) + (V0 * (T - T1)));
          Y := Y0 + ((Q * DV) / (6 * M * D * TAU)) * ((T * T * T) - (3 *
               T1 * T1 * T) + (2 * T1 * T1 * T1)) + ((Q * V0) / (2 * M *
               D)) * ((T - T1) * (T - T1));
          IF (SENTINEL = 'FX') OR (SENTINEL = 'LX') THEN
            WRITELN (OUTFILE2, X :15:9, Y :15:9, VY :13:3, T :19:12);
```

```
        I := I + 1;
        T := T + TI
      END;
    IF (T > TAU) AND (I <= DX) THEN      (* CALC BOUNDARY CONDITIONS *)
      BEGIN
        T := TAU;
        X := (VX * TAU) + X0;
        VY := (Q / (M * D)) * ((DV / (2 * TAU)) * ((T * T) - (T1 *
              T1)) + (V0 * (T - T1)));
        Y := Y0 + ((Q * DV) / (6 * M * D * TAU)) * ((T * T * T) - (3 *
             T1 * T1 * T) + (2 * T1 * T1 * T1)) + ((Q * V0) / (2 * M *
             D)) * ((T - T1) * (T - T1));
        IF (SENTINEL = 'FX') OR (SENTINEL = 'LX') THEN
          WRITELN (OUTFILE2, X :15:9, Y :15:9, VY :13:3, T :19:12)
      END
    ELSE
      T := T - TI
  END
ELSE IF (T = 0) AND (X0 >= 0) AND (X0 < XB) THEN      (* CALC INITIAL
  CONDS *)
  BEGIN
    T0B := - X0 / VX;
    VY0B := ((V0 * Q) / (M * D)) * (- T0B);
    Y0B := Y0 + ((V0 * Q) / (2 * M * D)) * (T0B * T0B);
    IF (SENTINEL = 'FX') OR (SENTINEL = 'LX') THEN
      WRITELN (OUTFILE2, X0 :15:9, Y0B :15:9, VY0B :13:3, T :19:12);
    TI := XB / (DX * VX);
    I := 0;
    REPEAT
      I := I + 1;
      XI := I * (XB / DX);
    UNTIL XI >= X0;
    T := (XI - X0) / VX;
    WHILE (T <= TAU) AND (I <= DX) DO
      BEGIN
        X := I * (XB / DX);
        VY := VY0B + (Q / (M * D)) * ((DV / (2 * TAU)) * (T * T) +
              (V0 * T));
        Y := Y0B + (VY0B * T) + ((Q * DV) / (6 * M * D * TAU)) * (T *
             T * T) + ((Q * V0) / (2 * M * D)) * (T * T);
        IF (SENTINEL = 'FX') OR (SENTINEL = 'LX') THEN
          WRITELN (OUTFILE2, X :15:9, Y :15:9, VY :13:3, T :19:12);
        I := I + 1;
        T := T + TI
      END;
      IF (T > TAU) AND (I <= DX) THEN
        BEGIN
          T := TAU;
          X := (VX * T) + X0;
          VY := VY0B + (Q / (M * D)) * ((DV / (2 * TAU)) * (T * T) +
                (V0 * T));
          Y := Y0B + (VY0B * T) + ((Q * DV) /(6 * M * D * TAU)) * (T *
               T * T) + ((Q * V0) / (2 * M * D)) * (T * T);
          IF (SENTINEL = 'FX') OR (SENTINEL = 'LX') THEN
```

```
            WRITELN (OUTFILE2, X :15:9, Y :15:9, VY :13:3, T :19:12)
          END
        ELSE
          T := T - TI
    END
END;
(* RETURNS TO MAIN PROGRAM WITH ION AT X = B AND T <= TAU, OR T = TAU
   AND 0 < X < B *)

PROCEDURE CHOPPER (Y, R : EXTENDED; VAR AREA : EXTENDED;
                   VAR STATUS : STRING); FORWARD;

PROCEDURE POSTACCEL (X, Y, VY, R : EXTENDED;
                     VXDIST : VXARRAY;
                     VAR X0, Y0, VX, T, FIRSTT, LASTX, DELTAT, DELTAX,
                       AREA : EXTENDED;
                     VAR SENTINEL, STATUS : STRING);

(* DEFINES LINEAR TRAJECTORY AFTER EXITING PLATES, TERMINATES
   CALCULATIONS ONCE ION IMPACTS SLIT PLATE OR REACHES END OF FLIGHT
   TUBE, AND DETERMINES SENTINEL VALUE *)

VAR
  T1, Y1, V1 : EXTENDED;

BEGIN
  IF (T = 0) AND (X0 = XB) THEN           (* FINAL X0 TRAJ ONLY *)
    BEGIN
      VY := ((V0 * Q) / (M * D)) * (XB / VX);
      Y := Y0 + ((V0 * Q) / (2 * M * D)) * ((X0 / VX) * (X0 / VX));
      IF (SENTINEL = 'FX') OR (SENTINEL = 'LX') THEN
        WRITELN (OUTFILE2, X :15:9, Y :15:9, VY :13:3, T :19:12)
    END;
  T1 := T;
  Y1 := Y;
  X := XB + XC;
  T := T + (XC / VX);
  Y := Y1 + VY * (T - T1);
  IF (SENTINEL = 'FX') OR (SENTINEL = 'LX') THEN
    WRITELN (OUTFILE2, X :15:9, Y :15:9, VY :13:3, T :19:12);
  IF SENTINEL = 'GREEN' THEN
    BEGIN
      T := T + (XD / VX);
      CHOPPER (Y, R, AREA, STATUS)
    END
  ELSE IF (Y <= (E / 2)) AND (Y >= (-E / 2)) THEN
    BEGIN
      X := XB + XC + XD;
      T := T + (XD / VX);
      Y := Y1 + VY * (T - T1);
      IF SENTINEL = 'RED' THEN
        BEGIN
          SENTINEL := 'LX';
          X0 := X0 - (DT * VX0)
```

```
  END
ELSE IF (SENTINEL = 'FX') OR (SENTINEL = 'LX') THEN
  BEGIN
    WRITELN (OUTFILE2, X :15:9, Y :15:9, VY :13:3, T :19:12);
    WRITELN (OUTFILE2);
    IF SENTINEL = 'FX' THEN
      BEGIN
        DELTAX := (FIRSTX - LASTX) / (10 * N);
        DELTAT := (LASTT - FIRSTT) / N;
        Y0 := 0;
        SENTINEL := 'GREEN'
      END
    ELSE  IF SENTINEL = 'LX' THEN
      BEGIN
        IF Y < (- F / 2) THEN
          WRITELN (OUTFILE2, '   ***** warning: TEDGE of fast
          component missed detector edge *****');
        LASTX := X0;
        X0 := X0 - (DT * VX0);
        Y0 := - R;
        SENTINEL := 'YELLOW1'
      END
  END
ELSE IF SENTINEL = 'YELLOW2' THEN
  BEGIN
    IF Y > (F / 2) THEN
      WRITELN (OUTFILE2, '   ***** warning: LEDGE of fast
      component missed detector edge *****');
    FIRSTT := T;
    FIRSTX := X0;
    VX := VXDIST [N, VELOCITY];
    X0 := LASTX - (DT * VX0);
    Y0 := R;
    SENTINEL := 'YELLOW3'
  END
ELSE IF SENTINEL = 'YELLOW3' THEN
  BEGIN
    IF Y < (- F / 2) THEN
      WRITELN (OUTFILE2, '   ***** warning: TEDGE of slow
      component missed detector edge *****');
    LASTT := T;
    X0 := X0 - (DT * VX0);
    Y0 := -R;
    SENTINEL := 'YELLOW4'
  END
ELSE IF SENTINEL = 'YELLOW5' THEN
  BEGIN
    IF Y > (F / 2) THEN
      WRITELN (OUTFILE2, '   ***** warning: LEDGE of slow
      component missed detector edge *****');
    IF X0 < FIRSTX THEN
      VX := VXDIST [1, VELOCITY]
    ELSE IF X0 >= FIRSTX THEN
      FIRSTX := X0;
```

```
          X0 := FIRSTX - (DT * VX0);
          SENTINEL := 'FX'
        END
    END
  ELSE IF Y > (E / 2) THEN
    BEGIN
      IF SENTINEL = 'YELLOW1' THEN
        BEGIN
          X0 := X0 - (2 * DT * VX0);
          SENTINEL := 'YELLOW2'
        END
      ELSE IF SENTINEL = 'YELLOW4' THEN
        BEGIN
          X0 := X0 - (2 * DT * VX0);
          SENTINEL := 'YELLOW5'
        END
    END
END;
(* RETURNS TO MAIN MENU AFTER COMPLETING TRAJ FOR A GIVEN X0 *)


PROCEDURE CHOPPER (Y, R : EXTENDED;
                   VAR AREA : EXTENDED;
                   VAR STATUS : STRING);

(* COMPUTES CROSS-SECTIONAL AREA OF BEAM PASSED BY SLIT BASED ON BEAM
   DIAMETER, SLIT SIZE AND BEAM SWEEP POSITION *)

VAR
  LEDGE, TEDGE, A, B : EXTENDED;

BEGIN
  LEDGE := Y + R;
  TEDGE := Y - R;
  IF (LEDGE > (- E / 2)) AND (TEDGE < (E / 2)) THEN (* BEAM OVER SLIT *)
    BEGIN
      STATUS := 'GO';
      IF (TEDGE < (- E / 2)) AND (LEDGE <= (E / 2)) THEN
        BEGIN
          A := (- E / 2) - Y;
          AREA := ((PI * R * R) / 2) - (A * SQRT ((R * R) - (A * A))) -
                  (R * R * ARCTAN (A / SQRT ((R * R) - (A * A))))
        END
      ELSE IF (TEDGE >= (- E / 2)) AND (LEDGE <= (E / 2)) THEN
        AREA := PI * R * R
      ELSE IF (TEDGE < (- E / 2)) AND (LEDGE > (E / 2)) THEN
        BEGIN
          A := (- E / 2) - Y;
          B := (E / 2) - Y;
          AREA := B * SQRT ((R * R) - (B * B)) + (R * R * ARCTAN
                  (B / SQRT ((R * R) - (B * B)))) - (A * SQRT ((R * R) -
                  (A * A))) - (R * R * ARCTAN (A / SQRT ((R * R) -
                  (A * A))))
        END
```

```
      ELSE IF (TEDGE >= (- E / 2)) AND (LEDGE > (E / 2)) THEN
        BEGIN
          A := (E / 2) - Y;
          AREA := ((PI * R * R) / 2) + (A * SQRT ((R * R) - (A * A))) +
                  (R * R * ARCTAN (A / SQRT ((R * R) - (A * A))))
        END
    END
END;


BEGIN
(* INITIALIZE VARIABLES *)
  ASSIGN (OUTFILE1, 'BOLTZMAN.TXT');
  REWRITE (OUTFILE1);
  ASSIGN (OUTFILE2, 'TRAJECT.TXT');
  REWRITE (OUTFILE2);
  ASSIGN (OUTFILE3, 'PULSE.TXT');
  REWRITE (OUTFILE3);
  WRITE ('> ENTER ION M/E IN AMU: ');
  READLN (M);
  M := M * 1.6605656E-27;
  WRITE ('> ENTER BEAM KINETIC ENERGY IN EV: ');
  READLN (KE);
  KE := KE * 1.6021892E-19;
  VX0 := SQRT (2 * KE / M);
  WRITE ('> ENTER ESTIMATED BEAM TEMPERATURE IN DEGREES KELVIN: ');
  READLN (TEMP);
  WRITE ('> ENTER BEAM WIDTH IN MM: ');
  READLN (R);
  R := R / 2000;
  WRITE ('> ENTER INTEGRAL NUMBER OF LOCI TO BE CALCULATED BETWEEN
    PLATES: ');
  READLN (DX);
  WRITE ('> ENTER INTEGRAL TIME INTERVAL BETWEEN SUCCESSIVE ION
    TRAJECTORIES IN PS: ');
  READLN (DT);
  DT := DT * 1.0E-12;
  WRITELN (OUTFILE2, 'X (m)' :12, 'Y (m)' :15, 'Vy (m/s)' :16,
    t (s)' :14);
  WRITELN (OUTFILE2, '   ==========================================
    ============');

(* COMPUTE BOLTZMANN VELOCITY DISTRIBUTION *)
  BOLTZMANN (M, KE, VX0, TEMP, VXDIST);

(* ASSIGN VX AND FIRST X0 WHEN HV PULSE IS 1/3 OVER *)
  VX := VXDIST [1, VELOCITY];
  X0 := -VX * 0.66 * TAU;
  Y0 := R;
  X := X0;
  T := 0;
  SENTINEL := 'RED';

(* MAIN PROGRAM *)
```

```
  WHILE (X0 < (XB +(DT * VX))) AND (SENTINEL <> 'GREEN') DO
    BEGIN
      IF X0 < 0 THEN
        BEGIN
          PREACCEL (X0, Y0, VX, SENTINEL, T, X);
          IF T < TAU THEN
            VARIACCEL (DX, SENTINEL, VX, X0, Y0, T, X, Y, VY);
          CONSTACCEL (DX, SENTINEL, VX, X0, Y0, T, X, Y, VY);
          POSTACCEL (X, Y, VY, R, VXDIST, X0, Y0, VX, T, FIRSTT, LASTX,
            DELTAT, DELTAX, AREA, SENTINEL, STATUS)
        END
      ELSE IF (X0 >= 0) AND (X0 < XB) THEN
        BEGIN
          VARIACCEL (DX, SENTINEL, VX, X0, Y0, T, X, Y, VY);
          IF X < XB THEN
            CONSTACCEL (DX, SENTINEL, VX, X0, Y0, T, X, Y, VY);
          POSTACCEL (X, Y, VY, R, VXDIST, X0, Y0, VX, T, FIRSTT, LASTX,
            DELTAT, DELTAX, AREA, SENTINEL, STATUS)
        END
      ELSE IF X0 >= XB THEN
        BEGIN
          X0 := XB;
          X := X0;
          POSTACCEL (X, Y, VY, R, VXDIST, X0, Y0, VX, T, FIRSTT, LASTX,
            DELTAT, DELTAX, AREA, SENTINEL, STATUS)
        END;
      X0 := X0 + (DT * VX0);
      X := X0;
      T := 0
    END;

(* INITIALIZE MCADIST *)
  FOR CH := 1 TO N DO
    BEGIN
      MCADIST [CH, INTENSITY] := 0;
      MCADIST [CH, TIME] := FIRSTT + ((CH - 0.05) * DELTAT)
    END;

(* NESTED FOR LOOP TO CALCULATE AND STORE MCA PULSE SHAPE DATA *)
  FOR LCV1 := 1 TO (10 * N) DO
    BEGIN
      X0 := LASTX + ((LCV1 - 0.5) * DELTAX);
        BEGIN
          FOR LCV2 := 1 TO N DO
            BEGIN
              X := X0;
              T := 0;
              VX := VXDIST [LCV2, VELOCITY];
              STATUS := 'NOGO';
              IF X0 < 0 THEN
                BEGIN
                  PREACCEL (X0, Y0, VX, SENTINEL, T, X);
                  IF T < TAU THEN
                    VARIACCEL (DX, SENTINEL, VX, X0, Y0, T, X, Y, VY);
```

```
                CONSTACCEL (DX, SENTINEL, VX, X0, Y0, T, X, Y, VY);
                POSTACCEL (X, Y, VY, R, VXDIST, X0, Y0, VX, T, FIRSTT,
                  LASTX, DELTAT, DELTAX, AREA, SENTINEL, STATUS)
              END
            ELSE IF (X0 >= 0) AND (X0 < XB) THEN
              BEGIN
                VARIACCEL (DX, SENTINEL, VX, X0, Y0, T, X, Y, VY);
                IF X < XB THEN
                  CONSTACCEL (DX, SENTINEL, VX, X0, Y0, T, X, Y, VY);
                POSTACCEL (X, Y, VY, R, VXDIST, X0, Y0, VX, T, FIRSTT,
                  LASTX, DELTAT, DELTAX, AREA, SENTINEL, STATUS)
              END;
             IF (STATUS = 'GO') THEN
              BEGIN
                CH := TRUNC (((T - FIRSTT) / DELTAT) + 1);
                MCADIST [CH, INTENSITY] := (MCADIST [CH, INTENSITY])
                  + (VXDIST [LCV2, DENSITY] * AREA * DELTAX)
              END
          END
        END
    END;
WRITELN (OUTFILE3, 'CH#' :6, 'TIME (PS)' :12, 'INTENSITY' :12);
FOR CH := 1 TO N DO
  WRITELN (OUTFILE3, CH :6, MCADIST [CH, TIME] * 1E12 :12:0,
    MCADIST [CH, INTENSITY] :12);
CLOSE (OUTFILE3);

(* WRITE JOB/FILE DESCRIPTION *)
    WRITELN (OUTFILE2);
    WRITELN (OUTFILE2, M / 1.6605656E-27 :11:0,' amu', KE / 1.6021892
      E-19 :12:0,' eV', R * 2E3 :10:0,' mm', VX0 :15:0,' m/s');
    WRITELN (OUTFILE2);
    WRITELN (OUTFILE2, 'SLIT = ':16, E * 1000 :2:1,' mm' , 'FIRSTT ='
      :23, FIRSTT * 1E12 :12:0, ' ps');
    WRITELN (OUTFILE2, 'DECAY TIME = ':22, TAU * 1E9 :4:0,' ns',
      'LAASTT = ' :15, LASTT * 1E12 :12:0, ' ps');
    CLOSE (OUTFILE2);
END.
```

APPENDIX C
TRAJION OUTPUT DATA

The following tables and figures were created from data generated by the ion trajectory simulation code TRAJION. The actual TRAJION outputs were imported into Quattro Pro for Windows to create the tables, trajectory plots, and histograms.

Tables C-1 through C-14 as well as Figures C-1 through C-14 were generated for monoenergetic ion beams; the trajectory data simulate the beam axis or centerline motion through the beam deflection TOF mass spectrometer. The effect of a relatively slow (t_r = 2200 ns) deflection plate voltage change versus a fast (t_r = 30 ns) voltage change on a 550 eV ion beam over the mass range of 1 to 10^6 amu was investigated. All code parameters were defined in accordance with the actual experimental parameters. TRAJION v4, an earlier version which does not compute pulse shapes nor address isomass beam velocity spread, was used for this study. Note: TRAJION v6 yields essentially the same results if run for a beam of zero diameter and exceedingly low temperature (ca. 10^{-6} K or less).

Figures C-15 through C-17 illustrate the effects of slit size and beam deflection rise time on the pulse width (or resolution). Each run was based on a CO_2^+ beam at 550 eV with a beam temperature of 10 K and beam diameter of 1 mm. The "no slit" condition was simulated by setting XC = 1.766875, XD = 0.034925, and E = 0.01905, thus allowing the end of the flight tube to define the "slit."

Table C-1 Data for 1 m/e ion trajectories (tr = 2200 ns)

x (m)	y (m)	Vy (m/s)	t (s)
-0.365547339	0	0	0
0	0	0	1.122066E-06
0.0015875	-9.7E-08	-41.232	1.126939E-06
0.003175	-4.15E-07	-90.663	1.131812E-06
0.0047625	-9.94E-07	-148.294	1.136685E-06
0.00635	-1.874E-06	-214.126	1.141558E-06
0.0079375	-3.094E-06	-288.157	1.146431E-06
0.009525	-4.695E-06	-370.388	1.151303E-06
0.0111125	-6.717E-06	-460.819	1.156176E-06
0.0127	-9.2E-06	-559.449	1.161049E-06
0.0142875	-1.2183E-05	-666.28	1.165922E-06
0.015875	-1.5707E-05	-781.311	1.170795E-06
0.0174625	-1.9811E-05	-904.541	1.175668E-06
0.01905	-2.4535E-05	-1035.972	1.180541E-06
0.0206375	-2.992E-05	-1175.602	1.185414E-06
0.022225	-3.6006E-05	-1323.432	1.190287E-06
0.0238125	-4.2832E-05	-1479.462	1.19516E-06
0.0254	-5.0438E-05	-1643.692	1.200033E-06
0.3127	-0.00149998	-1643.692	2.081914E-06
1.8272	-0.009141232	-1643.692	6.730749E-06
-0.326128212	0	0	0
0	0	0	1.001067E-06
0.0015875	3.99E-07	162.38	1.00594E-06
0.003175	1.569E-06	316.559	1.010813E-06
0.0047625	3.471E-06	462.539	1.015686E-06
0.00635	6.064E-06	600.319	1.020559E-06
0.0079375	9.308E-06	729.899	1.025432E-06
0.009525	1.3164E-05	851.28	1.030304E-06
0.0111125	1.7591E-05	964.46	1.035177E-06
0.0127	2.255E-05	1069.44	1.04005E-06
0.0142875	2.8E-05	1166.221	1.044923E-06
0.015875	3.3902E-05	1254.801	1.049796E-06
0.0174625	4.0216E-05	1335.182	1.054669E-06
0.01905	4.6902E-05	1407.363	1.059542E-06
0.0206375	5.3919E-05	1471.344	1.064415E-06
0.022225	6.1228E-05	1527.125	1.069288E-06
0.0238125	6.8789E-05	1574.706	1.074161E-06
0.0254	7.6561E-05	1614.087	1.079034E-06
0.3127	0.001499995	1614.087	1.960915E-06
1.8272	0.009003618	1614.087	6.60975E-06
1	550	0	325781

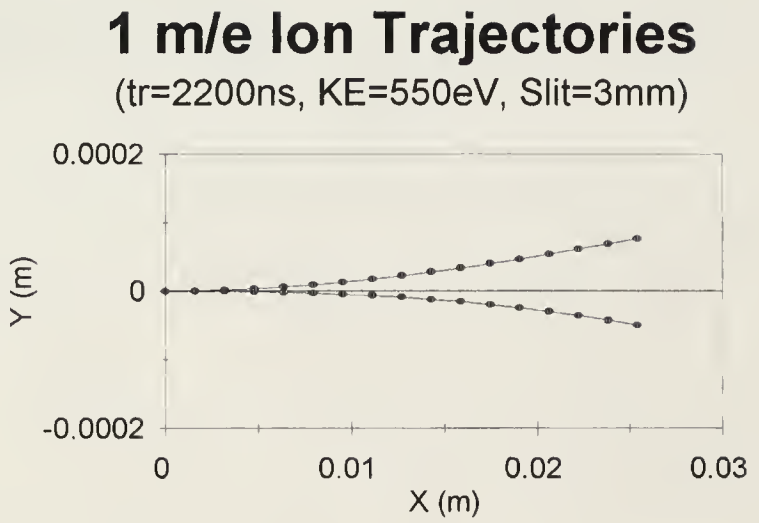

Figure C-1 Plot of 1 m/e beam centerline trajectories between the parallel plates.

Table C-2 Data for 10 m/e ion trajectories (tr = 2200 ns)

x (m)	y (m)	Vy (m/s)	t (s)
-0.107034875	0	0	0
0	0	0	1.038963E-06
0.0015875	2.29E-07	28.38	1.054372E-06
0.003175	8.33E-07	48.56	1.069782E-06
0.0047625	1.684E-06	60.54	1.085191E-06
0.00635	2.656E-06	64.32	1.100601E-06
0.0079375	3.624E-06	59.9	1.11601E-06
0.009525	4.46E-06	47.281	1.13142E-06
0.0111125	5.039E-06	26.461	1.146829E-06
0.0127	5.234E-06	-2.558	1.162239E-06
0.0142875	4.918E-06	-39.778	1.177648E-06
0.015875	3.965E-06	-85.197	1.193058E-06
0.0174625	2.25E-06	-138.816	1.208467E-06
0.01905	-3.55E-07	-200.635	1.223877E-06
0.0206375	-3.975E-06	-270.654	1.239286E-06
0.022225	-8.738E-06	-348.873	1.254696E-06
0.0238125	-1.4769E-05	-435.292	1.270105E-06
0.0254	-2.2196E-05	-529.91	1.285515E-06
0.3127	-0.001499986	-529.91	4.07427E-06
1.8272	-0.009290147	-529.91	1.8775175E-05
-0.094569452	0	0	0
0	0	0	9.17964E-07
0.0015875	7.25E-07	92.767	9.33373E-07
0.003175	2.817E-06	177.335	9.48783E-07
0.0047625	6.148E-06	253.702	9.64192E-07
0.00635	1.0594E-05	321.87	9.79602E-07
0.0079375	1.6026E-05	381.838	9.95011E-07
0.009525	2.2319E-05	433.606	1.010421E-06
0.0111125	2.9347E-05	477.174	1.02583E-06
0.0127	3.6983E-05	512.542	1.04124E-06
0.0142875	4.5101E-05	539.71	1.056649E-06
0.015875	5.3574E-05	558.678	1.072059E-06
0.0174625	6.2277E-05	569.446	1.087468E-06
0.01905	7.1082E-05	572.015	1.102878E-06
0.0206375	7.9864E-05	566.384	1.118287E-06
0.022225	8.8495E-05	552.552	1.133697E-06
0.0238125	9.6851E-05	530.521	1.149106E-06
0.0254	0.000104803	500.29	1.164516E-06
0.3127	0.001499989	500.29	3.953271E-06
1.8272	0.008854703	500.29	1.8654176E-05
10	550	0	103021

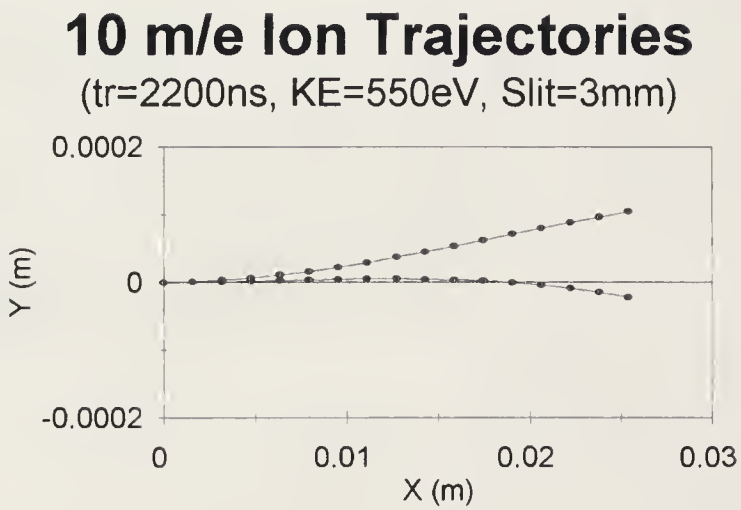

Figure C-2 Plot of 10 m/e beam centerline trajectories between the parallel plates.

Table C-3 Data for 100 m/e ion trajectories (tr = 2200 ns)

x (m)	y (m)	Vy (m/s)	t (s)
-0.025286048	0	0	0
0	0	0	7.76168E-07
0.0015875	1.261E-06	50.393	8.24897E-07
0.003175	4.778E-06	92.586	8.73626E-07
0.0047625	1.0151E-05	126.579	9.22355E-07
0.00635	1.6981E-05	152.372	9.71084E-07
0.0079375	2.4868E-05	169.966	1.019814E-06
0.009525	3.3412E-05	179.359	1.068543E-06
0.0111125	4.2215E-05	180.553	1.117272E-06
0.0127	5.0875E-05	173.546	1.166001E-06
0.0142875	5.8995E-05	158.34	1.21473E-06
0.015875	6.6174E-05	134.934	1.263459E-06
0.0174625	7.2012E-05	103.328	1.312188E-06
0.01905	7.6111E-05	63.522	1.360917E-06
0.0206375	7.807E-05	15.516	1.409646E-06
0.022225	7.749E-05	-40.69	1.458376E-06
0.0238125	7.3971E-05	-105.095	1.507105E-06
0.0254	6.7114E-05	-177.701	1.555834E-06
0.3127	-0.001499998	-177.701	1.0374652E-05
1.8272	-0.009761021	-177.701	5.6862994E-05
-0.021344135	0	0	0
0	0	0	6.55169E-07
0.0015875	1.757E-06	70.754	7.03898E-07
0.003175	6.762E-06	133.308	7.52627E-07
0.0047625	1.4616E-05	187.662	8.01356E-07
0.00635	2.4918E-05	233.817	8.50085E-07
0.0079375	3.727E-05	271.771	8.98815E-07
0.009525	5.1272E-05	301.526	9.47544E-07
0.0111125	6.6523E-05	323.08	9.96273E-07
0.0127	8.2625E-05	336.435	1.045002E-06
0.0142875	9.9178E-05	341.59	1.093731E-06
0.015875	0.000115783	338.545	1.14246E-06
0.0174625	0.000132039	327.3	1.191189E-06
0.01905	0.000147548	307.855	1.239918E-06
0.0206375	0.000161909	280.211	1.288647E-06
0.022225	0.000174723	244.366	1.337377E-06
0.0238125	0.000185591	200.321	1.386106E-06
0.0254	0.000194113	148.077	1.434835E-06
0.3127	0.001499977	148.077	1.0253653E-05
1.8272	0.008383829	148.077	5.6741995E-05
100	550	0	32578

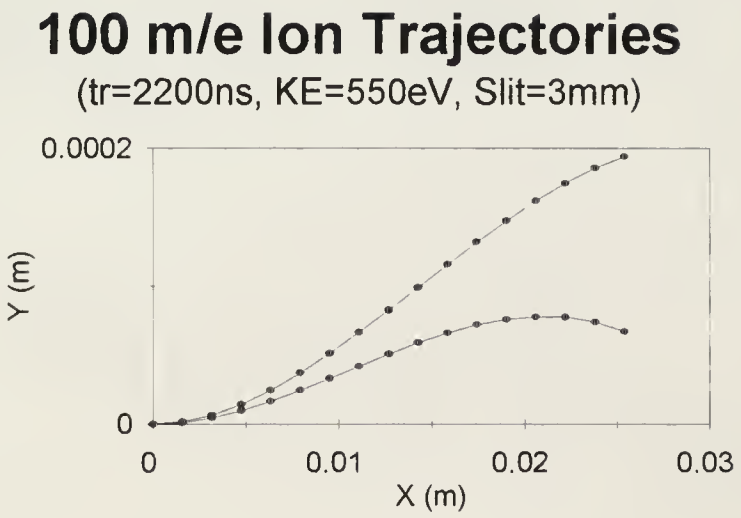

Figure C-3 Plot of 100 m/e beam centerline trajectories between the parallel plates.

Table C-4 Data for 1K m/e ion trajectories (tr = 2200 ns)

x (m)	y (m)	Vy (m/s)	t (s)
0.000473072	4E-07	17.443	0
0.0015875	4.437E-06	56.514	1.08175E-07
0.003175	1.7001E-05	105.192	2.6227E-07
0.0047625	3.6435E-05	145.671	4.16365E-07
0.00635	6.1475E-05	177.949	5.7046E-07
0.0079375	9.0856E-05	202.028	7.24555E-07
0.009525	0.000123316	217.907	8.7865E-07
0.0111125	0.000157592	225.585	1.032745E-06
0.0127	0.000192418	225.064	1.18684E-06
0.0142875	0.000226533	216.343	1.340935E-06
0.015875	0.000258672	199.422	1.49503E-06
0.0174625	0.000287572	174.302	1.649125E-06
0.01905	0.000311969	140.981	1.80322E-06
0.0206375	0.0003306	99.46	1.957315E-06
0.022225	0.0003422	49.74	2.11141E-06
0.023137664	0.000345196	17.443	2.2E-06
0.0238125	0.000345524	-7.439	2.265505E-06
0.0254	0.000339868	-65.974	2.4196E-06
0.3127	-0.001499988	-65.974	3.0307152E-05
1.8272	-0.011198774	-65.974	0.000177316196
0.001869149	6.252E-06	68.92	0
0.003175	1.7923E-05	114.295	1.26756E-07
0.0047625	3.9314E-05	161.985	2.80851E-07
0.00635	6.7423E-05	201.474	4.34946E-07
0.0079375	0.000100986	232.764	5.89041E-07
0.009525	0.000138738	255.854	7.43136E-07
0.0111125	0.000179416	270.744	8.97231E-07
0.0127	0.000221757	277.434	1.051326E-06
0.0142875	0.000264497	275.924	1.205421E-06
0.015875	0.000306373	266.214	1.359516E-06
0.0174625	0.00034612	248.305	1.513611E-06
0.01905	0.000382477	222.195	1.667706E-06
0.0206375	0.000414178	187.886	1.821801E-06
0.022225	0.00043996	145.376	1.975896E-06
0.0238125	0.00045856	94.667	2.129991E-06
0.024533741	0.000464296	68.92	2.2E-06
0.0254	0.000468748	36.979	2.284086E-06
0.3127	0.001499995	36.979	3.0171638E-05
1.8272	0.006936203	36.979	0.000177180682
1000	550	0	10302

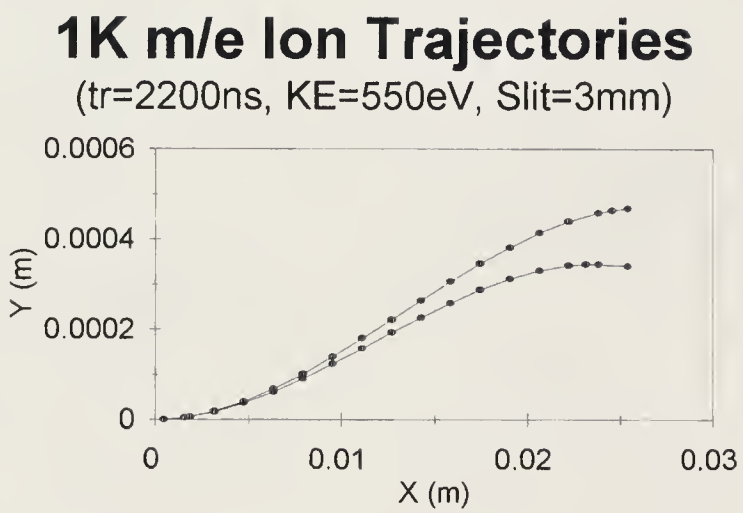

Figure C-4 Plot of 1K m/e beam centerline trajectories between the parallel plates.

Table C-5 Data for 10K m/e ion trajectories (tr = 2200 ns)

x (m)	y (m)	Vy (m/s)	t (s)
0.008157765	0.000119093	95.12	0
0.009525	0.000161933	108.02	4.1968E-07
0.0111125	0.000216693	115.369	9.06971E-07
0.0127	0.000273037	114.517	1.394262E-06
0.0142875	0.000326967	105.465	1.881553E-06
0.015324938	0.000358998	95.12	2.2E-06
0.015875	0.000374517	88.706	2.368844E-06
0.0174625	0.000413233	70.196	2.856135E-06
0.01905	0.000442928	51.685	3.343427E-06
0.0206375	0.000463604	33.175	3.830718E-06
0.022225	0.00047526	14.665	4.318009E-06
0.0238125	0.000477896	-3.845	4.8053E-06
0.0254	0.000471513	-22.356	5.292591E-06
0.3127	-0.001499996	-22.356	9.3480776E-05
1.8272	-0.011892792	-22.356	0.000558364192
0.009553549	0.000163333	111.394	0
0.0111125	0.000220357	125.618	4.78528E-07
0.0127	0.000283451	131.976	9.65819E-07
0.0142875	0.000347646	130.134	1.45311E-06
0.015875	0.000408945	120.092	1.940401E-06
0.016720722	0.000439043	111.394	2.2E-06
0.0174625	0.000463422	102.745	2.427692E-06
0.01905	0.000508978	84.235	2.914984E-06
0.0206375	0.000545516	65.725	3.402275E-06
0.022225	0.000573033	47.215	3.889566E-06
0.0238125	0.00059153	28.704	4.376857E-06
0.0254	0.000601007	10.194	4.864148E-06
0.3127	0.001499998	10.194	9.3052333E-05
1.8272	0.006239022	10.194	0.000557935749
10000	550	0	3258

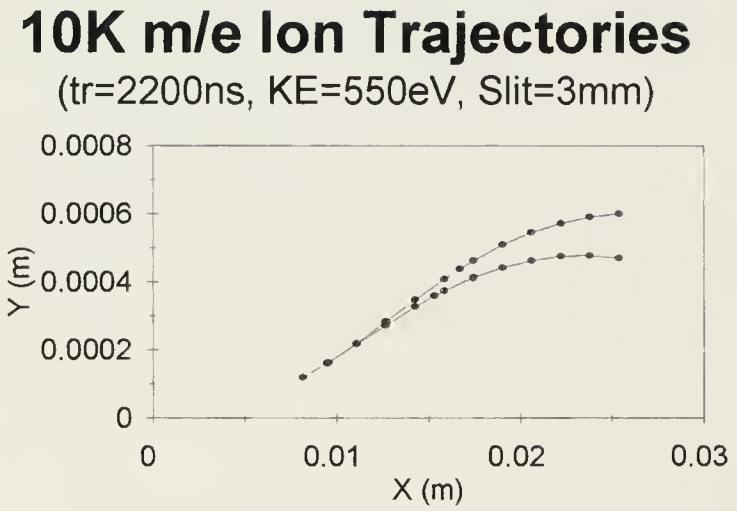

Figure C-5 Plot of 10K m/e beam centerline trajectories between the parallel plates.

Table C-6 Data for 100K m/e ion trajectories (tr = 2200 ns)

x (m)	y (m)	Vy (m/s)	t (s)
0.01060172	0.000201139	39.091	0
0.0111125	0.000220917	40.55	4.95802E-07
0.0127	0.000283773	39.665	2.036752E-06
0.01286818	0.000290203	39.091	2.2E-06
0.0142875	0.000340454	33.858	3.577702E-06
0.015875	0.000388116	28.004	5.118652E-06
0.0174625	0.000426759	22.151	6.659602E-06
0.01905	0.000456382	16.297	8.200551E-06
0.0206375	0.000476985	10.444	9.741501E-06
0.022225	0.000488569	4.59	1.1282451E-05
0.0238125	0.000491132	-1.263	1.2823401E-05
0.0254	0.000484676	-7.117	1.4364351E-05
0.3127	-0.001499998	-7.117	0.000293239877
1.8272	-0.01196219	-7.117	0.001763330317
0.011997476	0.000257587	44.237	0
0.0127	0.000288454	46.025	6.81924E-07
0.014263935	0.000357973	44.237	2.2E-06
0.0142875	0.000358984	44.15	2.222874E-06
0.015875	0.000422507	38.297	3.763824E-06
0.0174625	0.000477011	32.444	5.304774E-06
0.01905	0.000522495	26.59	6.845723E-06
0.0206375	0.000558959	20.737	8.386673E-06
0.022225	0.000586403	14.883	9.927623E-06
0.0238125	0.000604827	9.03	1.1468573E-05
0.0254	0.000614232	3.176	1.3009523E-05
0.3127	0.001499999	3.176	0.000291885049
1.8272	0.006169317	3.176	0.001761975489
100000	550	0	1030

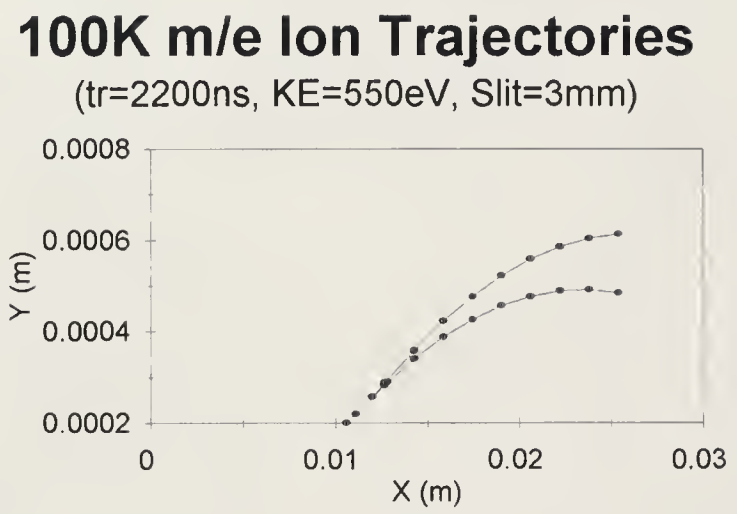

Figure C-6 Plot of 100K m/e beam centerline trajectories between the parallel plates.

Table C-7 Data for 1M m/e ion trajectories (tr = 2200 ns)

x (m)	y (m)	Vy (m/s)	t (s)
0.011375952	0.00023159	13.264	0
0.01209267	0.000261078	13.264	2.2E-06
0.0127	0.000285145	12.556	4.064231E-06
0.0142875	0.000341821	10.705	8.937142E-06
0.015875	0.000389476	8.854	1.3810053E-05
0.0174625	0.000428112	7.003	1.8682965E-05
0.01905	0.000457728	5.152	2.3555876E-05
0.0206375	0.000478324	3.301	2.8428787E-05
0.022225	0.0004899	1.45	3.3301699E-05
0.0238125	0.000492456	-0.401	3.817461E-05
0.0254	0.000485992	-2.252	4.3047521E-05
0.3127	-0.001499995	-2.252	0.000924929366
1.8272	-0.011969113	-2.252	0.005573763525
0.012771704	0.000291905	14.892	0
0.013488421	0.000324973	14.892	2.2E-06
0.0142875	0.000360357	13.96	4.652812E-06
0.015875	0.000423874	12.109	9.525723E-06
0.0174625	0.00047837	10.258	1.4398635E-05
0.01905	0.000523847	8.407	1.9271546E-05
0.0206375	0.000560303	6.556	2.4144457E-05
0.022225	0.00058774	4.705	2.9017369E-05
0.0238125	0.000606157	2.854	3.389028E-05
0.0254	0.000615554	1.003	3.8763191E-05
0.3127	0.0015	1.003	0.000920645036
1.8272	0.006162348	1.003	0.005569479195
1000000	550	0	326

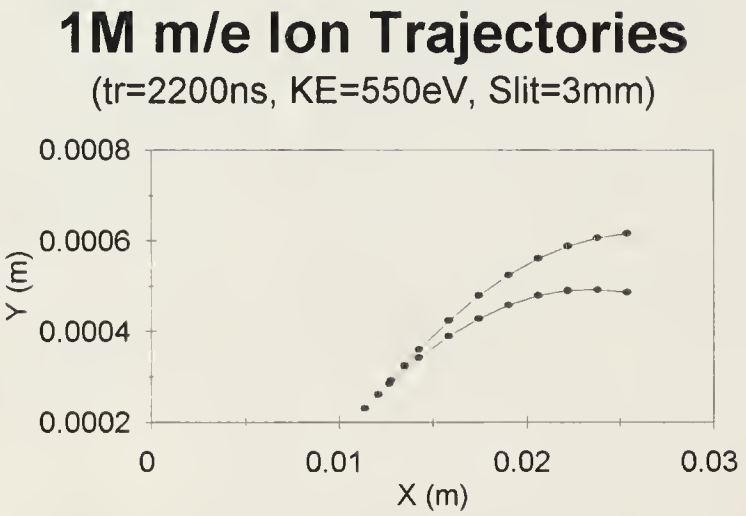

Figure C-7 Plot of 1M m/e beam centerline trajectories between the parallel plates.

Table C-8 Data for 1 m/e ion trajectories (tr = 30 ns)

x (m)	y (m)	Vy (m/s)	t (s)
0.00686094	8.4239E-05	7999.86	0
0.0079375	0.000112596	9116.86	3.305E-09
0.009525	0.00016005	10259.436	8.177E-09
0.0111125	0.000211606	10800.685	1.305E-08
0.0127	0.000264335	10740.609	1.7923E-08
0.0142875	0.000315306	10079.207	2.2796E-08
0.015875	0.000361588	8816.479	2.7669E-08
0.016634358	0.000381213	7999.86	3E-08
0.0174625	0.000400322	7034.246	3.2542E-08
0.01905	0.000430089	5183.22	3.7415E-08
0.0206375	0.000450837	3332.194	4.2288E-08
0.022225	0.000462564	1481.167	4.7161E-08
0.0238125	0.000465272	-369.859	5.2034E-08
0.0254	0.00045896	-2220.885	5.6907E-08
0.3127	-0.001499598	-2220.885	9.38788E-07
1.8272	-0.011824124	-2220.885	5.587623E-06
0.008256258	0.000121986	9626.803	0
0.009525	0.000162109	10914.114	3.894E-09
0.0111125	0.000218143	11983.893	8.767E-09
0.0127	0.000277925	12452.346	1.364E-08
0.0142875	0.000338524	12319.474	1.8513E-08
0.015875	0.000397011	11585.276	2.3386E-08
0.0174625	0.000450456	10249.752	2.8259E-08
0.018029676	0.000467769	9626.803	3E-08
0.01905	0.000496057	8437.104	3.3132E-08
0.0206375	0.00053266	6586.078	3.8005E-08
0.022225	0.000560243	4735.052	4.2878E-08
0.0238125	0.000578807	2884.026	4.7751E-08
0.0254	0.000588351	1032.999	5.2624E-08
0.3127	0.001499334	1032.999	9.34505E-07
1.8272	0.006301577	1032.999	5.58334E-06
1	550	0	325781

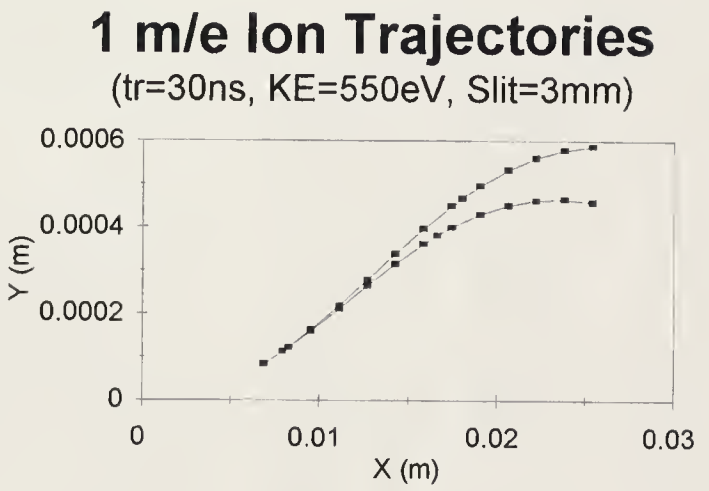

Figure C-8 Plot of 1 m/e beam centerline trajectories between the parallel plates.

Table C-9 Data for 10 m/e ion trajectories (tr = 30 ns)

x (m)	y (m)	Vy (m/s)	t (s)
0.01019031	0.000185831	3757.389	0
0.0111125	0.000220684	3995.961	8.951E-09
0.0127	0.000282534	3931.33	2.4361E-08
0.013280936	0.000304251	3757.389	3E-08
0.0142875	0.000339149	3386.247	3.977E-08
0.015875	0.00038682	2800.901	5.518E-08
0.0174625	0.00042547	2215.555	7.0589E-08
0.01905	0.000455101	1630.21	8.5999E-08
0.0206375	0.000475711	1044.864	1.01408E-07
0.022225	0.000487302	459.518	1.16818E-07
0.0238125	0.000489873	-125.828	1.32227E-07
0.0254	0.000483424	-711.174	1.47637E-07
0.3127	-0.001499865	-711.174	2.936392E-06
1.8272	-0.011954765	-711.174	1.7637297E-05
0.011585933	0.000240218	4271.986	0
0.0127	0.000288103	4534.694	1.0814E-08
0.0142875	0.000357694	4397.382	2.6223E-08
0.01467656	0.000374076	4271.986	3E-08
0.015875	0.000421201	3830.095	4.1633E-08
0.0174625	0.000475711	3244.749	5.7042E-08
0.01905	0.000521201	2659.403	7.2452E-08
0.0206375	0.000557671	2074.058	8.7861E-08
0.022225	0.000585122	1488.712	1.03271E-07
0.0238125	0.000603552	903.366	1.1868E-07
0.0254	0.000612962	318.02	1.3409E-07
0.3127	0.001499842	318.02	2.922845E-06
1.8272	0.006175023	318.02	1.762375E-05
10	550	0	103021

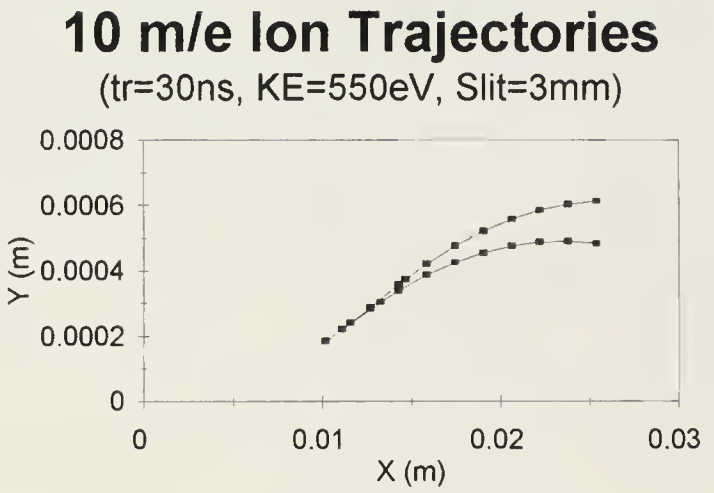

Figure C-9 Plot of 10 m/e beam centerline trajectories between the parallel plates.

Table C-10 Data for 100 m/e ion trajectories (tr = 30 ns)

x (m)	y (m)	Vy (m/s)	t (s)
0.011245718	0.000226317	1311.252	0
0.01222306	0.000266225	1311.252	3E-08
0.0127	0.000285014	1255.64	4.464E-08
0.0142875	0.000341691	1070.538	9.3369E-08
0.015875	0.000389347	885.435	1.42098E-07
0.0174625	0.000427984	700.333	1.90827E-07
0.01905	0.0004576	515.23	2.39556E-07
0.0206375	0.000478197	330.127	2.88285E-07
0.022225	0.000489774	145.025	3.37015E-07
0.0238125	0.000492331	-40.078	3.85744E-07
0.0254	0.000485868	-225.181	4.34473E-07
0.3127	-0.001499959	-225.181	9.253291E-06
1.8272	-0.011968229	-225.181	5.5741633E-05
0.012641428	0.00028598	1473.991	0
0.0127	0.000288636	1480.412	1.798E-09
0.013618769	0.00033077	1473.991	3E-08
0.0142875	0.000360226	1396.017	5.0527E-08
0.015875	0.000423743	1210.915	9.9256E-08
0.0174625	0.00047824	1025.812	1.47985E-07
0.01905	0.000523717	840.71	1.96714E-07
0.0206375	0.000560174	655.607	2.45443E-07
0.022225	0.000587611	470.504	2.94173E-07
0.0238125	0.000606028	285.402	3.42902E-07
0.0254	0.000615426	100.299	3.91631E-07
0.3127	0.001499945	100.299	9.210449E-06
1.8272	0.006162681	100.299	5.5698791E-05
100	550	0	32578

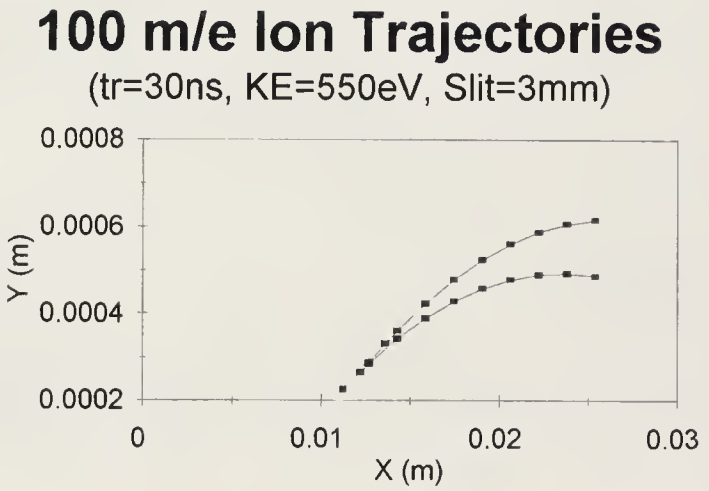

Figure C-10 Plot of 100 m/e beam centerline trajectories between the parallel plates.

Table C-11 Data for 1K m/e ion trajectories (tr = 30 ns)

x (m)	y (m)	Vy (m/s)	t (s)
0.011579721	0.00023[illegible]61	426.97	0
0.011888784	0.00025[illegible]827	426.97	[illegible]E-08
0.0127	0.00023527	397.058	1.0874[illegible]E-07
0.0142875	0.000341945	338.524	2.62838E-07
0.015875	0.000389599	279.989	4.16933E-07
0.0174625	0.000428234	221.455	5.71028E-07
0.01905	0.000457849	162.92	7.25123E-07
0.0206375	0.000478445	104.385	8.79218E-07
0.022225	0.00049002	45.851	1.033313E-06
0.0238125	0.000492575	-12.684	1.187408E-06
0.0254	0.000486111	-71.218	1.341503E-06
0.3127	-0.001499997	-71.218	2.9229055E-05
1.8272	-0.01196975	-71.218	0.000176238099
0.012975469	0.000301293	478.434	0
0.013284531	0.000315703	478.434	3E-08
0.0142875	0.000360482	441.452	1.27356E-07
0.015875	0.000423997	382.918	2.81451E-07
0.0174625	0.000478493	324.383	4.35546E-07
0.01905	0.000523969	265.848	5.89641E-07
0.0206375	0.000560425	207.314	7.43736E-07
0.022225	0.000587861	148.779	8.97831E-07
0.0238125	0.000606277	90.245	1.051926E-06
0.0254	0.000615673	31.71	1.206021E-06
0.3127	0.00149999	31.71	2.9093573E-05
1.8272	0.006161656	31.71	0.000176102617
1000	550	0	10302

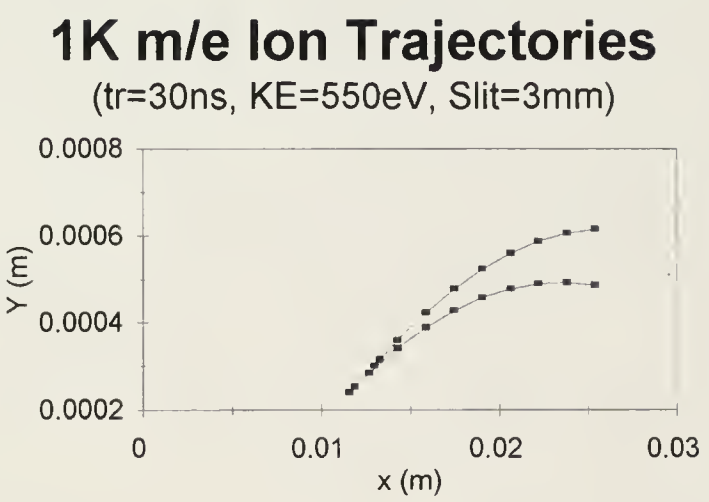

Figure C-11 Plot of 1K m/e beam centerline trajectories between the parallel plates.

Table C-12 Data for 10K m/e ion trajectories (tr = 30 ns)

x (m)	y (m)	Vy (m/s)	t (s)
0.011685372	0.000244359	136.252	0
0.011783107	0.000248452	136.252	3E-08
0.0127	0.000285295	125.561	3.11445E-07
0.0142875	0.00034197	107.05	7.98736E-07
0.015875	0.000389625	88.54	1.286027E-06
0.0174625	0.000428259	70.03	1.773318E-06
0.01905	0.000457874	51.519	2.26061E-06
0.0206375	0.000478469	33.009	2.747901E-06
0.022225	0.000490045	14.499	3.235192E-06
0.0238125	0.0004926	-4.011	3.722483E-06
0.0254	0.000486135	-22.522	4.209774E-06
0.3127	-0.001499999	-22.522	9.2397959E-05
1.8272	-0.011969895	-22.522	0.000557281375
0.013081124	0.00030622	152.526	0
0.013178858	0.000310802	152.526	3E-08
0.0142875	0.000360507	139.599	3.70303E-07
0.015875	0.000424023	121.089	8.57594E-07
0.0174625	0.000478518	102.579	1.344885E-06
0.01905	0.000523994	84.068	1.832177E-06
0.0206375	0.00056045	65.558	2.319468E-06
0.022225	0.000587886	47.048	2.806759E-06
0.0238125	0.000606302	28.538	3.29405E-06
0.0254	0.000615698	10.027	3.781341E-06
0.3127	0.001499996	10.027	9.1969526E-05
1.8272	0.006161567	10.027	0.000556852942
10000	550	0	3258

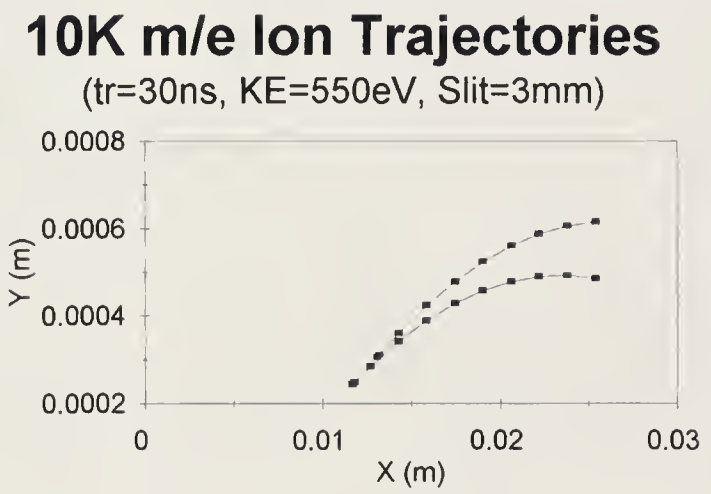

Figure C-12 Plot of 10K m/e beam centerline trajectories between the parallel plates.

Table C-13 Data for 100K m/e ion trajectories (tr = 30 ns)

x (m)	y (m)	Vy (m/s)	t (s)
0.011718785	0.000245759	43.21	0
0.011749691	0.000247055	43.21	3E-08
0.0127	0.000285298	39.706	9.52443E-07
0.0142875	0.000341972	33.852	2.493393E-06
0.015875	0.000389627	27.999	4.034343E-06
0.0174625	0.000428262	22.145	5.575293E-06
0.01905	0.000457877	16.292	7.116242E-06
0.0206375	0.000478472	10.438	8.657192E-06
0.022225	0.000490047	4.585	1.0198142E-05
0.0238125	0.000492602	-1.268	1.1739092E-05
0.0254	0.000486138	-7.122	1.3280042E-05
0.3127	-0.0015	-7.122	0.000292155568
1.8272	-0.011969909	-7.122	0.001762246008
0.013114538	0.000307786	48.356	0
0.013145444	0.000309238	48.356	3E-08
0.0142875	0.00036051	44.145	1.138568E-06
0.015875	0.000424025	38.292	2.679518E-06
0.0174625	0.000478521	32.438	4.220468E-06
0.01905	0.000523997	26.585	5.761417E-06
0.0206375	0.000560452	20.731	7.302367E-06
0.022225	0.000587888	14.878	8.843317E-06
0.0238125	0.000606305	9.024	1.0384267E-05
0.0254	0.000615701	3.171	1.1925217E-05
0.3127	0.001499998	3.171	0.000290800743
1.8272	0.006161564	3.171	0.001760891183
100000	550	0	1030

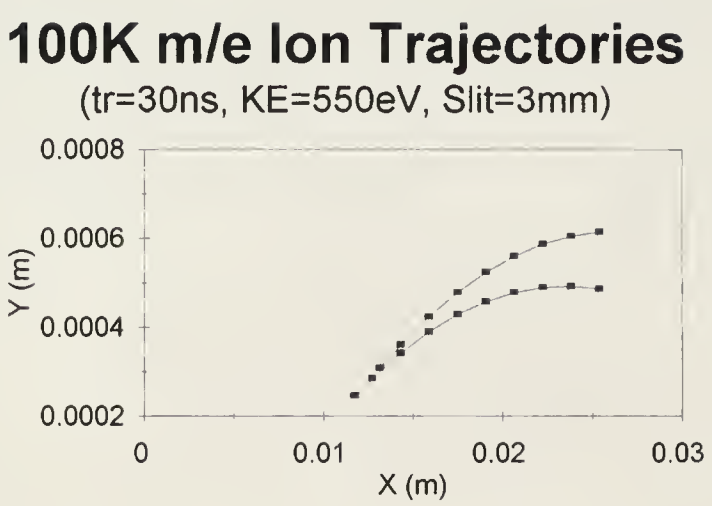

Figure C-13 Plot of 100K m/e beam centerline trajectories between the parallel plates.

Table C-14 Data for 1M m/e ion trajectories (tr = 30 ns)

x (m)	y (m)	Vy (m/s)	t (s)
0.011729353	0.000246202	13.676	0
0.011739126	0.000246612	13.676	3E-08
0.0127	0.000285298	12.556	2.979451E-06
0.0142875	0.000341973	10.705	7.852362E-06
0.015875	0.000389627	8.854	1.2725273E-05
0.0174625	0.000428262	7.003	1.7598185E-05
0.01905	0.000457877	5.152	2.2471096E-05
0.0206375	0.000478472	3.301	2.7344007E-05
0.022225	0.000490047	1.45	3.2216919E-05
0.0238125	0.000492603	-0.401	3.708983E-05
0.0254	0.000486138	-2.252	4.1962741E-05
0.3127	-0.001499997	-2.252	0.000923844586
1.8272	-0.011969892	-2.252	0.005572678745
0.013125104	0.000308283	15.304	0
0.013134878	0.000308742	15.304	3E-08
0.0142875	0.00036051	13.96	3.568032E-06
0.015875	0.000424026	12.109	8.440943E-06
0.0174625	0.000478521	10.258	1.3313855E-05
0.01905	0.000523997	8.407	1.8186766E-05
0.0206375	0.000560453	6.556	2.3059677E-05
0.022225	0.000587889	4.705	2.7932589E-05
0.0238125	0.000606305	2.854	3.28055E-05
0.0254	0.000615701	1.003	3.7678411E-05
0.3127	0.001499999	1.003	0.000919560256
1.8272	0.00616157	1.003	0.005568394415
1000000	550	0	326

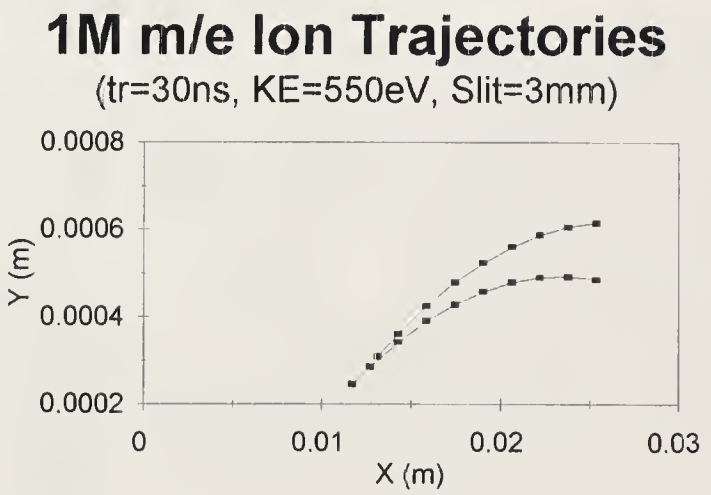

Figure C-14 Plot of 1M m/e beam centerline trajectories between the parallel plates.

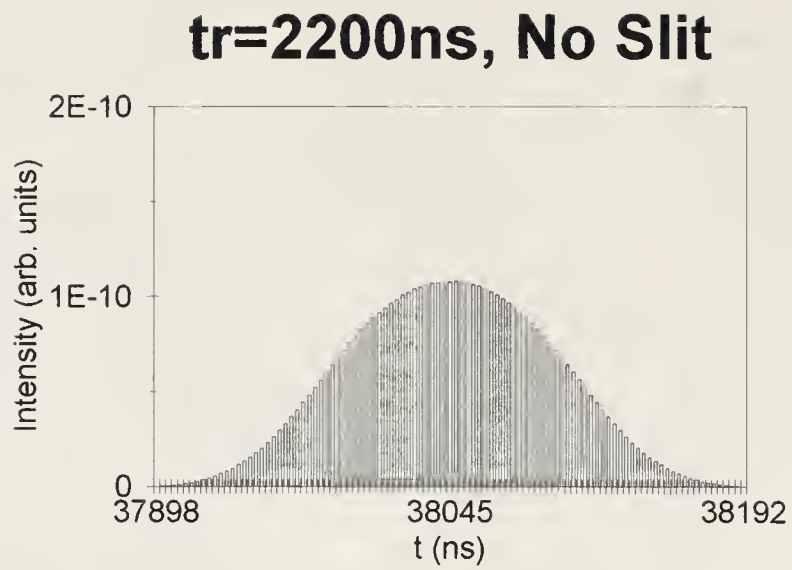

(a)

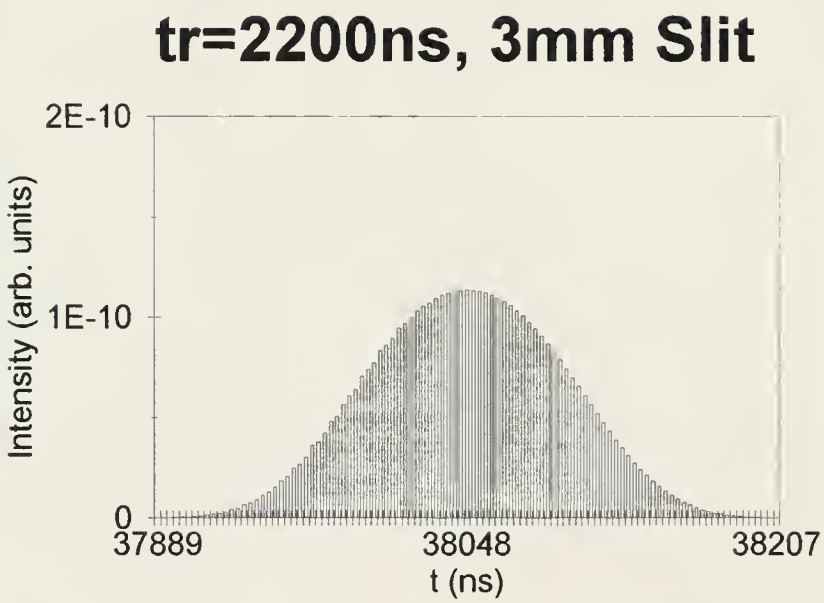

(b)

Figure C-15 CO2+ pulse shapes calculated by TRAJION for 5 slit configurations; tr = 2200 ns, beam diameter = 1 mm, beam temp. = 10 K. (continued on next two pages)

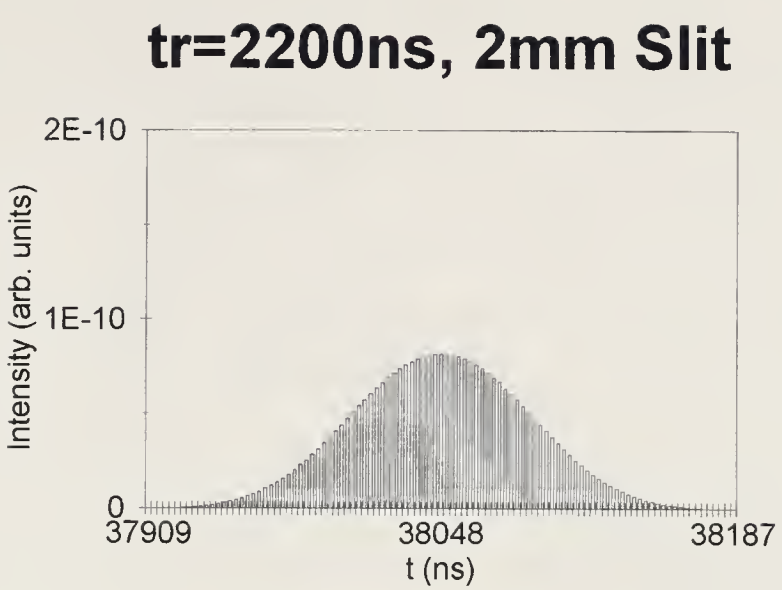

(c)

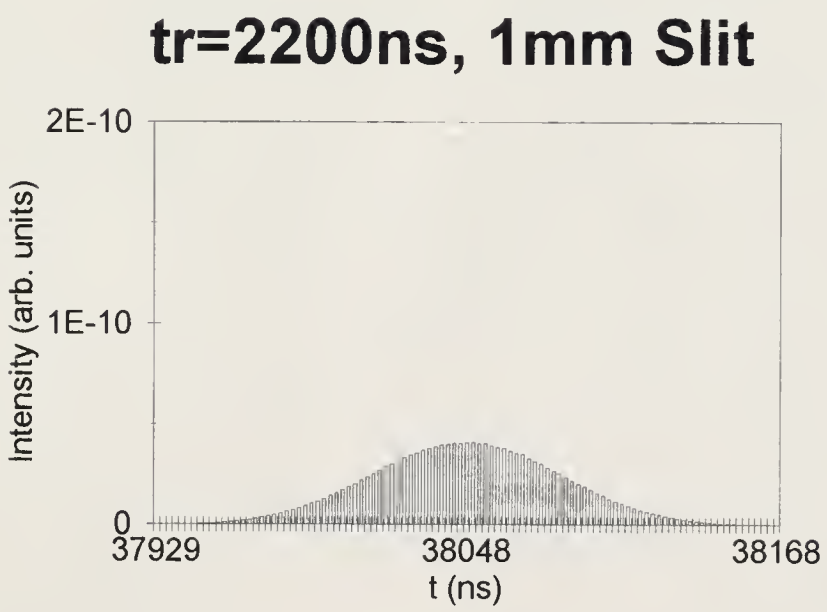

(d)

Figure C-15 (continued)

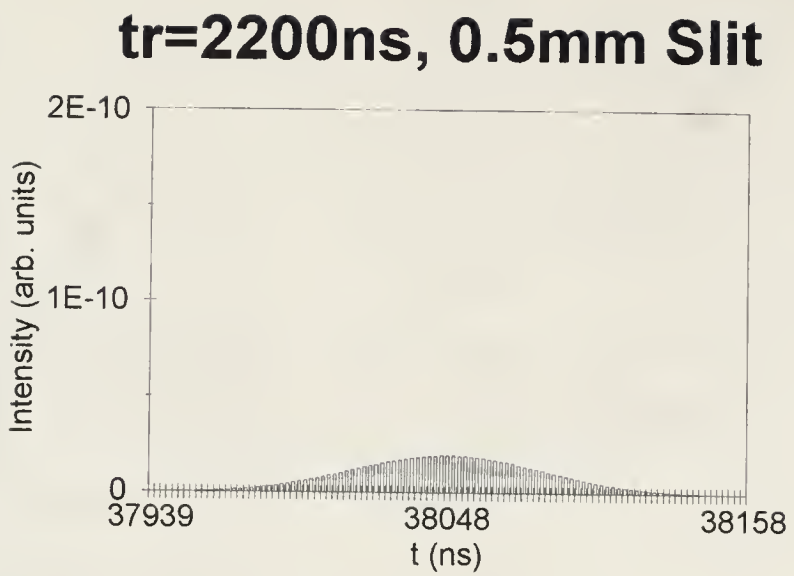

(e)

Figure C-15 (continued)

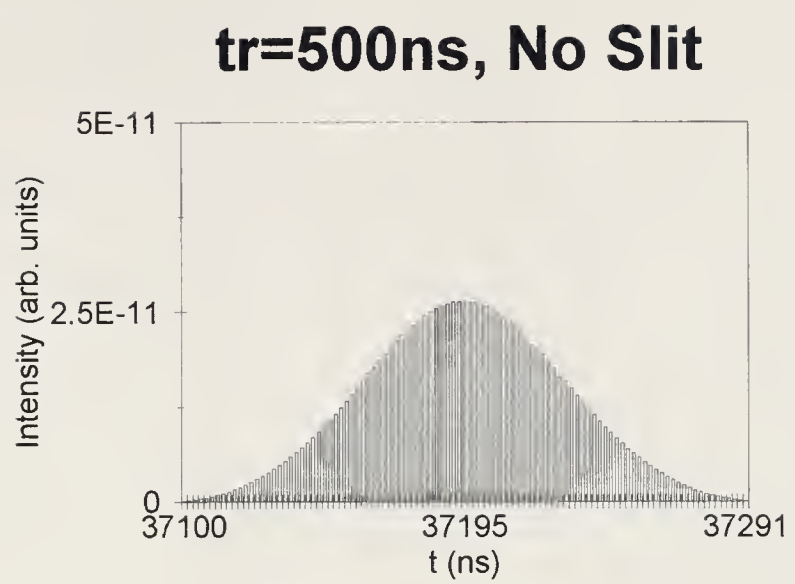

(a)

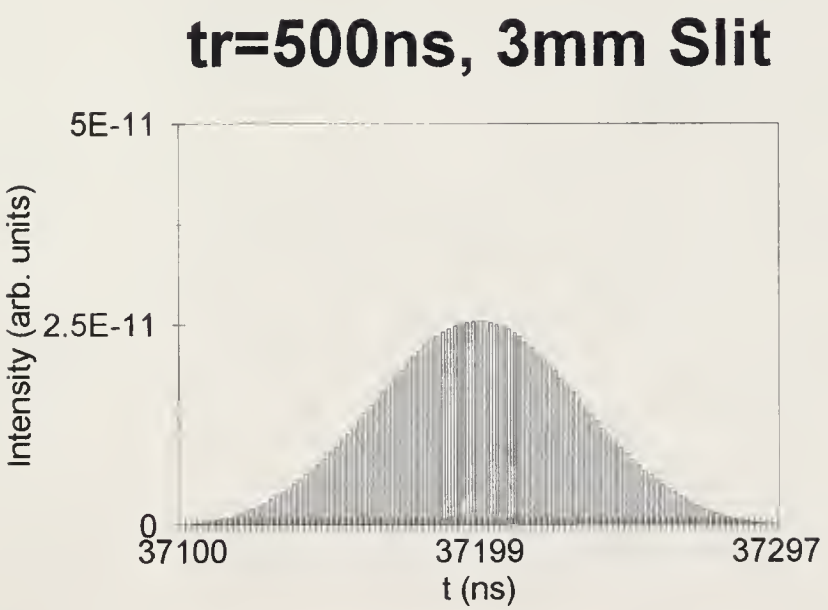

(b)

Figure C-16 CO2+ pulse shapes calculated by TRAJION for 5 slit configurations; tr = 500 ns, beam diameter = 1 mm, beam temp = 10 K. (continued on next two pages)

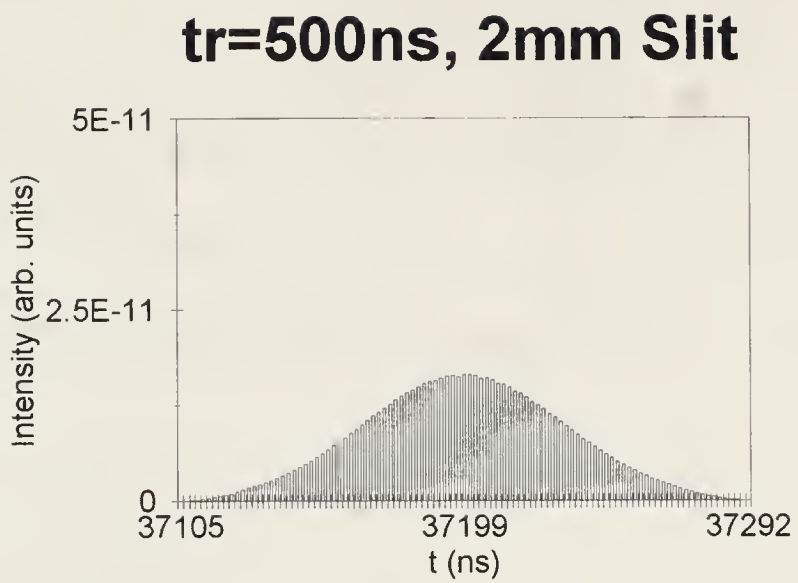

(c)

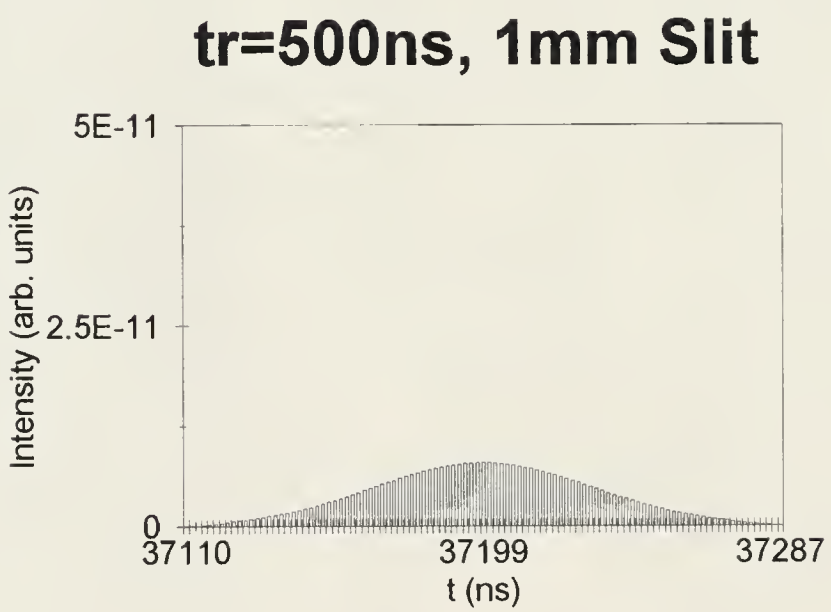

(d)

Figure C-16 (continued)

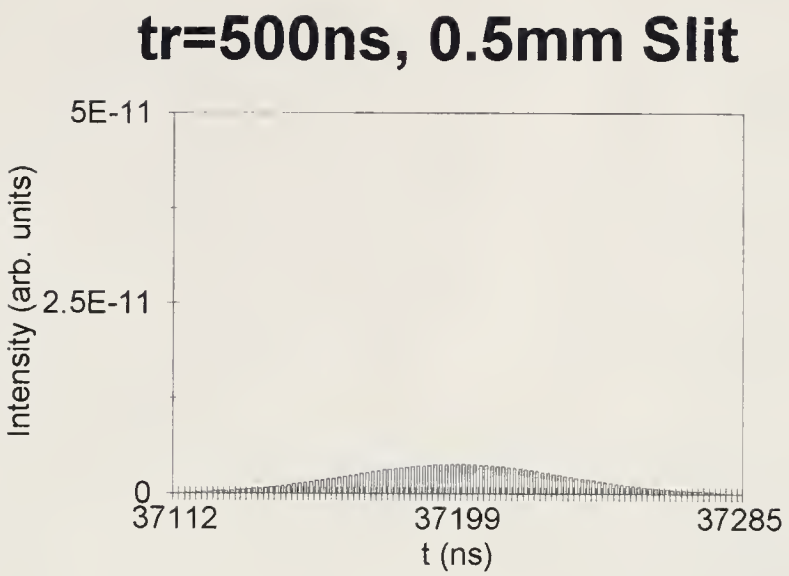

(e)

Figure C-16 (continued)

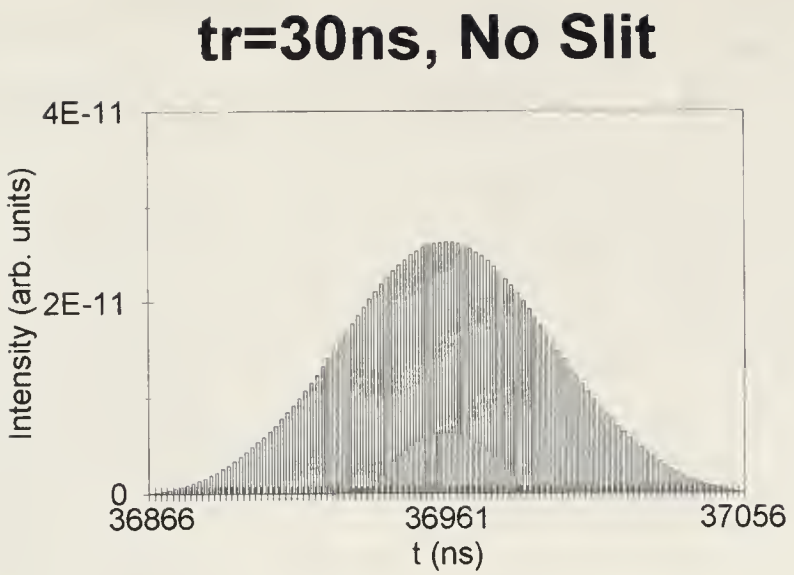

(a)

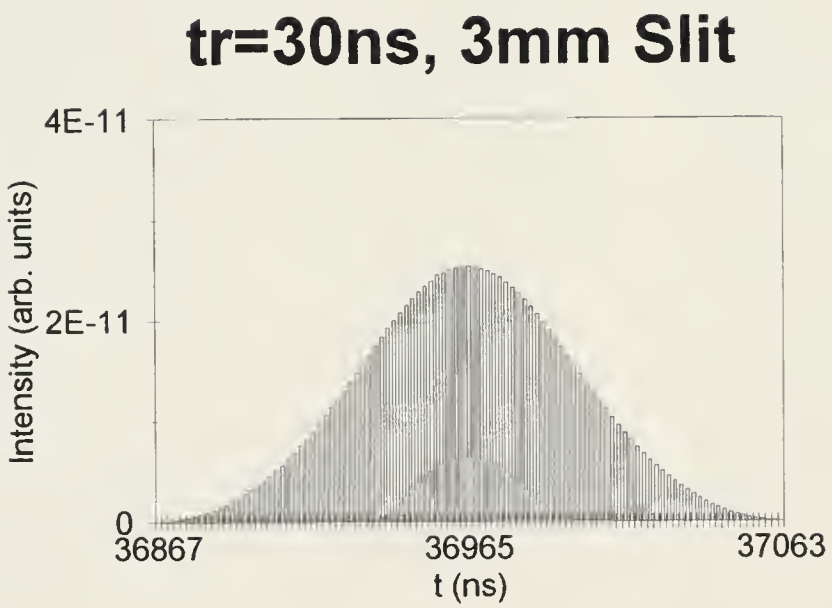

(b)

Figure C-17 CO2+ pulse shapes calculated by TRAJION for 5 slit configurations; tr = 30 ns, beam diameter = 1 mm, beam temp. = 10 K. (continued on next two pages)

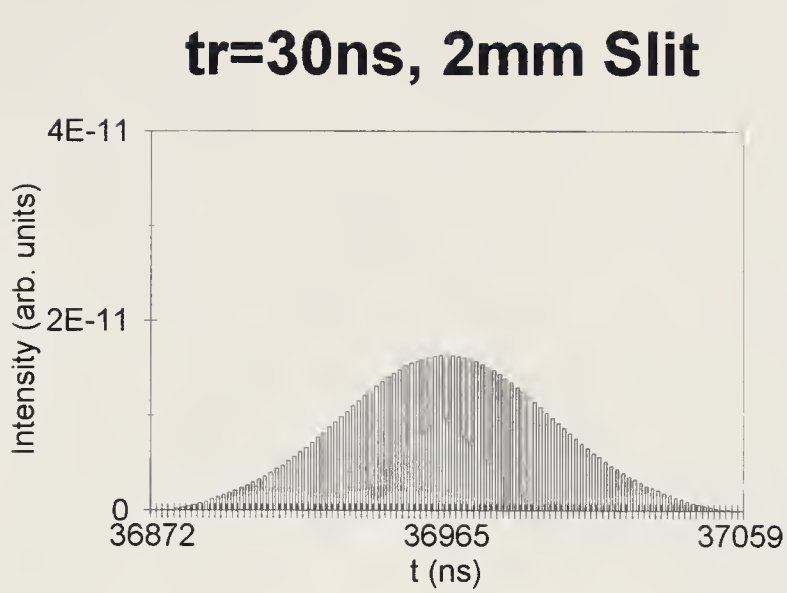

(c)

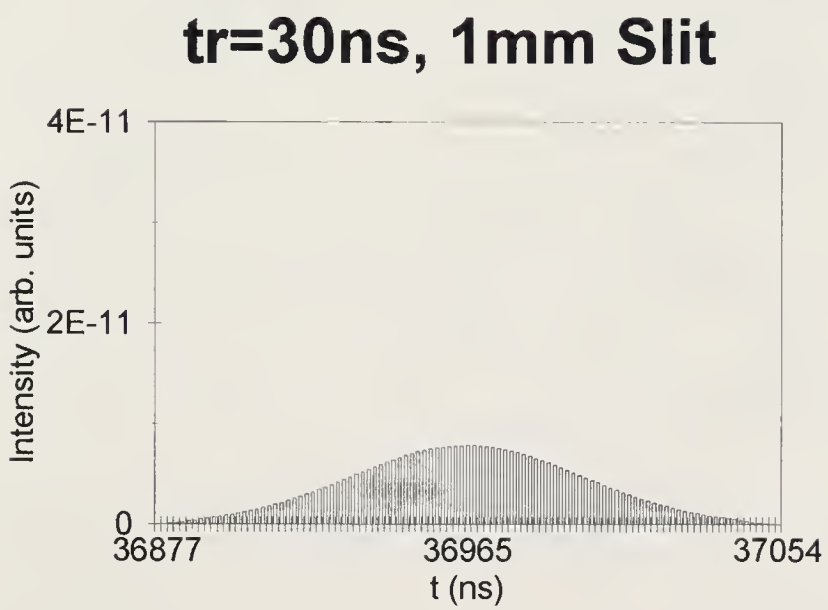

(d)

Figure C-17 (continued)

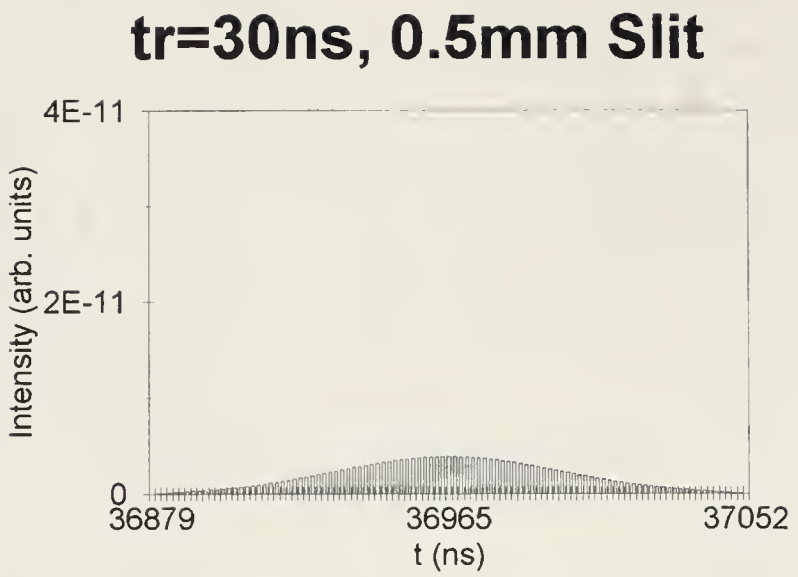

(e)

Figure C-17 (continued)

REFERENCES

1) R. J. Beuhler, G. Friedlander and L. Friedman, Phys. Rev. Lett. 63 (1989) 1292.

2) Martin Fleishmann and Stanley Pons, J. Electroanal. Chem. 261 (1989) 301.

3) D. E. Alburger, J. Phys. Chem. Comments, 94 (1990) 8494.

4) P. M. Echenique, J. R. Manson and R. H. Ritchie, Phys. Rev. Lett. 64 (1990) 1413.

5) C. Carraro, B. Q. Chen, S. Schramm and S. E. Koonin, Phys. Rev. A, 42 (1990) 1379.

6) M. Fallavier, J. Kemmler, R. Kirsch, J. C. Poizat, J. Remillieux and J. P. Thomas, Phys. Rev. Lett. 65 (1990) 621.

7) R. J. Beuhler, Y. Y. Chu, G. Friedlander, L. Friedman and W. Kunnmann, J. Phys. Chem. 94 (1990) 7665.

8) R. J. Beuhler, Y. Y. Chu, G. Friedlander, L. Friedman, J. G. Alessi, V. LoDestro and J. P. Thomas, Phys. Rev. Lett. 67 (1991) 473.

9) Y. K. Bae, D. C. Lorents and S. E. Young, Phys. Rev. A, 44 (1991) 4091.

10) R. J. Beuhler, G. Friedlander and L. Friedman, Phys. Rev. Lett. Errata 68 (1992) 2108.

11) D. H. Lo, R. D. Petrasso and K. W. Wenzel, Phys. Rev. Lett. 68 (1992) 2107.

12) R. Vandenbosch, D. Ye, J. Neubauer, D. I. Will and T. Trainor, Phys. Rev. A, 46 (1992) 5741.

13) Y. K. Bae, R. J. Beuhler, Y. Y. Chu, G. Friedlander and L. Friedman, Phys. Rev. A, 48 (1993) 4461.

14) E. W. Becker, K. Bier and W. Henkes, Z. Physik, 146 (1956) 333.

15) R. P. Andres, R. S. Averback, W. L. Brown, L. E. Brus, W. A. Goddard, III, A. Kaldor, S. G. Louie, M. Moscovits, P. S. Peercy, S. J. Riley, R. W. Siegel, F. Spaepen and Y. Wang, J. Mater. Res. 4 (1989) 704.

16) Pamela M. St. John, Ranier D. Beck and Robert L. Whetten, Phys. Rev. Lett. 69 (1992) 1467.

17) Irwin Stambler, Nanometer Cluster Collisions Spawn "New Chemistry," R & D Magazine (Oct. 1992) 21.

18) Yasunori Yamamura and Tetsuya Muramoto, Phys. Rev. Lett. 69 (1992) 1463.

19) M. Vicanek, I. Abril, N. R. Arista and A. Gras-Marti, Phys. Rev. A. 46 (1992) 5745.

20) C. Deutsch, Laser Part. Beams, 8 (1990) 541.

21) T. Mark and A. Castleman, Advances in Atomic and Molecular Physics, Vol. 20, Academic Press (1985) New York, 65.

22) Malcolm Dole, L. L. Mack, R. L. Hines, R. C. Mobley, L. D. Ferguson and M. B. Alice, J. Chem. Phys. 49 (1968) 2240.

23) L. Mack, P.Kralik, A. Rheude and M. Dole, J. Chem. Phys. 52 (1970) 4977.

24) M. Yamashita and J. B. Fenn, J. Phys. Chem. 88 (1984) 4451.

25) C. R. Blakely, J. J. Carmody and M. L. Vestal, J. Am. Chem. Soc. 102 (1980) 5933.

26) J. Searcy and J. Fenn, J. Chem. Phys. 61 5282.

27) R. Beuhler and L. Friedman, J. Chem. Phys. 77 (1982) 2549.

28) Lewis Friedman and Robert J. Beuhler, J. Chem. Phys. 78 (1983) 4669.

29) M. A. Johnson, M. L. Alexander and W. C. Lineberger, Chem. Phys. Lett. 112 (1984) 285.

30) M. L. Alexander, M. A. Johnson and W. C. Lineberger, J. Chem. Phys. 82 (1985) 5288.

31) Y. K. Bae, P. C. Cosby, M. Nicholson and W. Olson, Rev. Sci. Instrum. 62 (1991) 1157.

32) P. J. Kuntz and J. Valldorf, Z. Physik D, 8 (1988) 195.

33) M. Amarouche, G. Durand and J. P. Malrieu, J. Chem. Phys. 88 (1988) 1010.

34) Y. K. Bae, P. C. Cosby and D. C. Lorents, Chem. Phys. Lett. 159 (1989) 214.

35) Michael L. Alexander, M. A. Johnson, Nancy E. Levinger and W. C. Lineberger, Phys. Rev. Lett. 57 (1986) 976.

36) Nancy E. Levinger, Douglas Ray, Michael L. Alexander and W. C. Lineberger, J. Chem. Phys. 89 (1988) 5654.

37) Nancy E. Levinger, Douglas Ray, Kermit K. Murray, Amy S. Mullin, C. P. Schultz and W. C. Lineberger, J. Chem. Phys. 89 (1988) 71.

38) M. Kappes and S. Leutwyler, Ch. 15, Atomic and Molecular Beam Methods, Giacinto Scoles, ed. Oxford University Press (1988) New York, 380.

39) Gilbert D. Stein, Surface Science, 156 (1985) 44.

40) Otto F. Hagena, Ch. 2, Molecular Beams and Low Density Gasdynamics, Peter P. Wegener, ed. Marcel Dekker (1974) New York, 93.

41) Otto F. Hagena, Surface Science, 106 (1981) 101.

42) David R. Miller, Ch. 2, Atomic and Molecular Beam Methods, Giacinto Scoles, ed. Oxford University Press (1988) New York, 14.

43) A. Ryali and J. Fenn, Ber. Bunsenges. Phys. Chem. 88 (1984) 245.

44) O. Hagena, Z. Angew. Physik, 16 (1963) 183.

45) W. Ronald Gentry and Clayton F. Giese, Rev. Sci. Instrum. 49 (1978) 595.

46) M. G. Liverman, S. M. Beck, D. L. Monts and R. E. Smalley, J. Chem. Phys. 70 (1979) 192.

47) Katherine L. Saenger, J. Chem. Phys. 75 (1981) 2467.

48) Katherine L. Saenger and John B. Fenn, J. Chem. Phys. 79 (1983) 6043.

49) Atomic and Molecular Beam Methods, Giacinto Scoles, ed. Oxford University Press (1988) New York.

50) Basic Vacuum Practice, Varian Associates, (1986), Palo Alto.

51) R. N. Peacock, J. Vac. Sci. Technol. 17 (1980) 330.

52) SIMION v4.02 is available from D. A. Dahl, MS 2208, Idaho National Engineering Laboratory, EG&G Idaho Inc., PO Box 1625, Idaho Falls, ID 83415.

53) Series 9 valve performance characteristics are obtainable from Dan Gibson, General Valve Corp. 19 Gloria Lane, PO Box 1333, Fairfield, NJ 07004.

54) S. Matsuura, S. Umebayashi, C. Okuyama and K. Oba, IEEE Trans, 32 (1985) 350.

55) J. M. B. Bakker, J. Phys. E, 6 (1973) 785.

56) J. M. B. Bakker, J. Phys. E, 7, (1974) 364.

57) G. E. Yefchak, G. A. Schultz, J. Allison, C. G. Enke and J. F. Holland, J. Am. Soc. Mass Spectrom 1 (1990) 440.

58) Ce Ma, Steven M. Michael, Mingta Chien, Jianzhong Zhu and David M. Lubman Rev. Sci. Instrum. 63 (1992) 139.

59) Jean H. Futrell, Thomas O. Tiernan, Fred P. Abramson and C. Dean Miller, Rev. Sci. Instrum. 39 (1968) 340.

60) C. D. Miller, T. O. Tiernan and J. H. Futrell, Rev. Sci. Instrum. 40 (1969) 503.

61) Gary L. Glish and Douglas E. Goeringer, Anal. Chem. 56 (1984) 2291.

62) John T. Stults, Christie G. Enke and John F. Holland, Anal. Chem. 55 (1983) 1323.

63) B. A. Eckenrode, J. T. Watson, C. G. Enke and J. F. Holland, Int. J. Mass Spectrom. Ion Processes 83 (1988) 177.

64) J. David Pinkston, Martin Rabb, J. Throck Watson and John Allison, Rev. Sci. Instrum. 57 (1986) 583.

65) J. T. Watson, G. A. Schultz, R. E. Tecklenburg, Jr. and J. Allison, J. Chromatogr. 518 (1990) 283.

66) G. A. Schultz, B. A. Chamberlin, C. C. Sweeley, J. T. Watson and J. Allison, J. Chromatogr. 590 (1992) 329.

67) David J. Burnsed, Power Supply Gates MOSFET, EDN (Sep. 30, 1993) 117.

68) Data acquisition computer code is available from TOFTEC Inc., P.O. Box 12877, Gainesville, FL 32604.

69) P. Hobza, R. Struzinsky, N. Duc Thang and R. Zahradnik, Collection Czechoslov. Chem. Commun. 41 (1978) 1727.

70) Lawrence S. Bartell, Laszlo Harsanyi and Edward J. Valente, J. Phys. Chem. 93 (1989) 6201.

71) Kenzo Hiraoka and Shinichi Yamabe, Chem. Phys. Lett. 154 (1989) 139.

72) Vladimir Frecer, Duli C. Jain and Anne-Marie Sapse, J. Phys. Chem. 95 (1991) 9263.

73) Q. Y. Shang, P. O. Moreno, C. Dion and E. R. Bernstein, J. Chem. Phys. 98 (1993) 6769.

74) M. T. Bowers, Ion and Cluster Ion Spectroscopy and Structure, J. P. Maier, ed. Elsevier (1989) Amsterdam, 241.

BIOGRAPHICAL SKETCH

Steven Dane Thompson was born in Pensacola, Florida, on September 17, 1962, to Bobby H. and Mary J. Thompson; he is the youngest of three children. He graduated from Tate High School in 1980. He received an Associate of Arts degree from Pensacola Junior College in 1982 and graduated in 1984 from the University of West Florida with a Bachelor of Science degree in chemistry. On November 30, 1984, he was commissioned a Second Lieutenant in the United States Air Force after successful completion of Officer Training School at San Antonio, Texas.

He was assigned to the Tactical Air Warfare Center at Eglin Air Force Base, Florida, until the Fall of 1986 when he entered the Graduate School at the University of Florida. There he earned a Master of Science in nuclear chemistry in 1987 through the Air Force Institute of Technology Civilian Institute program.

After completing his master's degree he was assigned to the Astronautics Laboratory at Edwards Air Force Base, California. He graduated from Squadron Officer School in June 1989. In the fall of 1990 he once again entered the University of Florida Graduate School to pursue a doctoral degree in chemistry

Steven Thompson is currently a Captain in the United States Air Force. He has been selected to teach at the United States Air Force Academy upon completion of his current duty assignment. He is married to the former Lee Ann Parker. They have one son, Justin Steven, born on November 26, 1986, and a daughter, Tara Leanne, who was born May 9, 1990.

I certify that I have read this study and that in my opinion it conforms to acceptable standards of scholarly presentation and is fully adequate, in scope and quality, as a dissertation for the degree of Doctor of Philosophy.

M. Luis Muga, Chairman
Professor of Chemistry

I certify that I have read this study and that in my opinion it conforms to acceptable standards of scholarly presentation and is fully adequate, in scope and quality, as a dissertation for the degree of Doctor of Philosophy.

Robert J. Hanrahan
Professor of Chemistry

I certify that I have read this study and that in my opinion it conforms to acceptable standards of scholarly presentation and is fully adequate, in scope and quality, as a dissertation for the degree of Doctor of Philosophy.

Martin T. Vala, Jr.
Professor of Chemistry

I certify that I have read this study and that in my opinion it conforms to acceptable standards of scholarly presentation and is fully adequate, in scope and quality, as a dissertation for the degree of Doctor of Philosophy.

William Weltner, Jr.
Professor of Chemistry

I certify that I have read this study and that in my opinion it conforms to acceptable standards of scholarly presentation and is fully adequate, in scope and quality, as a dissertation for the degree of Doctor of Philosophy.

Francis E. Dunnam
Professor of Physics

This dissertation was submitted to the Graduate Faculty of the Department of Chemistry in the College of Liberal Arts and Sciences and to the Graduate School and was accepted as partial fulfillment of the requirements for the degree of Doctor of Philosophy.

April 1994

_____

Dean, Graduate School

LD
1780
1994
.T476

UNIVERSITY OF FLORIDA
3 1262 08557 0819